Title

Modeling of Solar and Atmospheric Radiation Transfer with Cloud and Aerosol Variability for Solar Energy Applications

Author

Liao, Zhouyi

Publication Date

2021

Peer reviewed|Thesis/dissertation

UNIVERSITY OF CALIFORNIA SAN DIEGO

Modeling of Solar and Atmospheric Radiation Transfer with Cloud and Aerosol Variability for Solar Energy Applications

A Dissertation submitted in partial satisfaction of the
requirements for the degree
Doctor of Philosophy

in

Engineering Sciences (Mechanical Engineering)

by

Zhouyi Liao

Committee in charge:

Professor Carlos F. M. Coimbra, Chair
Professor Renkun Chen
Professor Amato Evan
Professor Jan P. Kleissl
Professor Lynn M. Russell

2021

The Dissertation of Zhouyi Liao is approved, and it is acceptable in quality and form for publication on microfilm and electronically.

University of California San Diego

2021

DEDICATION

This work is dedicated to my dear parents, for their support and encouragement.

EPIGRAPH

Somewhere, something incredible is waiting to be known.

—Carl Sagan

TABLE OF CONTENTS

LIST OF FIGURES

LIST OF TABLES

ACKNOWLEDGEMENTS

First, I would like to express my sincere appreciation to my advisor Prof. Carlos F. M. Coimbra for motivating and helping me throughout my journey of PhD research. His invaluable guidance and advice helped me in all the time of the research and writing of this thesis. I am grateful and honored to have joined his group and to have had the opportunity to conduct the research I am interested in. I would also like to thank him for his friendship, caring heart, and great sense of humor. I could not have imagined having a better advisor. I would also like to express my gratitude to the rest of my committee: Profs. Renkun Chen, Amato Evan, Jan Kleissl and Lynn Russel, for their constructive suggestions and insightful comments.

I would also like to knowledge the help and support from previous and present research group members. First, I would like to thank Dr. Mengying Li, who provided invaluable advice and help for my research and life and being a good friend. I also want to thank Dr. David Larson and Dr. Hugo Pedro for their valuable technical help and patience. Thanks also to Dr. Yinghao Chu and Richard Inman, who provided guidance during my first year here. I would also like to thank Jessica Medrado and Lysha Matsunobu for their inspiration and encouragement.

I am extremely grateful to my parents for their love, caring and sacrifices for educating and preparing me for my future. My gratitude also goes to my friend and roommate Meihan Li, who offered me great help and company in the past year during the pandemic period.

A large portion of Chapter 3 is a combination of two publications: M. Li, Z. Liao, and C. F. M. Coimbra (2018) "Spectral model for clear sky atmospheric longwave radiation" *Journal of Quantitative Spectroscopy and Radiative Transfer*, 209, 196-211; M. Li, Z. Liao and C. F. M. Coimbra (2018) "An Efficient Spectral Model for Evaluating Spectral and Spatial Distributions of Clear Sky Atmospheric Longwave Radiation," accepted for the *16th International Heat Transfer Conference (IHTC-16)*. The dissertation author is the second author of these manuscripts.

Chapter 4, in full, is from the publication: Z. Liao, M. Li, and C. F. M. Coimbra (2019) " Anisotropic Corrections for the Downwelling Radiative Heat Transfer Flux from Various Types of Aerosols " *International Journal of Heat and Mass Transfer* , 136, 1006-1016. The dissertation author is the first author of this manuscript.

Chapter 5 and 6, in full are in preparation as a manuscript for publication with my co-author and advisor C. F. M Coimbra at UC San Diego. The dissertation author is also the first author of these papers.

VITA

2021	Ph. D. in Engineering Sciences (Mechanical Engineering), University of California San Diego, U. S.
2016	M. S. in Environmental Engineering, Stanford University, U. S.
2014	B. S. in Environmental Engineering, University of California San Diego, U. S.

PUBLICATIONS

Liao, Z., and Coimbra, C. F. M. (2021) "Solar Irradiance Prediction from GOES-R imagery using SCOPE method and convolutional neural networks", in preparation.

Liao, Z., and Coimbra, C. F. M. (2021) "Advanced Multi-layer Spectral cloud optical property estimation using real-time GOES-R imagery", in preparation.

Li, M., Liao, Z., and Coimbra, C. F. M. (2020) "Spectral solar irradiance on inclined surfaces: A fast Monte Carlo approach," *Journal of Renewable and Sustainable Energy*, 12, 053705.

Liao, Z., Li, M., and Coimbra, C. F. M. (2019) "Approximation of Anisotropic Aerosol Scattering Effects on Longwave Irradiance". *International Journal of Heat and Mass Transfer*, 136, 1006-1016.

Li, M., Liao, L. and Coimbra, C. F. M. (2018) "Spectral Model for Clear Sky Atmospheric Longwave Radiation," *Journal of Quantitative Spectroscopy and Radiative Transfer* 209, 196–211.

Li, M., Liao, Z. and Coimbra, C. F. M. (2018) "Spectral Model for Clear-Sky Longwave Surface Irradiance ", *American Meteorological Society 31st Conference on Climate Variability and Change*, Austin, TX.

Liao, Z., Li, M. and Coimbra, C. F. M. (2018) "Nonisotropic Aerosol Scattering Effects on Longwave Irradiance" , *American Meteorological Society 10th Symposium on Aerosol–Cloud–Climate Interactions*, Austin, TX.

Coimbra, C. F. M., Li, M., and Liao, Z. (2018) "Efficient Model for Evaluation of Spectral and Vertical Distributions of Atmospheric Longwave Radiation", *Proceedings of The 16th International Heat Transfer Conference*, pp. 8287-8295.

Chu, Y., Nonnenmacher, L., Inman, R. H., Liao, Z., Pedro, H. T. C., and Coimbra, C. F. M. (2014) "A Smart Image-Based Cloud Detection System for Intra-Hour Solar Irradiance Forecasts," *Journal of Atmospheric and Oceanic Technology*, 31(9), 1995-2007.

ABSTRACT OF THE DISSERTATION

Modeling of Solar and Atmospheric Radiation Transfer with Cloud and Aerosol Variability for Solar Energy Applications

by

Zhouyi Liao

Doctor of Philosophy in Engineering Sciences (Mechanical Engineering)

University of California San Diego, 2021

Professor Carlos F. M. Coimbra, Chair

The rapid growth of global solar utilization for power generation poses increasing stress on grid reliability and performance due to the variability of the solar resource. This variability mainly comes from cloud coverage, water vapor content and aerosol loading. Cloud cover has, by far, the greatest effect on short-term solar power generation. The highly volatile nature of solar insolation at the ground level requires a more dynamic response from the power grid. More accurate short-term solar power prediction is a cost-effective way to provide bidding strategies for real-time markets and to determine the need for dispatch strategies and management of operating reserves. This work contributes to solar integration efforts by employing comprehensive spectral radiative models to calculate longwave and shortwave radiation through the atmosphere, estimating cloud properties from remote sensing data with the atmospheric model and building convolutional neural network (CNN) models to estimate solar radiation at the ground level.

A Line-by-Line (LBL) spectral radiative model is built to capture details of the wavenumber-dependent nature of irradiance fluxes through the atmosphere. A broadband empirical model serves as a benchmark to validate the LBL model. For the longwave spectrum that is emitted and absorbed by gases, aerosols, clouds and the ground, a high-resolution two-flux model with a fast recursive scattering method is developed and tested. For the shortwave (solar) part of the spectrum, which includes scattering from atmospheric constituents and the ground, 3D comprehensive Monte-Carlo simulations are used. Beyond the basic models, some corrections and additional calibrations are made. Monte Carlo simulations are used for correcting deviations on the atmospheric downwelling longwave (DLW) flux caused by isotropic scattering assumptions for very high aerosol loading regimes. The δ-M approximation input-based scaling rule is validated for a wide range of aerosol loading values except for very high aerosol loading conditions. A proposed scaling rule minimizes substantially the computational effort of calculating anisotropic downwelling radiation from various types of aerosols under these extreme conditions. Earth curvature effects are modelled using standard air mass corrections. A plane-parallel atmosphere approximation is found to be accurate enough for modeling of solar power generation.

A Spectral Cloud Optical Property Estimation (SCOPE) method that integrates the high-resolution imagery from GOES-R satellite and a two-stream, spectrally-resolved longwave radiative model is evaluated for the estimation of cloud optical depth and cloud bottom height. An improved version of the original model (SCOPE 2.0) is proposed. This new version of SCOPE considers multi-layer clouds, clouds with ice crystals and additional aerosol corrections. A shortwave Monte Carlo simulation is developed and used to validate the derived cloud optical properties. With this comprehensive cloud cover estimate model, a convolutional neural networks (CNN) model is developed to correlate global horizontal irradiance (GHI) to the satellite-derived cloud cover values. The performance of SCOPE method as well as CNN+SCOPE model is evaluated using one year (2018) of downwelling longwave (DLW) radiation and GHI measurements from the Surface Radiation Budget Network, which consists of seven sites spread across climatically diverse regions of the contiguous United States. The CNN+SCOPE model achieves test-set root-mean-square error (RMSE) of 30.5 - 62.6 W m^{-2} with an average of 47.2 W m^{-2}, which is an improvement over then the National Solar Radiation Database, NSRDB, model (average RMSE of 66.9 W m^{-2}).

Chapter 1

Introduction

1.1 Motivation and objectives

Due to concerns with climate change and the role the energy industry plays in releasing greenhouses to the atmosphere, as well as the declining cost of solar generation, the market share of solar power has increased rapidly in the decade. The global share of solar generation is almost 3% of the total electricity generation [7], a share that was only 1.2% in 2016 [8].

Despite of the rapid growth of solar power utilization, its energy market share is still very low compared to fossil fuels. The major challenge for even faster growth of solar utilization is the variability of the solar resource. This variability is mostly caused by cloud coverage, water vapor content and aerosol loading. Solar variability has grid integration consequences due to the difficulties presented by short-term solar power prediction. In partly-cloudy conditions, the power output from solar plants can drop to near zero with time scales of the order of a minute [9]. The highly volatile nature of the solar insolation makes it difficult to integrate solar power output to electricity grids that were designed to rely on steady generation. Understanding and predicting the solar resource with high accuracy also helps in the development of bidding strategies for real-time markets as well as to determine the need for operating reserves [10].

Although water vapor content and aerosol loadings also affect light transmission to the ground level, short-term solar power variability mostly comes from clouds due to the short time constants associated with cloud inception, transport and dissipation rates. Important features of cloud cover for ground irradiation include the optical and physical thickness of cloud decks, cloud bottom height and both vertical and horizontal

distributions [10]. Some of current solar forecasting methods use either binary (clear or cloudy) or coarse representations of sky conditions[11]. Recent years, many studies make short-term forecasting by correlating total sky imagers to solar power output or GHI. Marquez et al. (2012) derived three sky cover(SC) indices from the observed cloud cover via total sky imagers. They found the optimal correlation between GHI and SC indices and employed an artificial neural network (ANN) algorithm to improve the forecasting model [12]. Chu et al. (2014) proposed a automatic smart adaptive cloud identification (SACI) system for sky imagery and solar irradiance forecast. Cloud cover classification retrieved by SACI is used as an input for an artificial neural network model that predicts 1-min average global horizontal irradiance (GHI), 5-, 10-, and 15-min ahead of time[13]. Apart from ANN, convolutional neural networks (CNN) are commonly used for the task of image recognition and could be applied for short-term solar forecasting from satellite images or total sky images. For example Y. Sun et al. [14] used CNN to forecast a current PV output from a contemporaneous total-sky image (a "nowcasting"). Recently, Ryu et al. [15] made a step forward to use CNN to forecast 5-20 min ahead of global horizontal irradiance using total-sky images and lagged GHI. This model performs root-mean-square error (RMSE) of 49-177 W/m^2, 93-146W/m^2, 71-118W/m^2 in sunny day, partly cloudy day and overcast day, respectively.

The current CNN-related solar forecast models rely heavily on ground instruments. However, ground instruments are not always available in every location and the implementation cost is high. Therefore, we aim to use satellite data, which can be obtained from GOES database, to minimize the cost to estimate the atmospheric variability, and to find low-cost strategies to mitigate the intermittency of solar power. At locations where ground instruments are available, local-sensing techniques together with remote sensing techniques are used to provide more accurate cloud and aerosol information as inputs to forecasting models.

The current research mainly focus on two parts: radiative transfer modelling and solar forecasting.

- Use Monte Carlo technique to estimate the impact of aerosol loadings on atmospheric radiation
- Use Monte Carlo technique and two-flux approximation to estimate the impact of cloud cover on earth radiation energy budget and derive cloud information from remote sensing database
- Use convolutional neural networks to model global horizontal irradiance and make short-term and long-term forecast

1.2 Basics of Radiation

1.2.1 Characteristics of longwave and shortwave radiation

Electromagnetic radiation is characterized by its wavelength/wavenumber/frequency [16]. By definition, wavelength λ, wavenumber ν and frequency ν_f are related as,

$$\lambda = \frac{1}{\nu} = \frac{c}{\nu_f}, \tag{1.1}$$

where c is the speed of light. The wavenumber is used in future chapters unless stated otherwise.

The monochromatic emissive intensity of a black surface, $I_{b\nu}$, as the radiant power emitted per unit area of surface per unit solid angle per unit wavenumber, is expressed by Planck's law,

$$I_b(\nu, T) = \frac{2hc^2\nu^3}{\exp\left(\frac{hc\nu}{k_B T}\right) - 1}, \tag{1.2}$$

where ν (m^{-1}) is wavenumber, $h = 6.626 \times 10^{-34}$ J s is Planck's constant, $c = 3 \times 10^8$ m s^{-1} is the speed of light and $k_B = 1.38 \times 10^{-23}$ J K^{-1} is the Boltzmann constant.

The shortwave solar irradiance is emitted by the Sun at high temperatures with a cutoff wavelength of 4 micrometers. The atmospheric longwave irradiance is emitted by gases and surfaces at temperatures ranging roughly from 200 to 320 K [16]. For the solar irradiance, the 2000 ASTM Standard Extraterrestrial Spectrum is used [17]. Atmospheric longwave irradiance is mostly in the wavenumber spectral range from 0 to 2,500 cm^{-1} while solar shortwave irradiance is considered in this work to range from 2,500 to 40,000 cm^{-1}.

Therefore, the longwave irradiance (LW) referred in this work is the emitted radiation from atmosphere constituents and the Earth's surface, in the spectral range of 0 to 2,500 cm^{-1}. The solar shortwave irradiance (SW) is the emitted radiation from the Sun that is in the spectral range of 2,500 to 40,000 cm^{-1}. The emission by the atmosphere and Earth is assumed to be diffuse (no preferable direction) while the solar irradiance is highly directional. The LW transfer in the atmosphere includes processes of emission, absorption, scattering/reflection. While for SW, the processes involves only absorption and scattering/reflection.

1.2.2 Radiative Transfer Equation

Consider a beam of radiation traverses a participating medium, which may gain energy from emission or may lose energy to scattering or absorption. If we denote the extinction coefficient as κ_ν and emission coefficient as j_ν, we can write down the radiative equation describing the overall process. The change in energy in a specified frequency range $d\nu$ centered on a frequency ν as a result of absorption, of a beam of radiation traversing some thickness ds of the medium, which has cross-sectional area $\mathrm{d}\sigma_c$, in a time dt is given by

$$dE_\nu = \kappa_\nu \rho I_\nu ds d\nu d\sigma_c d\Omega dt, \tag{1.3}$$

where the spectral radiance, I_ν is defined to be the amount of incident radiant energy intensity, $d\Omega$ is the solid angle subtended by the beam, ρ is the density of the medium and κ_ν is the extinction coefficient at that frequency which accounts for both absorption and scattering processes. In addition to the energy removed by absorption and scattering as Eq.1.3 does, there may exist processes in the medium by which radiant energy is emitted into the radiation field:

$$dE_\nu = j_\nu \rho ds d\nu d\sigma_c d\Omega dt, \tag{1.4}$$

where the emission coefficient j_ν is the rate at which energy is emitted by the constituent particles of the medium. In a scattering medium with some nonzero albedo, there will be a contribution to the emitted radiation field from radiation that is scattered from all other directions in the propagation direction that is considered. The direction of the radiation scattered out of a beam is denoted as (θ_0, ϕ_0). Combining both removal and emission processes, the sum of the amount of energy change is [18]:

$$\frac{dE_\nu}{ds} = j_\nu \rho d\nu d\sigma d\omega dt - \kappa_\nu I_\nu \rho d\nu d\sigma d\omega dt, \tag{1.5}$$

which can be simplified as

$$-\frac{dI_\nu}{\kappa_\nu \rho ds} = I_\nu - J_\nu, \tag{1.6}$$

For a scattering medium, the source function has the form

$$J_\nu = \frac{1}{4\pi}\int_0^{\pi}\int_0^{2\pi} P(\theta_0,\phi_0;\theta,\phi)I(\theta_0,\phi_0)\sin\theta_0\, d\theta_0\, d\phi_0, \tag{1.7}$$

By adding the blackbody emission I_b, the overall radiative transfer equation can be written in the form :

$$\frac{\partial I(\theta,\phi)}{\kappa\rho\partial s} = -I(\theta,\phi) + (1-\omega_s)I_b(T) + \frac{\omega_s}{4\pi}\int_0^{\pi}\int_0^{2\pi} P(\theta_0,\phi_0;\theta,\phi)I(\theta_0,\phi_0)\sin\theta_0\, d\theta_0\, d\phi_0, \tag{1.8}$$

where ω_s is the scattering albedo and $P(\theta_0,\phi_0;\theta,\phi)I(\theta_0,\phi_0)$ is the scattering phase function. Thus, the radiative transfer equation is an integro-differential equation, which we must solve to understand the nature of the radiation field in the medium of interest. The complex nature of most phase functions of interest makes solving this equation analytically difficult therefore Monte Carlo and other numerical methods are usually used [19].

1.2.3 Components of solar Radiation

The solar radiation incident on the top of atmosphere (TOA) is parallel with the direction being defined by a solar zenith angle θ and an azimuth angle ϕ. Once enter the atmosphere, some photons are scattered and some are absorbed by gas molecules, aerosols and clouds. The solar radiation incident on the Earth's surface thus consists of both a direct (in the direction of solar rays) and a diffuse component (scattered out of the direction of solar rays). When measured on the ground, the Direct Normal Irradiance (DNI) is the direct component, defined as the solar radiation received by a surface placed perpendicular (or normal) to the extraterrestrial solar rays. The Diffuse Horizontal Irradiance (DHI) quantifies the diffuse component, which is defined as the solar radiation received by a surface that is not in the direction of extraterrestrial solar rays. The global horizontal irradiance (GHI) is the combination of both direct and diffuse components, which is defined as the total solar radiation received by a surface placed horizontal on the ground,

$$\mathrm{GHI} = \mathrm{DNI}\cos\theta_z + \mathrm{DHI}, \tag{1.9}$$

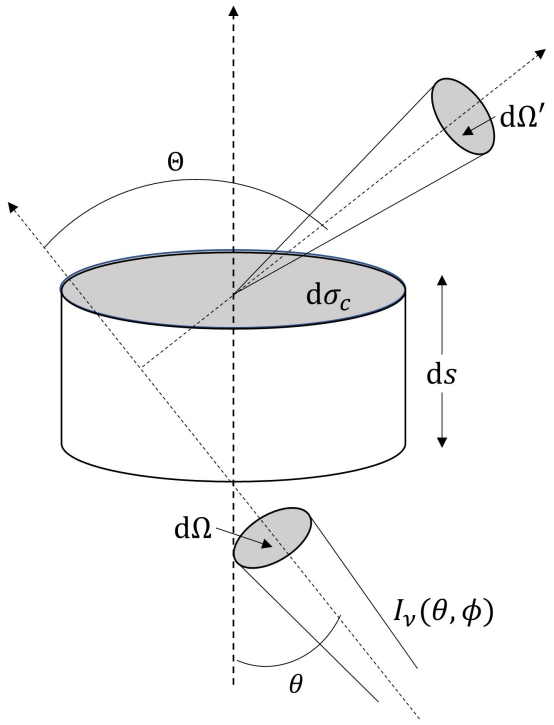

Figure 1.1: Energy transfer across a differential volume. A pencil of radiation in the frequency interval $(\nu, \nu + d\nu)$ is incident upon the volume $\mathrm{d}s\mathrm{d}\sigma_c$ at an angle θ. We are interested in the change in radiant energy, $\mathrm{d}E_\nu$ that results from absorption and scattering throught the angle Θ into the solid angle $\mathrm{d}\Omega$.

Some common methodologies and terms used in future chapters are presented in this section.

1.2.4 Assessment metrics

Four statistical metrics are implemented to assess the accuracy of the proposed models: mean biased error (MBE), root mean square error (RMSE), relative mean biased error (rMBE) and relative root mean square error (rRMSE).

$$\mathrm{MBE} = \frac{1}{K}\sum_{k=1}^{K}\left(\hat{I}_k - I_k\right), \tag{1.10}$$

$$\mathrm{RMSE} = \sqrt{\frac{1}{K}\sum_{k=1}^{K}\left(\hat{I}_k - I_k\right)^2}, \tag{1.11}$$

$$\mathrm{rMBE} = \frac{\mathrm{MBE}}{1/K\sum_{k=1}^{K} I_k}, \tag{1.12}$$

$$\mathrm{rRMSE} = \frac{\mathrm{RMSE}}{1/K\sum_{k=1}^{K} I_k}, \tag{1.13}$$

where K is the number of data points, $\hat{I}$ is the modeled value and I is comparison 'ground truth'.

1.3 Dissertation structure

In chapter 2, we review existing radiative transfer Monte Carlo Models and explore how could some of them be applied to the current research.

Chapter 3 presents a comprehensive spectral radiative model for the atmosphere using line-by-line two-flux approximation. Air-mass correction due to earth curvature effect is also considered

Chapter 4 investigates the impact of aerosol loadings and anisotropic characteristics on atmospheric radiation and presents a scaling method to calibrate the aerosol effects using Monte Carlo algorithm.

Chapter 5 presents a "SCOPE" method to estimate spectral cloud optical properties using satellite data and ground measurements. Ice cloud correction and multiple cloud layer scenarios are also considered.

Chapter 6 presents a now-casting convolutional neural networks model for global horizontal irradiance using the cloud information derived from the satellite data using the method proposed in Chapter 4.

Chapter 2

Monte Carlo Simulation Models

2.1 Basics for Monte Carlo Radiative Transfer

The framework of radiative transfer (RT) in the atmosphere builds the theoretical foundation for many topics in atmospheric and energy research. The variation of solar irradiance is caused by differential heating of the sun as well as the atmospheric dynamics, which would in turn influence atmospheric dynamics [20].

When radiation propagates through some medium, there will be interactions between the propagating light or photons and the medium [19]. Studying this process requires a rigorous mathematical theory that describes accurately the nature of the radiation field. Due to complexities and uncertainties, the radiative transfer within participating media presents some of the most mathematically challenging heat transfer problems [21]. There are numerous methods of approximating radiative transfer, one of the most widely used ones is the Monte Carlo method. The Monte Carlo method is a general computational technique based on the statistical characteristics of physical processes, or of analogous models that mimic physical processes [22]. To solve the radiative transfer problem, discrete energy parcels are simulated to traverl over relatively long distance along a straight path before interaction with medium. The solutions of such problems are based on tracing the history of statistically meaningful random sample of photons from their points of emission or incidence to their points of extinction [23].

The Monte Carlo method is a method of directly simulating mathematical or physical relations by random processes. One advantage of the Monte Carlo method is the simple structure of the computation

algorithm. A certain program is written to carry out N random trials. These trials are independent with each other and then the results of all trials are averaged [24]. In particular, for radiative heat transfer, the method is based on simulating a finite number of photon bundles that carry finite amount of radiative energy using a random number generator. The physical events that happen in the life of a photon bundle such as emission, absorption, reflection, are decided using probability density functions derived from physical laws.

Energy Representation for Photon Bundles

According to the quantum theory, energy is transferred through radiation in terms of energy particles (photons). Based on this theory, the Monte Carlo method simulates the energy transfer by observing the behavior of a number of photon bundles. In solving this type of problems with Monte Carlo method, the energy of each emitted photon bundle w is represented by $w = E/n$, where E is the total emissive power $E = \sigma T^4$ and n is the number of histories used for the simulation.

The emissions of the photons are from either surfaces or a volume of emitting gases. During the simulations, in order to obtain localized results, these surfaces and volumes must be divided into some sub-regions. The emissive power for a surface element E_{bw} and for a gas volume E_{bg} can be evaluated by using the following equations:

$$E_{bw} = \varepsilon \sigma T_w^4 A, \tag{2.1}$$

$$E_{bg} = 4 k_a \sigma T_g^4 V, \tag{2.2}$$

where ε is the surface emittance and k_a is the absorption coefficient of the gas volume.

Random Sampling Techniques for Monte Carlo Simulation

The essence of the Monte carlo method is sampling from probability distribution functions (PDFs). To sample a quantity x_0 from a PDF $p(x)$, which is normalized over all x, we can use the fundamental principle which is[25]:

$$\xi = \int_a^{x_0} p(x) dx = P(x_0), \tag{2.3}$$

where ξ is a random number samples uniformly from the range of 0 to 1, a is the lower limit of the range over which x is defined and $P(x_0)$ is the cumulative probability distribution function. There are many ways to

generate random numbers, but for convenience, in the present study, a built-in random number generator in MATLAB is applied.

Random numbers can be used to choose not only the starting location but also the emitting angles and optical depths. It is important to notice that, the angles and optical depths are not necessarily evenly sampled over their possible ranges. For a photon emitted from a surface to an isotropic medium, random number relations for the azimuthal angle ϕ and the zenith angle θ are given by the following relations:

$$\theta = \cos^{-1}(\sqrt{\xi_\theta}), \qquad \phi = 2\pi\xi_\phi, \tag{2.4}$$

For a photon emitted from an isotropic gas, the range of its zenith angle is extended to $[0, \pi]$. Now the random number relations for these angles are[25]:

$$\theta = \cos^{-1}(2\xi_\theta - 1), \qquad \phi = 2\pi\xi_\phi, \tag{2.5}$$

To sample the optical depth that a photon travels before being absorbed or scattered, we need to find the probability that a photon travels for an optical depth τ without interacting other molecules:

$$p(\tau)d\tau = e^{-\tau}d\tau, \tag{2.6}$$

Applying the fundamental principle:

$$\xi = \int_0^{\tau_0} e^{-\tau}d\tau = 1 - e^{-\tau_0} \longrightarrow \tau_0 = -\ln(1-\xi) = -\ln(\xi), \tag{2.7}$$

where ξ is the uniform random number in the range of [0, 1] so $1-\xi$ has the same distribution.

The application of these sampling methods will be explained in the following sections.

Tracing Approaches

Ray-tracing procedure can be divided to forward approach and backward approach. Forward approach is the standard or traditional approach and starts at the point of emission, then track the ray through the medium until the ray energy is totally absorbed by the medium or the enclosing surface. The backward approach performs the simulations in reverse and considers only rays that impact the surface of interest [21].

The forward methods are more straight forward and can easily simulate problems of great complexity with reasonable efficiency. However, if only the radiative intensity hitting a small range of solid angles is required, the backward method is more desirable [23].

Collision-Based Approach

In this approach, an emitted photon bundle is assumed to travel undisturbed until it collides with a molecule or particle, where it is either absorbed or scattered. If absorption occurs, the energy contained in the entire photon bundle is converted to thermal field in medium or surface while if scattering occurs, the photon bundle continues to travel until the next collision. The key variable that is sampled randomly is the distance traveled between consecutive collisions which is determined by cumulative probability distribution functions based on radiative properties of the medium [21]. According to Cashwell and Everett [26] this distance is denoted by d_c and can be sampled as:

$$d_c = -\Lambda_\lambda \ln r = -\frac{\ln r}{\kappa_{a\lambda}}, \tag{2.8}$$

where Λ_λ is the photon mean free path at wavelength λ and $\kappa_{a\lambda}$ is the absorption coefficient of current medium at wavelength λ. However, this general approach may be problematic when applied to an atmosphere that is either optically thin or optically thick. In either case, the application of some biasing scheme is required.

After determining d_c it is necessary to calculate the distance to the nearest boundary d_b from the starting position along the direction of propagation. Once it is done, d_b and d_c are compared so that to determine whether the collision occurs in the current zone, or before crossing the boundary. If $d_c < d_b$, the collision happens in the current zone. As a result of collision, the photon may either be absorbed or scattered. The probability that the photon scatters is determined by single scattering albedo. if scattering occurs, a new random scattering direction is generated according to incoming ray direction and scattering phase function. On the other hand, the energy of the photon bundle is converted to the thermal field if absorbed by media. If $d_c > d_b$, the photon is advanced to the boundary and its coordinates are updated accordingly:

$$x' = x + r_x d_b, \qquad y' = y + r_y d_b, \qquad z' = z + r_z d_b, \tag{2.9}$$

If this boundary is an external boundary, the energy contained in this photon bundle is recorded as an outgoing energy flux or energy absorbed by a surface. If the external surface is non-black, the possible reflection should also be considered. On the other hand, if an internal boundary is passed, energy flux to next zone can

be recorded if needed. Moreover, d_c and d_b are also updated according to new parameters in the new zone or volume. The remaining distance to collision can be expressed as:

$$d_c' = \frac{\Lambda_\lambda'}{\Lambda_\lambda}(d_c - d_b) = \frac{\kappa_{a\lambda}}{\kappa_{a\lambda}'}(d_c - d_b), \tag{2.10}$$

where Λ_λ' and $\kappa_{a\Lambda}'$ are the mean free path and absorption coefficient in the zone just entered. Then the updated distance to collision and new distance from the updated position to next boundary are compared. This process continues until either a collision or escape occurs [27].

Path Length Approach The pathlength method attempts to increase speed and statistical accuracy in the results by allowing each ray to contribute to every region it traverses. In this approach, a photon bundle is no longer considered as a whole; instead, a fraction of the photon bundle can be absorbed or scattered as it propagates [21].

The main idea of path length approach is more straight forward. Consider a bundle of photons being emitted in roughly the same direction from the same starting point. As this bundle travels a distance L throughout a medium, photons collide with molecules or particles such that the bundle is continuously losing photon from its initial population. The amount of power remaining in the bundle, $E_{remaining}$ after traveling a distance L through a absorbing scattering medium is:

$$E_{remaining} = E_{initial} \exp(-\kappa_e L), \tag{2.11}$$

where $E_{initial}$ is the power of the bundle prior to traveling the distance L and κ_e is the extinction coefficient, which includes absorption and scattering. Single scattering albedo is used to determine among the power lost along the traveling path how much power is absorbed and how much is scattered. The absorbed portion is added to the traversed region while the scattered portion is regarded as a new bundle that travels in a new scattering angle until it escapes or is fully absorbed. This method is particularly suitable for purely absorbing medium since scattering would take up a large portion of computational time. Through a purely absorbing medium with an absorption coefficient κ_a, the remaining power is:

$$E_{remaining} = E_{initial} \exp(-\kappa_a L), \tag{2.12}$$

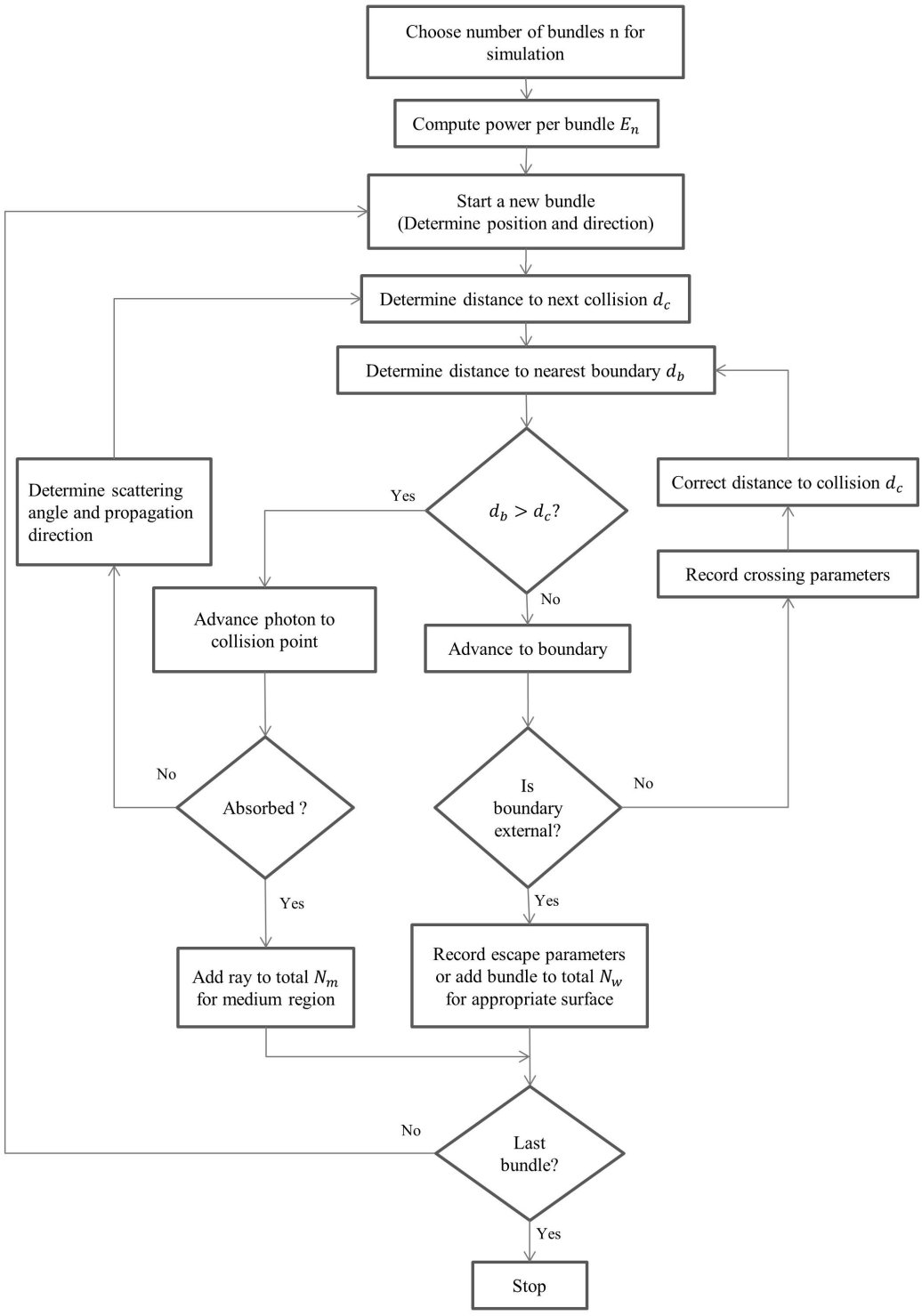

Figure 2.1: Schematic Overview of forward collision-based approach.

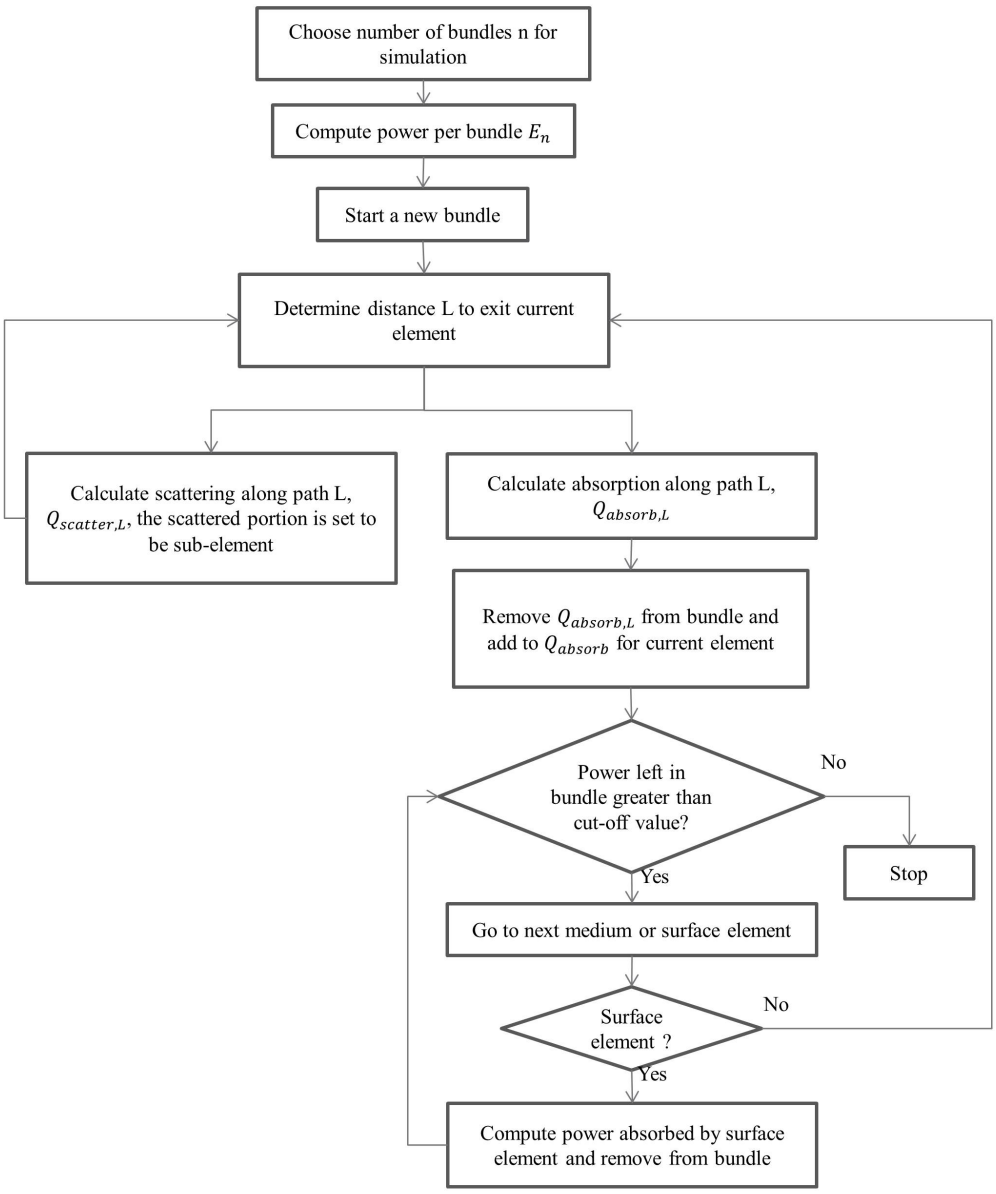

Figure 2.2: Schematic Overview of forward pathlength approach.

If the absorption coefficient varies along the path, Equation 2.12 can be written as:

$$E_{remaining} = E_{initial} \exp(-\int_0^L \kappa_a ds), \tag{2.13}$$

2.1.1 Backward Approach

Unlike forward approaches, the backward or reverse approach considers only rays that impact the target surface hence is problem-specific. This approach is relatively young, is first applied to radiation transfer problems in 1972, by Collins, et al [28]. Then Adam and Kattawar adopted this concept in their study of spherical shell atmospheric radiation and provided justifications [29]. In 1992, Walters and Buckius developed a comprehensive reverse Monte Carlo solution for computing the radiative emission of a generalized enclosure containing non-homogeneous absorbing emitting and scattering media [30] [31] based on the principle of reciprocity in radiative transfer described by Cashwell [32]. Later on, Ambirajan and Look employed a backward Monte Carlo estimator to describe the multiple scattering of a polarized, narrow light beam by a plane-parallel medium [33]. More recently, Modest gave a more comprehensive formulation for backward Monte Carlo simulations in radiative transfer in 2003 which is capable of treating media with diffuse or collimated irradiation, media with point or line sources and describes this method in terms of standard ray tracing (similar to forward collision-based approach) as well as energy partition (similar to forward pathlength method) [34]. In the same year, Lu and Hsu applied this approach for transient radiative transfer. Most recently, Yong, et al. presented a novel approach that combines backward and forward Monte Carlo simulation strategies to study the vector radiative transfer in the participated medium.

In this approach, a ray or photon bundle is launched from a specified terminal position in a randomly generated direction, which is referred to as the line of sight. The distance along the line of sight to the next event can be determined. For a emitting absorbing medium, radiation is emitted all along this line segment and the radiation leaving any point along this segment will undergo exponential attenuation [21]. The radiant intensity due to a single photon bundle arriving at the terminal point along the line-of-sight direction is given by:

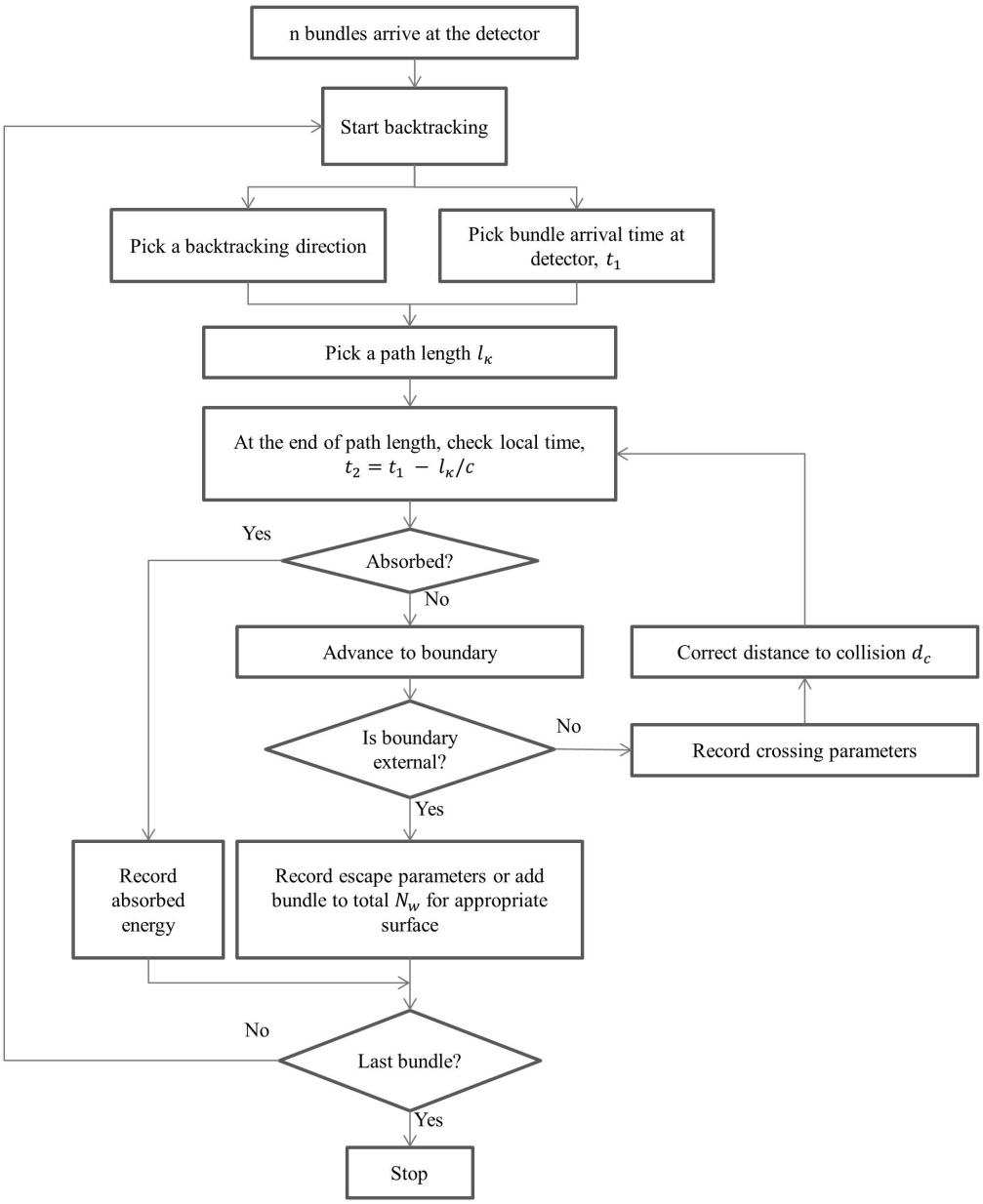

Figure 2.3: Schematic Overview of backward Monte Carlo approach.

$$I_n = \begin{cases} \int_0^{l_\kappa} \kappa(\mathbf{r}')I_b(\mathbf{r}')\exp(-\kappa l')dl', & l_\kappa < L \\ \\ \epsilon I_b(\mathbf{r_w}) + \int_0^{L} \kappa(\mathbf{r}')I_b(\mathbf{r}')\exp(-\kappa l')dl', & l_\kappa \geq L \end{cases}$$

where I_n is the radiant intensity of nth bundle, l_κ is the path length, or distance to the next event, L is the geometric length or distance to the boundary, $\mathbf{r}$ is the position vector, ϵ is the surface emittance of the boundary, I_b is the black-body intensity. Once this process has been completed for N bundles, the total intensity of each bundle is combined to determine the average intensity. This approach is particularly powerful for the measurement problem in which a large object is imaged over a smaller detector surface [23].

2.2 Monte Carlo Simulation in Spherical Configuration

Monte Carlo method is supposed to be able to simulate photon transport in various configurations. In a plane-parallel configuration, as we assumed for the atmosphere, a normal MC algorithm as Fig. 2.1 shows is used. For a spherical case, like in the real atmosphere, sightly more complicated steps are applied as Fig. 2.4 shows. The boundary of each atmospheric layer is represented as radius R_i.

2.3 Performance Comparison

There are two measures of performance for Monte Carlo simulations: variance of the results and the time required for solution. These two measures are normally competing with each other - fast computation time often means lower accuracy and larger variance while variance of results can be driven to near zero with drastically increasing computer time. An inclusive figure of merit is the product $\sigma^2 T$. A decreasing figure of merit indicates a reduction in variance , a reduction in computation time or both. The factors that influences this quantity are related only to the radiative parameters, geometric complexity and ray-tracing method.

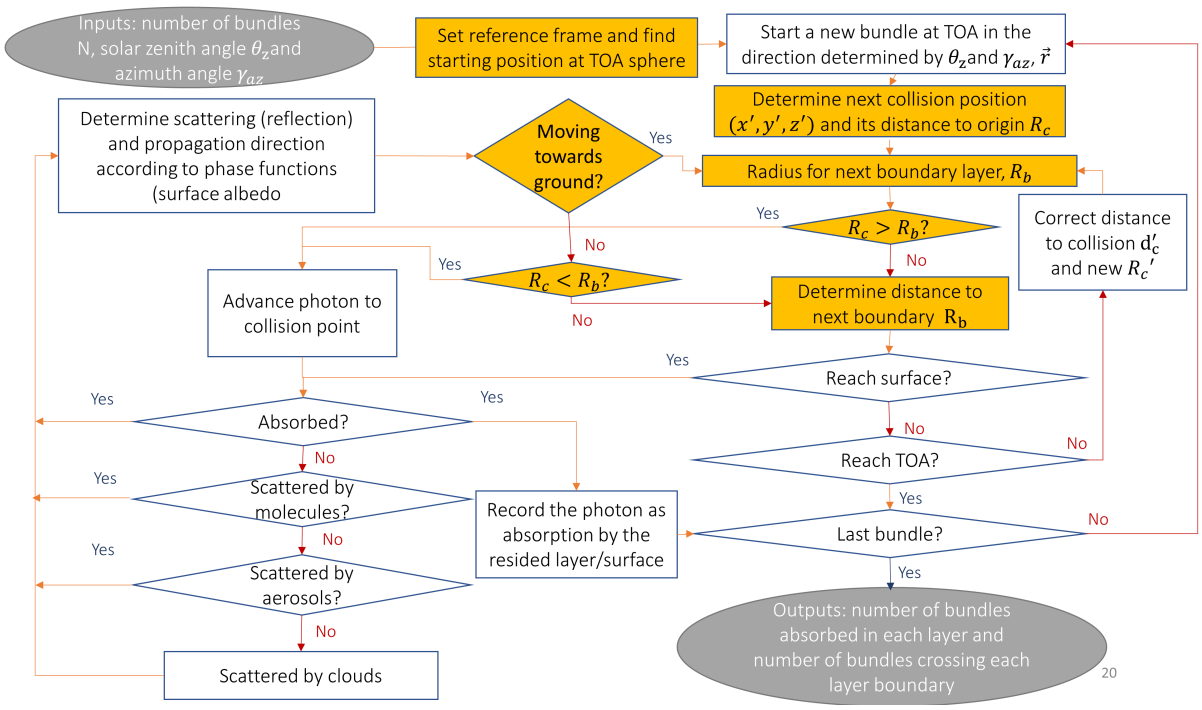

Figure 2.4: Flow chart for Monte Carlo simulation in spherical model configuration.

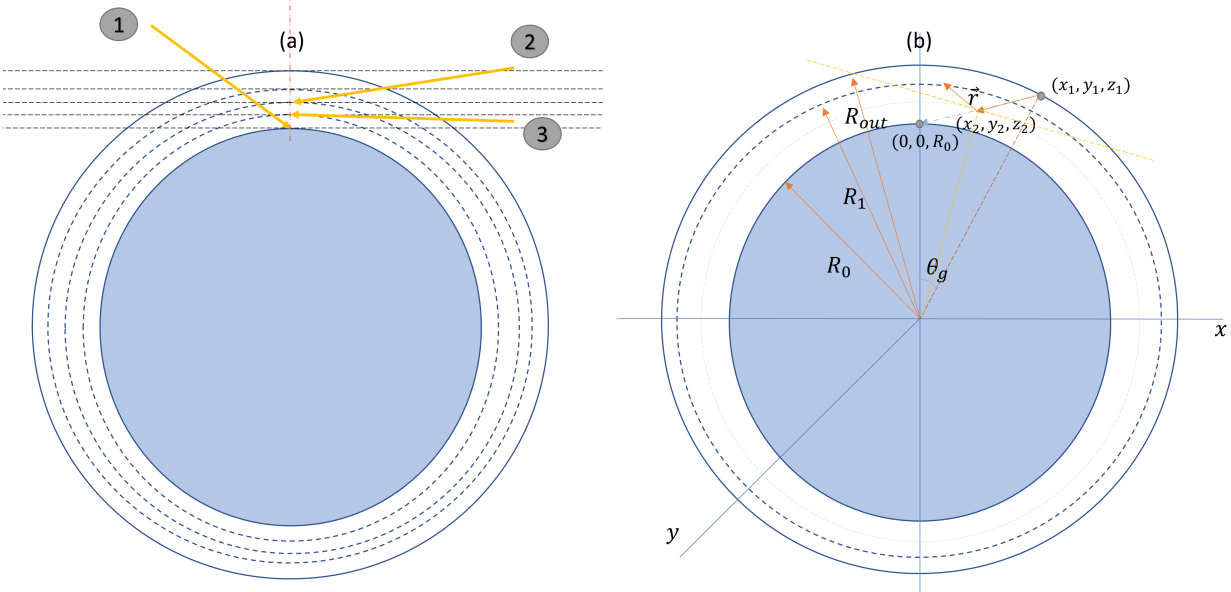

1. Most solar rays with zenith angle smaller than 85°,
2. Solar rays with zenith angle larger than 85°.
3. Solar rays with zenith angle larger than 90°. Some parts of the atmosphere will still be directly illuminated.

Figure 2.5: Interaction with solar rays in a spherical model configuration.

Chapter 3

Spectral modeling of longwave radiative transfer in the atmosphere

3.1 Introduction

Surface downwelling longwave irradiance (DLW) plays a critical role on weather and climate variability modeling, as well as on the heat balance design of solar power plants, of radiant cooling systems, and of the built environment [35]. Surface DLW can be measured directly by pyrgeometers, but pyrgeometers are not widely available in weather stations due to capital and calibration expenses. Furthermore, infrared radiation from the surroundings tend to complicate the installation of research-quality pyrgeometers. Because of the importance of surface DLW on the thermal balance of both agricultural and industrial environments, simplified models to estimate the so-called sky radiosity have been proposed (see [35] for an extensive review and up-to-date data-driven models). A simple-to-use parametric model with coefficients regressed from measurements can be used to calculate the ground level longwave irradiance with satisfactory accuracy. However, for locations without pyrgeometers, choosing a parametric model with regression coefficients estimated from the measurements of other locations may introduce bias errors because the surface level downwelling irradiance depends on local meteorological conditions. This work aims to develop a *minimal* model for calculating the atmospheric downwelling longwave radiation within the uncertainty of commonly used pyrgeometers.

A spectrally resolved radiative model is developed to calculate the interactions of longwave irradiance

with atmospheric molecules, aerosols and clouds. When compared with other available radiative models [36–39], this model incorporates the most up-to-date HIgh Resoluton TRANsmission (HITRAN) molecule spectral line data combined with the Mlawer-Tobin-Clough-Kneizys-Davies (MT_CKD) water vapor and CO_2 continuum model [40, 41]. The proposed model incorporates Mie theory to calculate aerosol extinction coefficients and asymmetry factors, with modifications for aerosol size distribution and refraction index corrections for aerosol - water vapor interactions. The complete model is a robust and inexpensive tool to study longwave radiative heat transfer in the atmosphere. The robustness of the model is derived from the use of a standard atmosphere that can be readily adjusted for surface altitude. The model was designed to be applied to the Air Force Geophysics Laboratory (AFGL) midlatitude summer atmosphere by simple displacement of the local altitude above sea level (see Section 3.5.4 for details).

In building the complete model, a recognition that most of the complexity related to the mutual interactions between atmosphere layers, aerosols and participating gases cannot be resolved without a detailed spectral consideration of each component. Thus, the model adopts high-resolution line-by-line data for all main constituents.

The monochromatic thermal exchange between layers is calculated by an isotropic *two-stream* (or *two-flux*) model [42–45], where the piecewise monochromatic sections of the spectrum are first treated as perfect emitters before they are recursively corrected by the application of a reflective plating algorithm. This application of the plating algorithm originally proposed by Edwards [46] for radiative enclosures allows for expedited incorporation of piecewise non-black portions of the spectrum, including aerosol scattering. To the best of our knowledge, this type of recursive plating algorithm has not been applied to atmospheric radiation problems before. The combination of reusable transfer factors, high-resolution line-by-line spectral data, and the recursive plating algorithm results in a fast computational method that can be performed in real-time (within realistic time constants of change of temperature and relative humidity) by a mini computer (e.g., Raspberry Pi or BeagleBone), thus allowing for the development of smart instruments for DLW calculations as opposed to relying on sparse pyrgeometer data networks. Because the proposed model incorporates the main thermal radiation contributions in the atmosphere, it can also be used to study the sensitivity of DLW to greenhouse gases (H_2O, CO_2 and CH_4) and aerosols by adjusting the parameters in the model without the need for local telemetry.

The main components of the proposed spectral model are outlined in Table 3.1, and the detailed

methodology used for evaluation is presented in Section 3.2 to 3.4, and the model is validated in Section 3.5.

Table 3.1: Main components of the proposed model

Model components	**Descriptions**	**Presented in**
Main radiative model	Divides the atmosphere into N parallel layers, constant σ coordinate system for pressures	Section 3.2
Temperature profile	AFGL profiles	Section 3.2
Concentration profiles of atmospheric gases	AFGL profiles corrected to current surface concentrations of gases	Section 3.2
Spectral resolution	Wavenumber range from 0 to 2500 cm^{-1} with resolution of 0.01 cm^{-1}	Section 3.2
Aerosol absorption and scattering coefficients	Evaluated using Mie theory	Section 3.3.1
Aerosol size distribution	Assumes equivalent spherical shape for the aerosols, size distribution follows a bimodal lognormal distribution	Section 3.3.1
Aerosol interaction with water vapor	Aerosol size and refraction index change with respect to water vapor concentration in the surrounding air	Section 3.3.1
Clouds absorption and scattering coefficients	Evaluated using Mie theory	Section 3.3.2
Clouds droplet size distribution	Assumes equivalent spherical shape for the droplets, size distribution follows a Gamma distribution	Section 3.3.2
Spectral line absorption coefficients	HITRAN 2016 absorption coefficients for 7 atmospheric gases: H_2O, CO_2, O_3, CH_4,N_2O, O_2 and N_2 evaluated at layer-averaged pressures and temperatures. Data retrived via HITRAN API	Section 3.3.3
Continuum absorption coefficients	MT_CKD continuum model for H_2O, CO_2, O_3 and O_2	Section 3.3.3
Monochromatic flux of scattering medium	Scale anisotropic scattering to isotropic by δ-M approximation, use exponential integral as transferfactors, blackbody emissive power of each layer is evaluated at layer average temperature	Section 3.4.1
Broadband flux	Integrated monochromatic flux density	Section 3.4.2

3.2 Model structure

This section presents the method used to divide the atmosphere into N parallel layers, with pressure, temperature and constituent profiles along the z direction. As depicted in Fig.3.1, the atmosphere is divided

in N layers, extending from the surface to an altitude with approximately zero pressure. The layers are determined according to pressure, not physical height. The monochromatic downwelling and upwelling fluxes q_n^- and q_n^+ are evaluated at layer boundaries. The monochromatic extinction coefficient κ_e, single scattering albedo $\tilde{\rho}$ and asymmetry factor g for each layer are evaluated using layer-averaged pressure $\bar{P}_n$ and temperature $\bar{T}_n$ values.

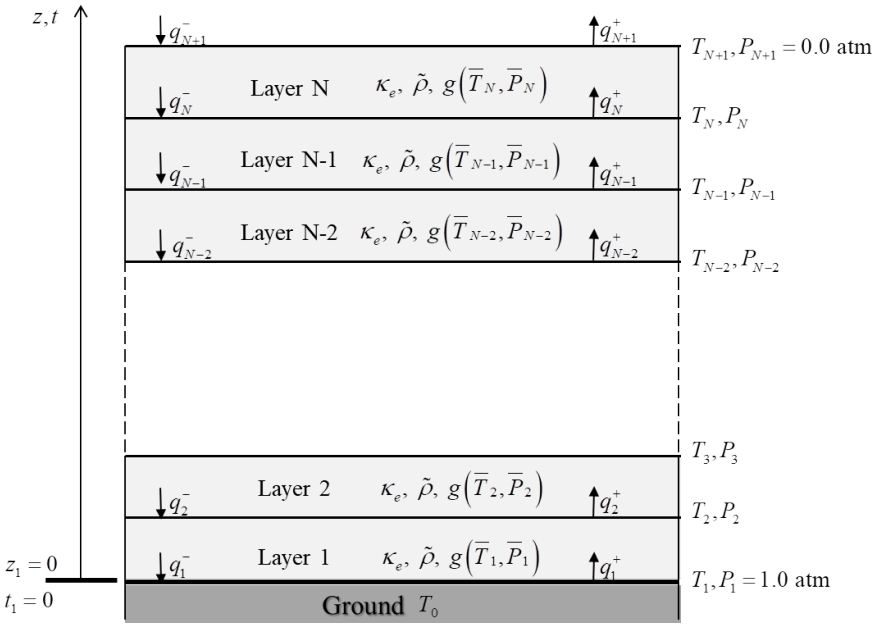

Figure 3.1: Schematic representation of the multilayer model of the Earth-atmosphere system. The vertical coordinates of altitude and normal optical path are labeled as z and t, respectively. The surface altitude z and normal optical depth t are equal to zero.

A constant σ_n coordinate system designates the average pressure $\bar{P}_n$ and the pressure of each layer boundary [47, 48]:

$$\begin{aligned} \sigma_n &= \frac{2N - 2n + 1}{2N}, \\ \bar{P}_n &= \sigma_n^2(3 - 2\sigma_n), \\ P_n &= \bar{P}_{n-0.5}, \end{aligned} \tag{3.1}$$

and the pressure-averaged temperature of layer n is:

$$\bar{T}_n = \frac{T_n(P_n - \bar{P}_n) + T_{n+1}(\bar{P}_n - P_{n+1})}{P_n - P_{n+1}}. \tag{3.2}$$

AFGL profiles [49] are used for the temperature profile T_n and pressure profile P_n (Fig. 3.2). Since the pressure is defined by Eq. (3.1), the z_n and T_n are inferred from P_n according to the AFGL profiles. The AFGL midlatitude summer profile is used throughout this work, unless noted otherwise.

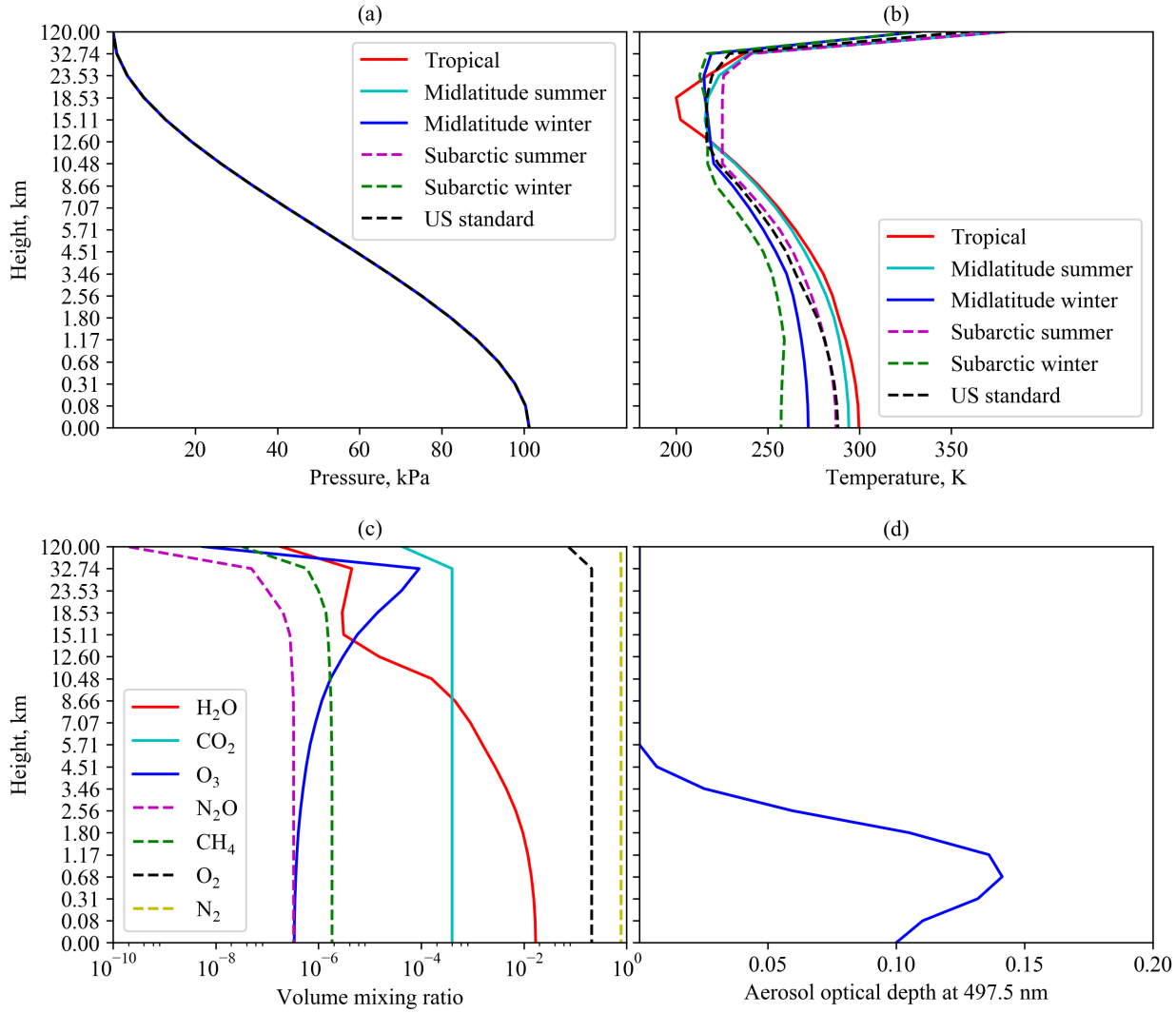

Figure 3.2: (a) AFGL pressure profiles; (b) AFGL temperature profiles; (c) AFGL midlatitude summer gas profiles corrected for current surface concentration of gases (shown for 70% surface relative humidity); (d) aerosol optical depth at 497.5 nm.

Seven participating atmospheric gases are considered: water vapor (H_2O), carbon dioxide (CO_2), ozone (O_3), methane (CH_4), nitrous oxide (N_2O), oxygen (O_2) and nitrogen (N_2). The vertical profiles of those gases are also based on AFGL profiles [49], with modifications to account for various surface conditions

(Fig. 3.2). For each gas, the vertical profile of the volumetric mixing ratio is given by

$$w(z) = w^*(0)\frac{w_{\mathrm{AFGL}}(z)}{w_{\mathrm{AFGL}}(0)}, \tag{3.3}$$

where $w^*(0)$ represents the current surface volumetric mixing ratio. For H_2O, $w^*(0)$ is a function of surface relative humidity ϕ_1, such that

$$w^*_{\mathrm{H_2O}}(0) = \frac{\phi_1 P_s(T_1)}{P_1}. \tag{3.4}$$

The saturated water vapor pressure P_s (Pa) for a given temperature T (K) is calculated using the August-Roche-Magnus (ARM) expression [50]

$$P_s(T) = P_{\mathrm{ARM}}\ \exp\left(\frac{c_{\mathrm{ARM}}(T-273.15)}{T-30.11}\right), \tag{3.5}$$

where $P_{\mathrm{ARM}} = 610.94$ Pa and $c_{\mathrm{ARM}} = 17.625$.

For the other gases we use current averaged values for the volumetric mixing ratios $w^*(0)$ in the troposphere [51]: $w^*_{\mathrm{CO_2}}(0) = 399.5$ ppm, $w^*_{\mathrm{O_3}}(0) = 337$ ppm, $w^*_{\mathrm{CH_4}}(0) = 1834$ ppb, $w^*_{\mathrm{N_2O}}(0) = 328$ ppb, $w^*_{\mathrm{O_2}}(0) = 0.209$ and $w^*_{\mathrm{N_2}}(0) = 0.781$.

The vertical aerosol concentration profile is adopted from [52] using the Cloud Aerosol LIDAR and Infrared Pathfinder Satellite Observations (CALIPSO) over North America. As mentioned before, we cover the wavenumber range from 0 to 2500 cm^{-1} in order to include all bands of practical interest, and adopt a spectral resolution of 0.01 cm^{-1}.

3.3 Monochromatic volumetric optical properties of atmosphere layers

The atmosphere is assumed to contain seven participating gases plus aerosols and clouds. For longwave radiation, scattering by gas molecules can be neglected [53], so only scattering by aerosols and clouds are considered here. The monochromatic volumetric extinction coefficient, the single scattering albedo and asymmetry factor for each layer are expressed as (the subscript for wavenumber ν is omitted in this

section for expediency),

$$\begin{aligned}
\kappa_e &= \kappa_a + \kappa_s = \kappa_{a,\text{gas}} + \kappa_{a,\text{aer}} + \kappa_{s,\text{aer}} + \kappa_{a,\text{cld}} + \kappa_{s,\text{cld}}, \\
\tilde{\rho} &= \frac{\kappa_{s,\text{aer}} + \kappa_{s,\text{cld}}}{\kappa_e}, \\
g &= \frac{\kappa_{s,\text{aer}} g_{\text{aer}} + \kappa_{s,\text{cld}} g_{\text{cld}}}{\kappa_{s,\text{aer}} + \kappa_{s,\text{cld}}},
\end{aligned} \tag{3.6}$$

where coefficients of gases, aerosols and clouds are evaluated at layer averaged temperature $\bar{T}_n$ and pressure $\bar{P}_n$. The absorption and scattering coefficients of aerosols and clouds follow Mie theory behavior, as detailed in the following sections 3.3.1 and 3.3.2. The method we use to calculate absorption coefficients for gas mixtures is detailed in 3.3.3.

3.3.1 Absorption and scattering coefficients of aerosols

The monochromatic absorption coefficient $\kappa_{a,\text{aer}}$, scattering coefficient $\kappa_{s,\text{aer}}$ and asymmetry factor g_{aer} of aerosols are functions of aerosol size distribution and aerosol refractive index.

The size distribution of aerosol particles in the model follows a standard lognormal distribution [1],

$$\frac{dN}{d\ln r} = r\frac{dN}{dr} = rn(r) = \sum_{i=1}^{I} \frac{N_i}{\sqrt{2\pi}\ln\sigma_i} \exp\left[-\frac{1}{2}\left(\frac{\ln(r/r_{m,i})}{\ln\sigma_i}\right)^2\right]. \tag{3.7}$$

For each mode i, $r_{m,i}$ (μm) is the mode radii, σ_i (μm) is the standard deviation and N_i is the mode amplitude. For internally mixed aerosols (aerosols mixed as a homogeneous material that reflects the chemical and physical average of all the contributing components [54]), the size distribution can be expressed bimodally with $I = 2$ and $r_{m,1} = 0.135$ μm, $r_{m,2} = 0.995$ μm, $\sigma_1 = 2.477$ μm, $\sigma_2 = 2.051$ μm [1]. The smaller particle mode is dominant given that $N_1 = 10^4 N_2$. Since the composition and size distribution of atmospheric aerosols vary greatly with time and locations [55], aerosols modeled in [1] are used to demonstrate the proposed model. Different aerosol compositions and size distributions can be easily implemented in the model.

To account for the changes of aerosol size distribution and refractive index due to the interaction with water vapor, a growth factor g_f is used. The value of g_f is a function of surrounding relative humidity as tabulated in Table 3.2 [1]. The value of g_f is multiplied by the mode radii $r_{m,i}$ in Eq. (3.7) to account for size changes, and is used in the following relation to account for the change of refractive index m [1]:

$$m = m_0 g_f^{-3} + m_w(1 - g_f^{-3}), \tag{3.8}$$

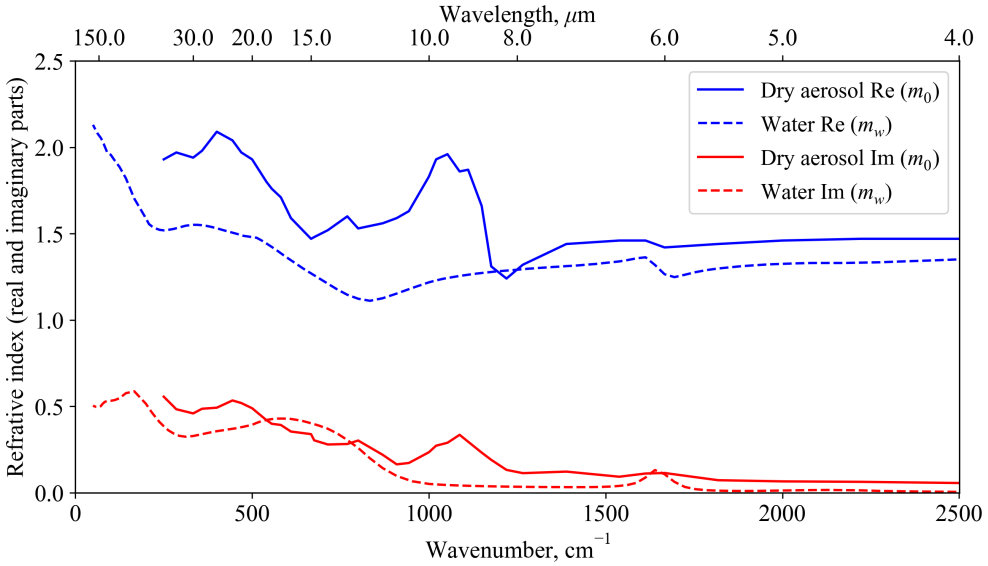

Figure 3.3: Refractive index of aerosols and liquid water [1, 2]. Re(·) and Im(·) stand for the real and imaginary parts of the index.

where the subscript 0 stands for dry aerosols, and the subscript w stands for liquid water. The spectral refractive index of dry aerosols m_0 and liquid water m_w are plotted in Fig. 3.3. Data for these plots were obtained from Ref. [1] and [2], respectively.

Table 3.2: Growth factor of aerosols [1]. Starred values are interpolated in the proposed model.

RH,%	0	10	20	30	40	50	60	70	80	90	100
g_f	1.000*	1.000*	1.000*	1.031	1.055	1.09	1.15	1.26	1.554	1.851	2.151*

The scattering of longwave radiation by aerosols is modeled by Mie theory, assuming equivalent spherical shapes for the aerosols [53]. The extinction, scattering, absorption efficiencies and asymmetry parameter of a single aerosol particle are calculated using standard Mie theory relations [53, 56],

$$
\begin{aligned}
Q_e &= \frac{2}{x^2}\sum_{n=1}^{\infty}(2n+1)\mathrm{Re}(a_n+b_n),\\
Q_s &= \frac{2}{x^2}\sum_{n=1}^{\infty}(2n+1)\left(|a_n|^2+|b_n|^2\right),\\
Q_a &= Q_e - Q_s,\\
g &= \frac{4}{x^2 Q_s}\left[\sum_{n=1}^{\infty}\frac{n(n+2)}{n+1}\mathrm{Re}(a_n a_{n+1}^{*}+b_n b_{n+1}^{*})+\sum_{n=1}^{\infty}\frac{2n+1}{n(n+1)}\mathrm{Re}(a_n b_n^{*})\right],
\end{aligned}
\tag{3.9}
$$

where the diacritic * stands for the complex conjugate; Re(·) stands for the real part of a complex number; x is the size parameter, $x = 2\pi\nu r$, where r (cm) is the radius of the aerosol and ν (cm^{-1}) is the wavenumber; a_n and b_n are the Mie coefficients, which are a function of the size parameter x and the aerosol refractive index m.

Note that the above parameters are summations of infinite series, which are truncated after n_{max} terms in the computations to satisfy accuracy requirements. The criteria for the number of terms used is given by [56],

$$n_{\max} = \text{round}(x + 4x^{1/3} + 2). \tag{3.10}$$

When the magnetic permeability of the sphere is equal to the magnetic permeability of the ambient medium, the Mie coefficients a_n and b_n are given by [56],

$$\begin{aligned} a_n &= \frac{m^2 j_n(mx)[x j_n(x)]' - j_n(x)[mx j_n(mx)]'}{m^2 j_n(mx)[x h_n(x)]' - h_n(x)[mx j_n(mx)]'}, \\ b_n &= \frac{j_n(mx)[x j_n(x)]' - j_n(x)[mx j_n(mx)]'}{j_n(mx)[x h_n(x)]' - h_n(x)[mx j_n(mx)]'}, \end{aligned} \tag{3.11}$$

where m is the refractive index of the aerosol relative to the ambient air; $j_n(z)$ is the spherical Bessel function of the first kind; $h_n(z)$ is the spherical Bessel related function, $h_n(z) = j_n(z) + y_n(z)i$ and $y_n(z)$ is the spherical Bessel function of the second kind.

The primes indicate derivatives with respect to the arguments, $z = x$ or $z = mx$, with the derivatives of the spherical Bessel functions being [57],

$$\begin{aligned} [z j_n(z)]' &= z j_{n-1}(z) - n j_n(z), \\ [z h_n(z)]' &= z h_{n-1}(z) - n h_n(z). \end{aligned} \tag{3.12}$$

For atmospheric aerosols with varying sizes, the volumetric absorption and scattering coefficients and asymmetry parameters correspond to integrated values of scattering/absorption efficiencies over all possible aerosol radii r [53],

$$\begin{aligned} \kappa_{a,\text{aer}} &= \int_0^\infty n(r) Q_a(r) \pi r^2 dr, \\ \kappa_{s,\text{aer}} &= \int_0^\infty n(r) Q_s(r) \pi r^2 dr, \\ g_{\text{aer}} &= \frac{1}{\kappa_{s,aer}} \int_0^\infty n(r) Q_s(r) \pi r^2 g(r) dr. \end{aligned} \tag{3.13}$$

The scattering and absorption coefficients of atmospheric aerosols are proportional to N_1, the first mode amplitude, as shown in Eqs. (3.7) and (3.13). Aerosol content in the atmosphere relates to aerosol optical depth (AOD) [58], which is defined as AOD = $\kappa_{e,\text{aer}}\bar{L}$ [59], where $\bar{L}$ is the scale height. Here we take the value of $\bar{L}$ to be 1,575 m, the annualized average value reported in [52] for the continental USA. If $\text{AOD}_{497.5} = 0.1$, aerosol extinction coefficient at 497.5 nm is then $\kappa_{e,\text{aer@497.5}} = \text{AOD}_{497.5}/\bar{L} = 6.35 \times 10^{-7}$ cm $^{-1}$. The value of N_1 in Eq. (3.7) is thus determined from $\kappa_{e,\text{aer@497.5}} = 6.35 \times 10^{-7}$ cm $^{-1}$. Figure 3.4 is a plot of the monochromatic extinction coefficient and optical depth of aerosols when $\text{AOD}_{497.5} = 0.1$ and relative humidity of 70%.

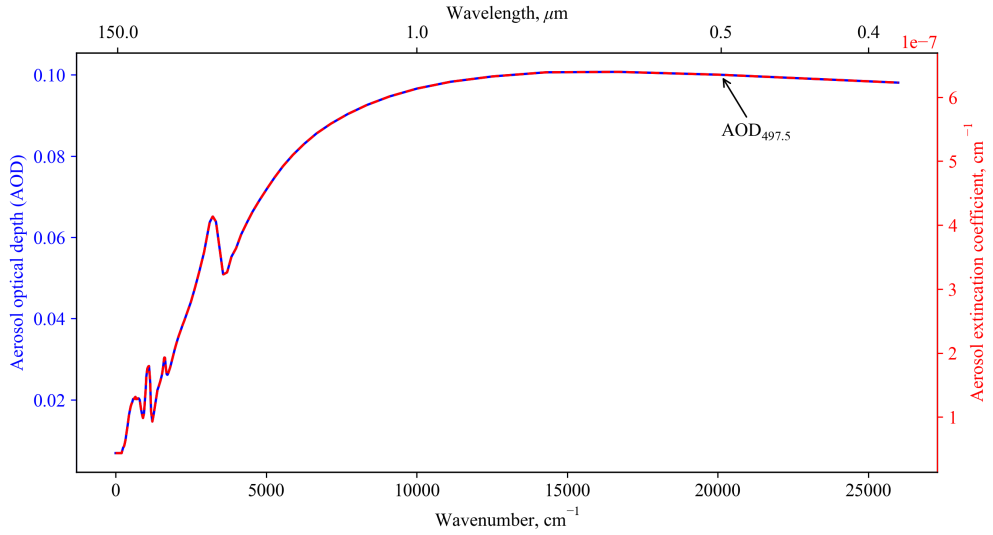

Figure 3.4: The monochromatic extinction coefficient and optical depth of aerosols when $\text{AOD}_{497.5}$ = 0.1 and 70% RH.

3.3.2 Absorption and scattering coefficients of clouds

Water clouds are modeled in the spectral radiative model using the similar methods as aerosols. Each water droplet is assumed to have a spherical shape, thus the absorption and scattering efficiencies of droplets are calculated using Mie theory [60] with the input of the refraction index of water retrieved from [2]. The absorption and scattering coefficients as well as the asymmetry factors of clouds are further calculated by integrating the efficiencies over a droplet size distribution [56]. The size distribution of droplets in clouds is

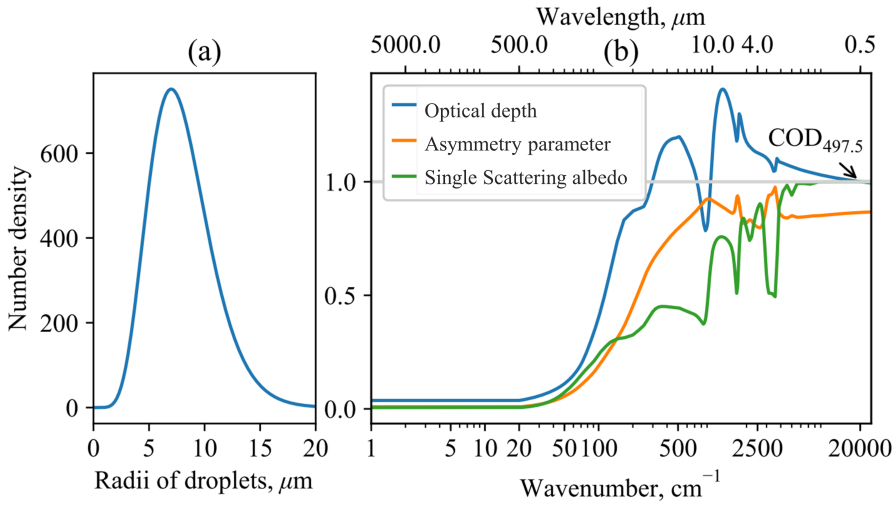

Figure 3.5: (a) Size distribution of droplets in the model clouds. (b) The spectral optical depth, single scattering albedo and asymmetry factor of model clouds for unity value of COD. The subscript 497.5 is omitted in the text for simplicity.

assumed to follow the Gamma distribution [61–63],

$$n(r) = r^{1/\sigma_e - 3} \exp\left(-\frac{r}{r_e \sigma_e}\right), \tag{3.14}$$

where r_e and σ_e are the effective radius and variance, respectively. For modelling purpose, $r_e = 10\,\mu$m and $\sigma_e = 0.1$, as suggested in [63]. The spectral dispersion k used by some modelers to represent the spread of droplet size (instead of σ_e) is defined as $k = (1/\sigma_e - 2)^{-1/2}$. When $\sigma_e = 0.1$, $k = 0.354$, which is a typical value for marine and continental clouds [62]. The size distribution of water droplets is shown in Fig. 3.5 (a).

In the model, clouds are treated as overcast and placed into layers with a predefined optical depth at 497.5 nm defined as $\text{COD} = \kappa_{e,\text{cld}} \Delta H_c$ where ΔH_c is the height of the clouds. The spectral optical depth, single scattering albedo and asymmetry factor of clouds are shown in Fig. 3.5 (b) for COD = 1.0.

3.3.3 Absorption coefficients of a mixture of atmospheric gases

The volumetric absorption coefficient κ_a (cm^{-1}) of a gas mixture is [53, 64],

$$\kappa_{a,\text{gas}} = \sum_i \rho_i \kappa_i^* = \sum_i \rho_i \left[\kappa^*_{\text{cont,i}} + \kappa^*_{\text{line,i}}\right], \tag{3.15}$$

where ρ_i (g cm^{-3}) is the partial density of gas i which is integrated over a layer; κ_i^* (cm^2 g^{-1}) is the mass absorption coefficient of gas i, which is the summation of continuum absorption coefficient $\kappa^*_{\text{cont,i}}$ and spectral line absorption coefficient $\kappa^*_{\text{line,i}}$.

The spectral line absorption coefficients $\kappa^*_{\text{line,i}}$ are obtained from HITRAN database using the HITRAN API [40, 65]. We use a Lorentz profile with line wing cut-off set to 25 cm^{-1} as suggested by [41, 66, 67] to properly account for the continuum absorption for water vapor. Although the Lorentz line shape is not strictly valid for high altitudes, the contributions from higher altitudes to the surface DLW is small enough that the error in assuming Lorentz line shapes across the atmosphere is negligible (see next Chapter for more details).

The continuum absorption coefficient of water vapor is the summation of self continuum and foreign continuum coefficients,

$$\kappa^*_{\text{cont,H}_2\text{O}} = \kappa^*_{\text{self,H}_2\text{O}} + \kappa^*_{\text{frgn,H}_2\text{O}}. \tag{3.16}$$

The continuum absorption spectral density functions C^0 at reference conditions are obtained from the MT_CKD model [41] and plotted in Fig.3.6 (a). For conditions with temperature T and pressure P, the spectral density function is,

$$C(T,P) = C_{\text{self}}(T,P) + C_{\text{frgn}}(T,P) = \frac{P}{P_0}\frac{T_0}{T}\left[w_{\text{H}_2\text{O}} C^0_{T_0,\text{self}} \left(\frac{C^0_{T_{\text{ref}},\text{self}}}{C^0_{T_0,\text{self}}} \right)^{\frac{T-T_0}{T_{\text{ref}}-T_0}} + (1-w_{\text{H}_2\text{O}}) C^0_{T_0,\text{frgn}} \right], \tag{3.17}$$

where $T_0 = 296$ K, $P_0 = 1$ atm, $T_{\text{ref}} = 260$ K; $w_{\text{H}_2\text{O}}$ is the molar fraction of water vapor; $C^0_{T_0,\text{self}}$,$C^0_{T_{\text{ref}},\text{self}}$ and $C^0_{T_0,\text{frgn}}$ are the reference spectral density function in Fig.3.6 (a).

To get the mass absorption coefficients, a 'radiation field' R_f is applied [39, 41],

$$R_f = \begin{cases} 0.5\nu\eta, & \text{for } \eta \le 0.01, \\ \nu \frac{1-\exp(-\eta)}{1+\exp(-\eta)} & \text{for } \eta \le 10, \\ \nu, & \text{all other conditions,} \end{cases} \tag{3.18}$$

where η is a non-dimensional parameter defined as $\eta = \nu/(T/c_{r2})$ with $c_{r2} = 1.439$ cm K being the second radiation constant [41].

The continuum mass absorption coefficient for water vapor is then,

$$k^*_{\text{cont,H}_2\text{O}} = C(T,P)\, R_f. \tag{3.19}$$

Figure 3.6 (b) plots the spectral and continuum absorption coefficients of pure water vapor, showing that continuum absorption dominates in the atmosphere window from 8 μm to 14 μm.

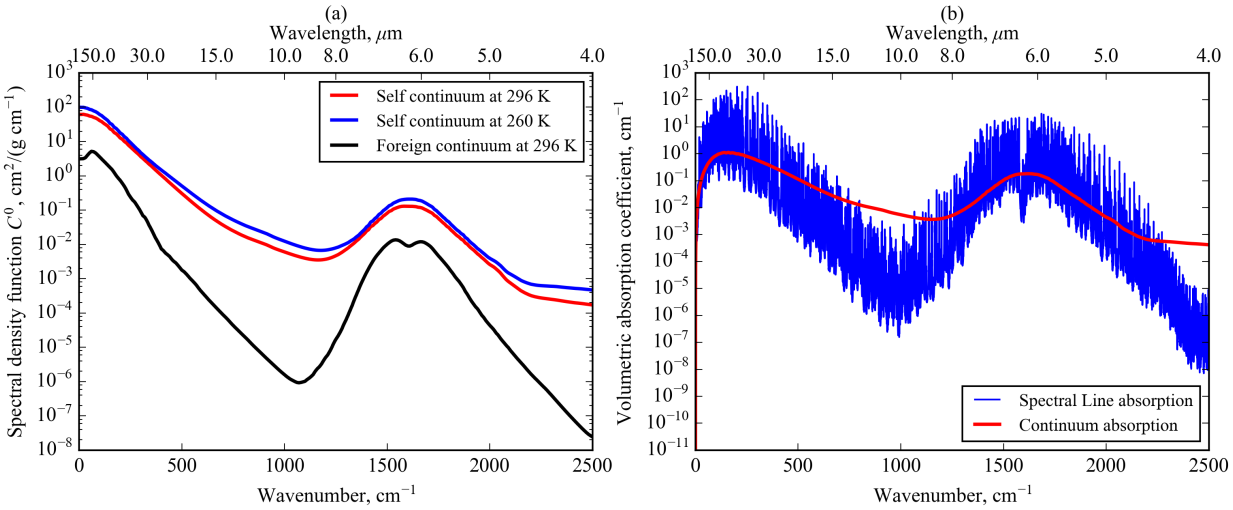

Figure 3.6: (a) The continuum absorption spectral density function C^0 for water vapor at selected conditions. (b) Spectral line and continuum absorption coefficients for water vapor at 1 atm and 288 K.

The continuum absorption spectral density functions C^0 at reference condition for CO_2 are obtained from the MT_CKD model [41] and plotted in Fig.3.7 (a). For conditions with temperature T and pressure P, the spectral density function is,

$$C(T,P) = w_{\text{CO}_2} C^0_{T_{\text{ref2}}} f_c \frac{P}{P_0} \frac{T_0}{T} \left(\frac{T}{T_{\text{ref2}}} \right)^{f_t}, \tag{3.20}$$

where $T_{\text{ref2}} = 246$ K; w_{CO_2} is the molar fraction of CO_2; $C^0_{T_{\text{ref2}}}$ is the reference spectral density function in Fig.3.7 (a); f_c and f_t are the spectral and temperature correction factor obtained from [41], respectively. The continuum mass absorption coefficient for CO_2 is then,

$$k^*_{\text{cont,CO}_2} = C(T,P)\, R_f, \tag{3.21}$$

Figure.3.7 (b) plots the spectral and continuum absorption coefficients of pure CO_2, showing that continuum absorption dominates in the spectral from 6 μm to 8 μm.

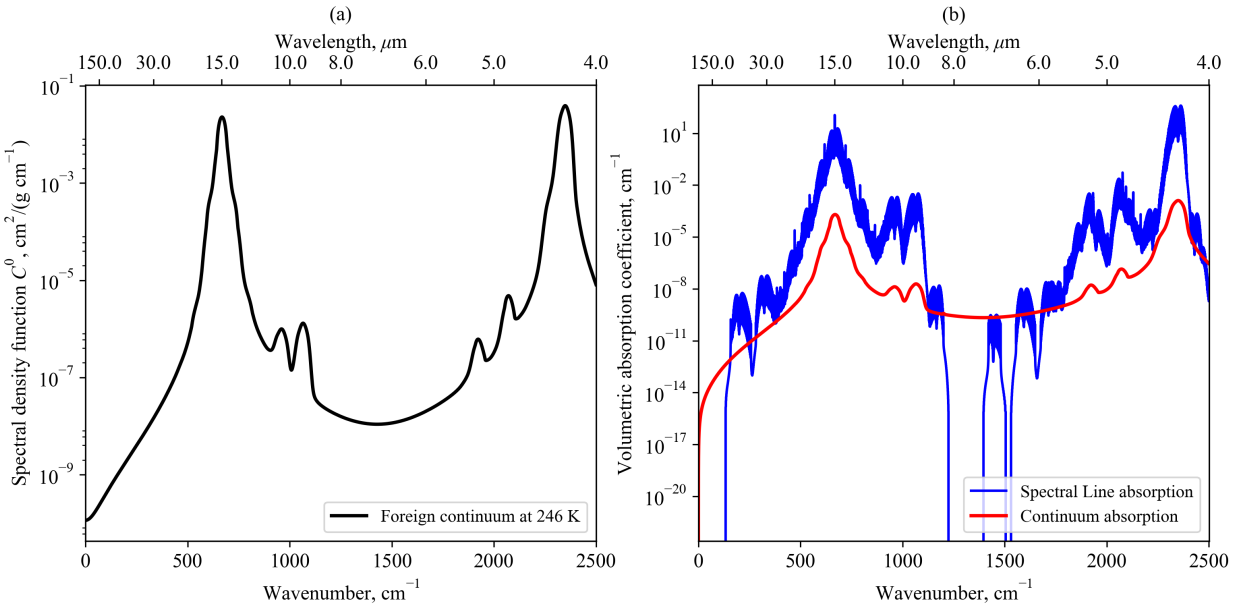

Figure 3.7: (a) The continuum absorption spectral density function C^0 for CO_2 at selected condition. (b) Spectral line and continuum absorption coefficients for CO_2 at 1 atm and 288 K.

3.4 Radiative upwelling and downwelling fluxes

This section presents the complete method used to calculate monochromatic downwelling and upwelling fluxes at each layer boundary in a scattering atmosphere. The broadband longwave fluxes is the integration of monochromatic fluxes over the range of wavenumbers considered (0 – 2500 cm^{-1}).

3.4.1 Monochromatic fluxes

This subsection details the method used to calculate downwelling and upwelling fluxes in a scattering medium from the irradiance G_i and radiosity J_i of each atmospheric layer.

For Earth's atmosphere, the albedo for single scattering is large in some spectral regions under cloud-free skies as shown in Fig. 3.8, thus scattering cannot be completely neglected even though the aerosol scattering effects for longwave radiation are never dominant. For longwave radiation, the asymmetry parameter ranges from 0.02 to 0.75 as shown in Fig. 3.8, therefore the δ-M approximation is used to scale

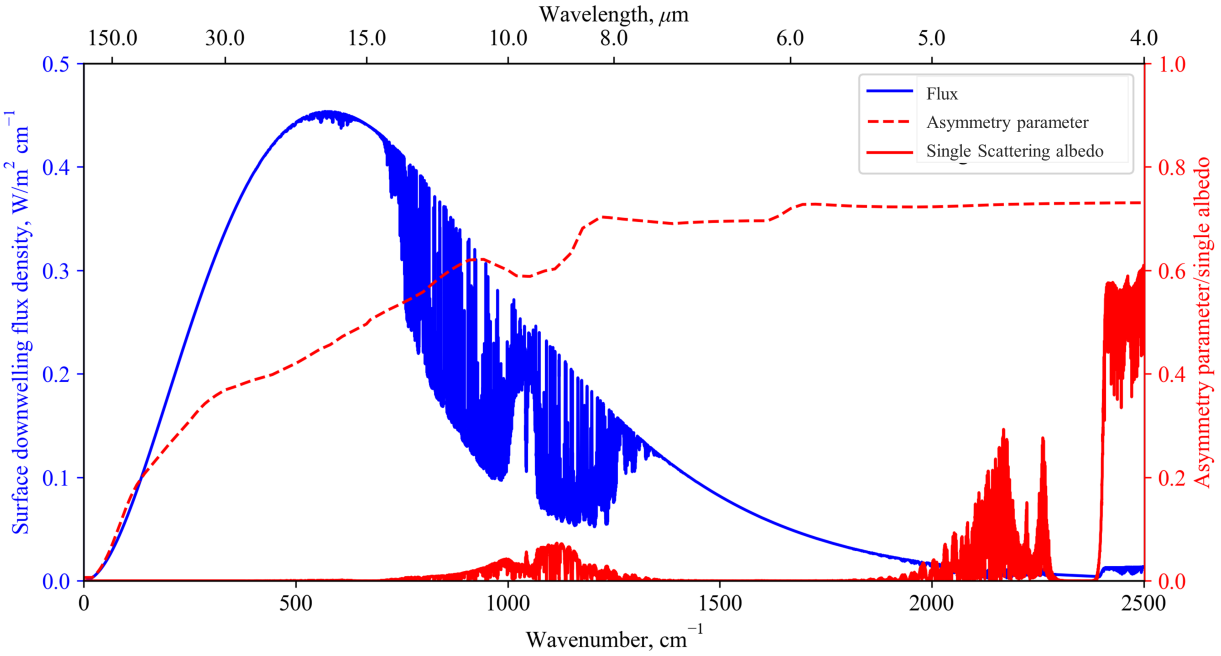

Figure 3.8: The spectral surface downwelling flux density, single scattering albedo and asymmetry parameter of the nearest atmosphere layer, for surface RH = 70% and $AOD_{497.5} = 0.1$.

anisotropic scattering to isotropic before applying the following algorithm for flux calculation. The δ-M approximation scales the extinction coefficient and the single scattering albedo using [68],

$$\begin{aligned} \hat{\kappa_e} &= (1-\tilde{\rho}g)\kappa_e, \\ \hat{\tilde{\rho}} &= \frac{\tilde{\rho}(1-g)}{1-\tilde{\rho}g}. \end{aligned} \tag{3.22}$$

After the scaling, isotropic scattering is assumed in the proposed model to reduce computational complexity.

For each layer n with a single scattering albedo $\hat{\tilde{\rho}}_n$ and extinction coefficient $\hat{\kappa}_{e,n}$, the irradiance G_n and radiosity J_n are,

$$\begin{aligned} G_n &= \sum_{j=0}^{N+1} \mathcal{F}_{n,j} J_j, \\ J_n &= (1-\hat{\tilde{\rho}}_n)\pi \bar{I}_{b,n} + \hat{\tilde{\rho}}_n G_n, \end{aligned} \tag{3.23}$$

where $\mathcal{F}_{n,j}$ is the transfer factor between layer n and layer j, and $\pi\bar{I}_{b,n}$ is the averaged blackbody emissive

flux of the layer, which is taken to be $\pi I_b(\bar{T}_n)$. The symbol I_b (W m m^{-2} sr^{-1}) is used for the monochromatic intensity in wavenumber basis defined by Eq.(1.2). Note that j values range from 0 to $N+1$ where layer 0 represents the ground layer and optical depth t_0 is taken to be negative infinity ($-\infty$). Layer $N+1$ represents the outer space layer and optical depth t_{N+2} is taken to be positive infinity ($+\infty$).

The transfer factors $\mathcal{F}_{n,j}$ are derived as follows. The monochromatic attenuation of intensity along a path s for an isotropic scattering medium is (wavenumber ν is omitted),

$$\frac{dI}{ds} = \hat{\kappa_e}(1-\hat{\bar{\rho}})I_b + \hat{\kappa_e}\hat{\bar{\rho}}\bar{I} - \hat{\kappa_e}I, \tag{3.24}$$

where $\hat{\kappa_e}$ (cm^{-1}) is the extinction coefficient (δ-M scaled), $\hat{\bar{\rho}}$ is the single scattering albedo (δ-M scaled), $\bar{I}$ is the averaged intensity over all solid angles, $\bar{I} = 1/4\pi \iint_0^{4\pi} I d^2\omega$.

The radiosity J and irradiance G of a volume are,

$$J = (1-\hat{\bar{\rho}})\pi I_b + \hat{\bar{\rho}}\pi\bar{I}; \qquad G = \int_0^s e^{-t_{s'}} J(s')ds', \tag{3.25}$$

where the optical depth $t_{s'} = \int_0^{s'} \hat{\kappa_e}(s'')ds''$.

For a plane parallel layer of atmosphere as shown in Fig. 3.9, the irradiance is expressed using *transfer factors*,

$$G_n = \sum_j J_j \mathcal{F}_{n,j} = \sum_j J_j \frac{1}{4\pi} \iint_0^{4\pi} \left[e^{t_s - t_{s,j}} - e^{t_s - t_{s,j+1}}\right] d^2\omega, \tag{3.26}$$

where the transfer factor between layer n and layer j is defined as

$$\mathcal{F}_{n,j} = \frac{1}{\Delta t_{s,n}} \int_{t_s} \int_0^{2\pi} d\phi \int_\theta \left[e^{t_s - t_{s,j}} - e^{t_s - t_{s,j+1}}\right] \frac{\sin\theta d\theta}{4\pi} dt_s. \tag{3.27}$$

Let $u = 1/\cos\theta$, then $du = \sin\theta/\cos^2\theta d\theta$ and $\sin\theta d\theta = du/u^2$. Note that the transfer factors given above can be written in terms of the normal optical depth $t = \int_0^z \hat{\kappa_e}(z')dz'$,

$$\begin{aligned}\mathcal{F}_{n,j} &= \frac{1}{2\Delta t_n} \int_t \int_1^\infty \left[e^{(t-t_j)u} - e^{(t-t_{s,j+1})u}\right] \frac{du}{u^2} = \frac{1}{2\Delta t_n} \int_{t_n}^{t_{n+1}} [E_2(t_j - t) - E_2(t_{j+1} - t)]dt \\ &= \frac{1}{2\Delta t_n} [E_3(|t_j - t_{n+1}|) + E_3(|t_{j+1} - t_n|) - E_3(|t_j - t_n|) - E_3(|t_{j+1} - t_{n+1}|)],\end{aligned} \tag{3.28}$$

where $E_2(\cdot)$ and $E_3(\cdot)$ correspond to the second and third exponential integral functions defined by $E_n(t) = \int_1^{+\infty} \exp(-ut)/u^n du$, which accounts for the integration of intensities over all solid angles of a hemisphere.

The transfer factor $\mathcal{F}_{n,n}$ for a layer to itself (due to emission and scattering) is,

$$\mathcal{F}_{n,n} = 1 - \frac{1}{2\Delta t_n}\int_{t_n}^{t_{n+1}} [E_2(t_n - t) - E_2(t_{n+1} - t)]dt = 1 - \frac{1 - 2E_3(|t_{n+1} - t_n|)}{2(t_{n+1} - t_n)}, \tag{3.29}$$

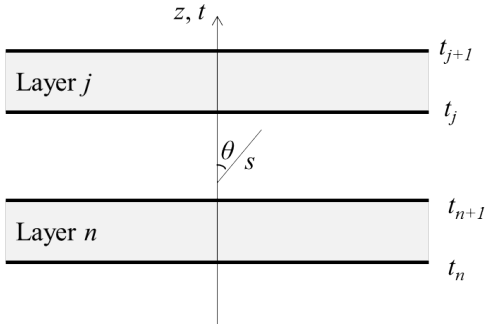

Figure 3.9: Plane parallel geometry and layer indices.

In sum, the transfer factors are,

$$\begin{aligned} A_n^*\mathcal{F}_{n,j} &= 2E_3(|t_j - t_{n+1}|) + 2E_3(|t_{j+1} - t_n|) - 2E_3(|t_j - t_n|) - 2E_3(|t_{j+1} - t_{n+1}|) \quad \text{for } j \neq n, \\ \mathcal{F}_{n,n} &= 1 - \frac{1 - 2E_3(t_{n+1} - t_n)}{2(t_{n+1} - t_n)} \qquad\qquad\qquad\qquad\qquad\qquad\qquad\qquad\qquad\qquad \text{for } j = n, \end{aligned} \tag{3.30}$$

where A_n^* is the equivalent surface area. For gas layers, $A_n^* = 4\hat{\kappa}_{e,n}\Delta z_n$ and for outer space and ground surface, $A_n^* = 1$.

The G_n and J_n are assembled in a matrix as depicted in the next page and the matrix equation is solved through matrix reduction.

$$
\begin{pmatrix} G_0 \\ G_1 \\ \vdots \\ G_N \\ G_{N+1} \\ J_0 \\ J_1 \\ \vdots \\ J_N \\ J_{N+1} \end{pmatrix} = \begin{pmatrix} 0 & 0 & \cdots & 0 & 0 & \mathcal{F}_{0,0} & \mathcal{F}_{0,1} & \cdots & \mathcal{F}_{0,N} & \mathcal{F}_{0,N+1} \\ 0 & 0 & \cdots & 0 & 0 & \mathcal{F}_{1,0} & \mathcal{F}_{1,1} & \cdots & \mathcal{F}_{1,N} & \mathcal{F}_{1,N+1} \\ \vdots & \vdots & \vdots & \vdots & \vdots & \vdots & \vdots & \vdots & \vdots & \vdots \\ 0 & 0 & \cdots & 0 & 0 & \mathcal{F}_{N,0} & \mathcal{F}_{N,1} & \cdots & \mathcal{F}_{N,N} & \mathcal{F}_{N,N+1} \\ 0 & 0 & \cdots & 0 & 0 & \mathcal{F}_{N+1,0} & \mathcal{F}_{N+1,1} & \cdots & \mathcal{F}_{N+1,N} & \mathcal{F}_{N+1,N+1} \\ \hat{\bar{\rho}}_0 & 0 & \cdots & 0 & 0 & 0 & 0 & \cdots & 0 & 0 \\ 0 & \hat{\bar{\rho}}_1 & \cdots & 0 & 0 & 0 & 0 & \cdots & 0 & 0 \\ \vdots & \vdots & \ddots & \vdots & \vdots & \vdots & \vdots & \vdots & \vdots & \vdots \\ 0 & 0 & \cdots & \hat{\bar{\rho}}_N & 0 & 0 & 0 & \cdots & 0 & 0 \\ 0 & 0 & \cdots & 0 & \hat{\bar{\rho}}_{N+1} & 0 & 0 & \cdots & 0 & 0 \end{pmatrix} \begin{pmatrix} G_0 \\ G_1 \\ \vdots \\ G_N \\ G_{N+1} \\ J_0 \\ J_1 \\ \vdots \\ J_N \\ J_{N+1} \end{pmatrix} + \begin{pmatrix} 0 \\ 0 \\ \vdots \\ 0 \\ 0 \\ (1-\hat{\bar{\rho}}_0)\pi\bar{I}_{b,0} \\ (1-\hat{\bar{\rho}}_1)\pi\bar{I}_{b,1} \\ \vdots \\ (1-\hat{\bar{\rho}}_N)\pi\bar{I}_{b,N} \\ (1-\hat{\bar{\rho}}_{N+1})\pi\bar{I}_{b,N+1} \end{pmatrix}
$$

With the values of J_j determined, the downward and upward fluxes are calculated as,

$$\begin{aligned} q_n^- &= \sum_{j=n}^{N+1} \mathcal{F}_{n,j}^* J_j, \\ q_n^+ &= \sum_{j=0}^{n-1} \mathcal{F}_{n,j}^* J_j, \end{aligned} \tag{3.31}$$

where $\mathcal{F}_{n,j}^*$ represent corrected transfer factors for downward and upward fluxes calculation. The values of $\mathcal{F}_{n,j}^*$ are calculated using Eq. (3.30) with the following rules for optical depth re-determination: (1) when calculating downward fluxes q_n^-, t_0 to t_{n-1} are taken to be $-\infty$; (2) when calculating upward fluxes q_n^+, t_{n+1} to t_{N+2} are taken to be $+\infty$.

Note that the above matrix reductions are calculated on every wavenumber, i.e. 0.25 million times with the resolution of 0.01 cm^{-1} for spectral range from 0 cm^{-1} to 2500 cm^{-1}. To make the model more computationally efficient, the irradiance G_n is solved directly by defining a modified transfer factor $\mathcal{F}_{n,j}^{**}$,

$$G_n = \sum_{j=0}^{N+1} \mathcal{F}_{n,j}^{**} \pi \bar{I}_{b,j}, \tag{3.32}$$

where the modified transfer factor $\mathcal{F}_{n,j}^{**}$ is calculated from the blackbody transfer factors $\mathcal{F}_{n,j}$ (Eq.(3.30)) recursively using a modified plating algorithm first proposed by Edwards [46] for radiative transfer within enclosures, but here adapted to radiative exchange between atmospheric layers with scattering.

The plating algorithm for scattering is initiated by assuming all layers to be non-scattering, i.e., having albedo $\hat{\bar{\rho}} = 0$,

$$G_n = \sum_{j=0}^{N+1} \mathcal{F}_{n,j} \pi \bar{I}_{b,j}. \tag{3.33}$$

Then the algorithm applies a single scattering albedo $\hat{\bar{\rho}}$ value to one layer at a time recursively, starting from layer 0. Non-scattering layers are skipped. Upon the plating of layer k, the radiosity is converted from $\pi \bar{I}_{b,k}$ to J_k, the sum of the emitted and scattered radiation,

$$J_k = (1 - \hat{\bar{\rho}}_n) \pi \bar{I}_{b,k} + \hat{\bar{\rho}}_n G_k^*, \qquad \text{and} \qquad G_k^* = \sum_{j \neq k} \mathcal{F}_{k,j} \pi \bar{I}_{b,j} + \mathcal{F}_{k,k} J_k, \tag{3.34}$$

where * denotes the corrected irradiance value after plating. Combining the relations in (3.34) gives the

radiosity,

$$J_k = \frac{1-\hat{\tilde{\rho}}_k}{D_k}\pi\bar{I}_{b,k} + \frac{\hat{\tilde{\rho}}_k}{D_k}\sum_{j\neq k}\mathcal{F}_{k,j}\pi\bar{I}_{b,j}, \tag{3.35}$$

where the denominator is $D_k = 1-\hat{\tilde{\rho}}_k\mathcal{F}_{k,k}$. When i is different from k, the new value of irradiance after plating layer k is given by,

$$G_i^* = \sum_{j\neq k}\mathcal{F}_{i,j}\pi\bar{I}_{b,j} + \mathcal{F}_{i,k}J_k = \sum_{j\neq k}\left[\mathcal{F}_{i,j} + \frac{\hat{\tilde{\rho}}_k}{D_k}\mathcal{F}_{i,k}\mathcal{F}_{k,j}\right]\pi\bar{I}_{b,j} + \frac{1-\hat{\tilde{\rho}}_k}{D_k}\mathcal{F}_{i,k}\pi\bar{I}_{b,k}. \tag{3.36}$$

The irradiance of layer k itself is then affected by the single scattering albedo,

$$G_k^* = (1-\hat{\tilde{\rho}}_k)\sum_{j\neq k}\mathcal{F}_{k,j}\pi\bar{I}_{b,j} + (1-\tilde{\rho}_{s,k})\mathcal{F}_{k,k}J_k = (1-\hat{\tilde{\rho}}_k)\sum_{j\neq k}\left[\mathcal{F}_{k,j} + \frac{\hat{\tilde{\rho}}_k}{D_k}\mathcal{F}_{k,k}\mathcal{F}_{k,j}\right]\pi\bar{I}_{b,j} + \frac{(1-\hat{\tilde{\rho}}_k)^2}{D_k}\mathcal{F}_{k,k}\pi\bar{I}_{b,k}. \tag{3.37}$$

Compare Eqs.(3.36) and (3.37) with Eq. (3.32) shows that four cases exist,

$$\begin{cases} \mathcal{F}^{**}_{i,j} = \mathcal{F}_{i,j} + \frac{\hat{\tilde{\rho}}_k}{D_k}\mathcal{F}_{i,k}\mathcal{F}_{k,j}, & i\neq k, j\neq k, \\ \mathcal{F}^{**}_{i,k} = \frac{1-\hat{\tilde{\rho}}_k}{D}\mathcal{F}_{i,k}, & i\neq k, j=k, \\ \mathcal{F}^{**}_{k,j} = (1-\hat{\tilde{\rho}}_k)\left[\mathcal{F}_{k,j} + \frac{\hat{\tilde{\rho}}_k}{D_k}\mathcal{F}_{k,k}\mathcal{F}_{k,j}\right] = \frac{1-\hat{\tilde{\rho}}_k}{D_k}\mathcal{F}_{k,j}, & i=k, j\neq k, \\ \mathcal{F}^{**}_{k,k} = \frac{(1-\hat{\tilde{\rho}}_k)^2}{D}\mathcal{F}_{k,k}, & i=k, j=k. \end{cases} \tag{3.38}$$

After plating, the modified transfer factors satisfy $\sum_{j=0}^{N+1}\mathcal{F}^{**}_{k,j} = 1-\hat{\tilde{\rho}}_k$.

3.4.2 Broadband fluxes

The broadband flux is the integration of monochromatic flux over the considered longwave wavenumber range,

$$\begin{aligned} \mathbf{q}_n^- &= \int_{\nu_1}^{\nu_2} q_n^-(\nu)d\nu, \\ \mathbf{q}_n^+ &= \int_{\nu_1}^{\nu_2} q_n^+(\nu)d\nu, \end{aligned} \tag{3.39}$$

where $q_n^-(\nu)$ / $q_n^+(\nu)$ is monochromatic downward / upward flux and ν (cm^{-1}) is wavenumber in the range of $\nu_1 = 0\ \mathrm{cm}^{-1}$ and $\nu_2 = 2500\ \mathrm{cm}^{-1}$. Broadband integration is evaluated using a trapezoidal rule.

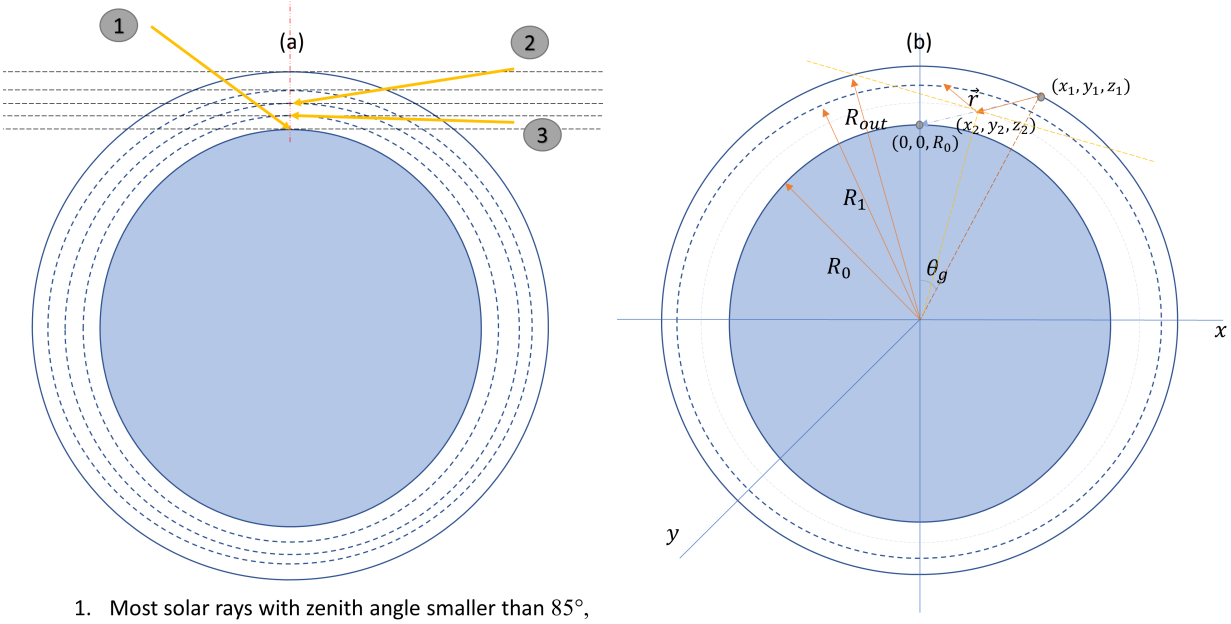

1. Most solar rays with zenith angle smaller than 85°,
2. Solar rays with zenith angle larger than 85°.
3. Solar rays with zenith angle larger than 90°. Some parts of the atmosphere will still be directly illuminated.

Figure 3.10: Spherical model Configuration of Earth's Atmosphere

3.5 Validation of the model

3.5.1 Validation of Plane-Parallel Assumption

In this model, a plane-parallel assumption is applied. However, in reality, the Earth is an ellipsoid and the atmosphere is curved. Fig. 3.10 shows the configuration of the Earth atmosphere and most cases are represented as Ray 1 with a zenith angle less than 85 degrees. The right figure of Fig. 3.10 shows the symbols used in spherical Monte Carlo simulation which is described in Sec. 2.2.

Fig. 3.11 shows the Monte Carlo simulation result that compares plane-parallel assumption and actual situation. For most solar rays less than 85^o, the Earth's curvature effect can be neglected. For solar zenith angles larger than 85^o, the attenuation of the direct solar beam is slightly overestimated in a plane-parallel atmosphere. For solar zenith angles larger than 90^o, some parts of the atmosphere will still be directly illuminated which is not possible using plane parallel geometry. In a spherical atmosphere, for an observation made at 20 km, there is no direct surface component until 4° below the local horizon. However, for the purpose of solar forecasting and modeling, those rare cases are not significant. Plane-parallel configuration is adequate.

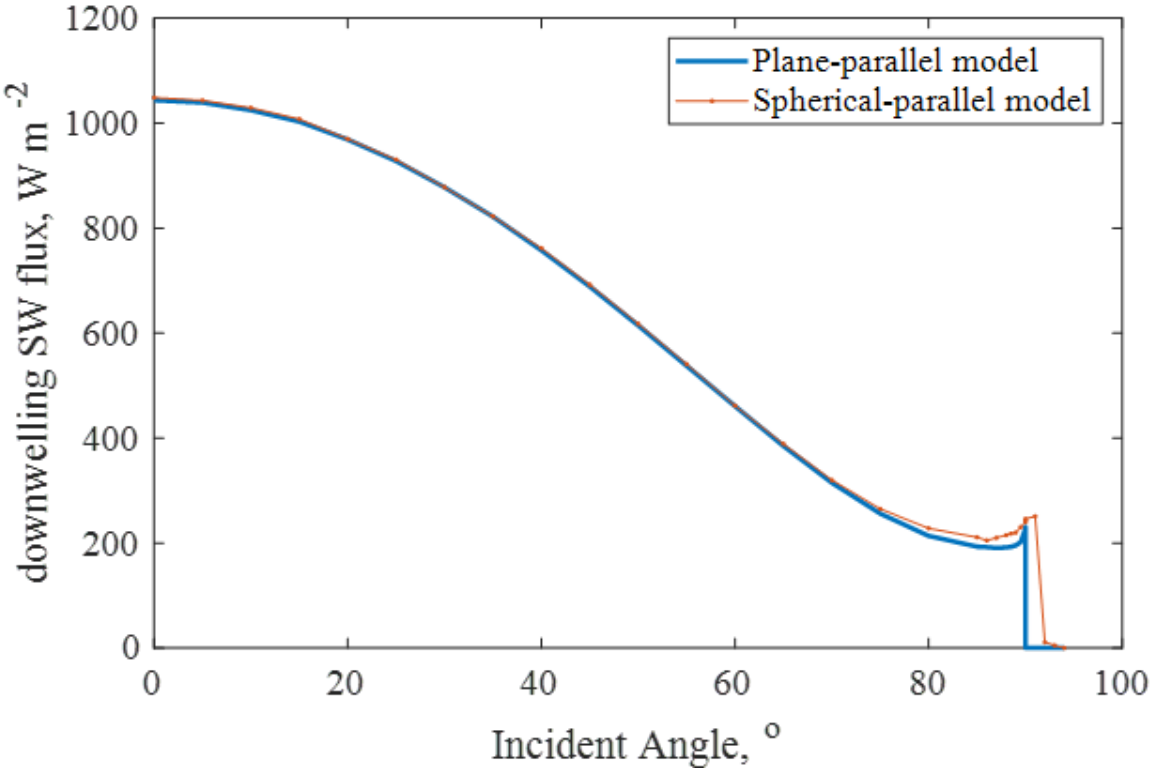

Figure 3.11: Comparison of the results in GHI for plane-parallel model and spherical-parallel model.

3.5.2 Grid convergence

The plane parallel model of the atmosphere assumes each layer to be homogeneous, so the accuracy of the model may be compromised if too few layers are considered. Increasing the number of layers increases model accuracy, but there is a number of layers after which further increase causes negligible effects on the overall results. As shown in Fig.3.12 below, the downward flux profile changes by less than 3 W m^{-2} when 18 or more atmospheric layers are used, indicating that grid convergence for DLW is achieved.

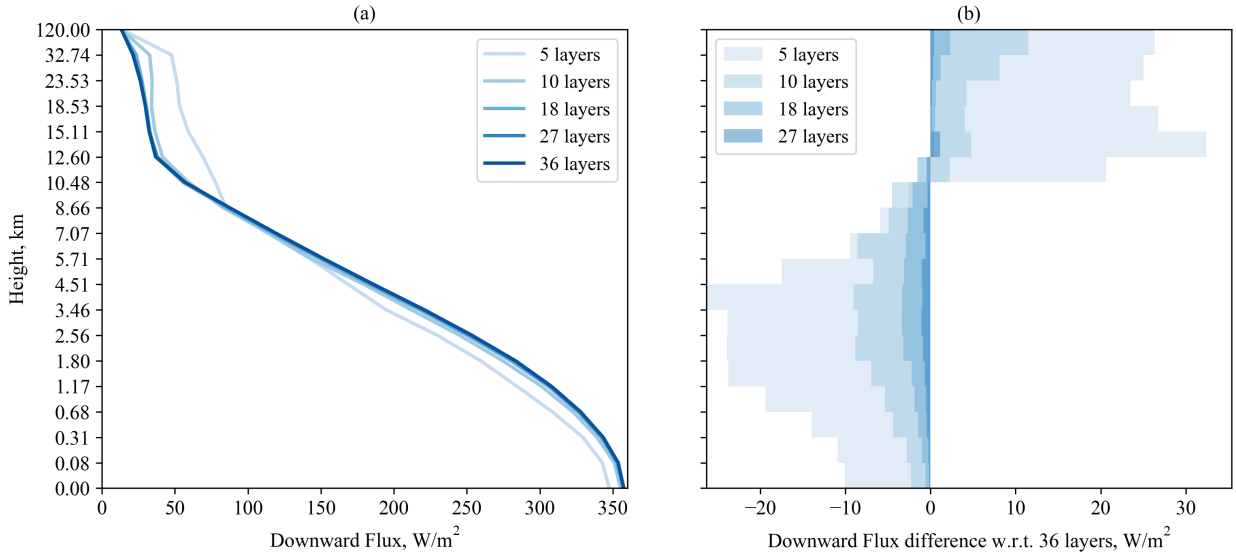

Figure 3.12: (a) Grid dependence on number of layers for broadband DLW; (b) Broadband DLW difference when compared to 36 layers. For this numerical example, surface relative humidity is 70% and $AOD_{497.5}$ is 0.1. The downwelling flux at the top of the atmosphere is from solar radiation.

3.5.3 Comparison with ICRCCM results

In this subsection we validate the proposed model against longwave results from the Intercomparison of Radiation Codes in Climate Models program (ICRCCM) [69]. Aerosols and solar longwave radiation are not included in ICRCCM results. The comparisons for selected cases are listed in Table 3.3, showing that the results of the proposed model are within 2.91% of the mean and within one standard deviation of ICRCCM results. The reference in Table 3.3 is the ICRCCM longwave results produced by Atmospheric Environmental Research, Inc. (AER), with data downloaded from [3]. The DLW flux profiles are plotted in Fig.3.13 (a) where the difference compared to AER ICRCCM results is smaller than ± 8.5 W/m^2 as shown in Fig.3.13 (b). Spectral comparison with results from AER ICRCCM results is plotted in Fig.3.13 (c). The

absolute difference is smaller than 0.035 W cm m^{-2} for all wavenumbers.

Table 3.3: Comparison of surface DLW with ICRCCM results. A midlatitude summer profile is used and the flux values have unit of W m^{-2}.

Case	Case description	ICRCCM Mean [69]	ICRCCM Std [69]	Reference [3]	This work
19	H_2O only, with continuum	326.23	14.06	333.92	335.74
20	H_2O only, without continuum	273.19	17.82	269.02	271.86
27	CO_2, H_2O, O_3 with 300 ppmv CO_2	343.18	8.21	346.91	346.78

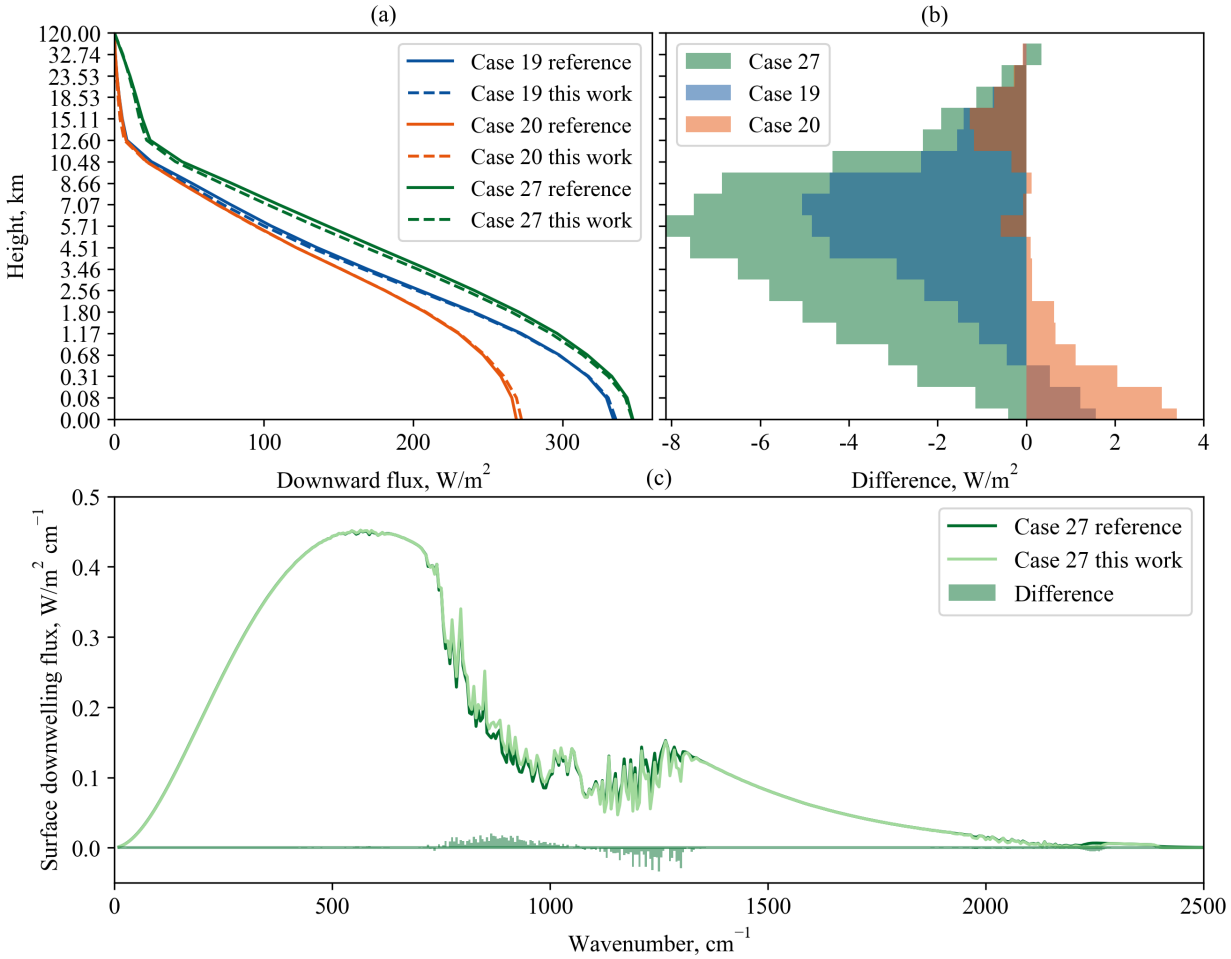

Figure 3.13: (a) Comparison of DLW profiles between the proposed model and Ref. [3]. (b) The difference of DLW fluxes with respect to Ref. [3]. (c) Spectral comparison of surface DLW flux densities.

3.5.4 Comparison with SURFRAD measurements

The comparisons in the previous section indicate the spectral model performs well for non-scattering atmospheres. In this section, we validate the spectral model for scattering atmosphere through a comparison with surface measurements of DLW from 7 SURFRAD stations for the year 2013. Aerosol content is assumed to be $AOD_{497.5} = 0.1243$ at the surface (the value 0.1243 is the 2013 annually averaged $AOD_{497.5}$ for all 7 stations, measured from the surface). Model results are also compared to a calibrated empirical model [35]. During clear sky daytime periods, the surface DLW can be empirically expressed as a function of surface water vapor partial pressure (in hPa),

$$\frac{\mathrm{DLW}}{\sigma T_a^4} = \varepsilon_{\mathrm{sky}} = c_1 + c_2\sqrt{P_w} = 0.598 + 0.057\sqrt{P_w}, \tag{3.40}$$

where $\varepsilon_{\mathrm{sky}}$ is the sky emissivity, $\sigma = 5.67\times10^{-8}\mathrm{W\,m^{-2}\,K^{-4}}$ is the Stefan Boltzmann constant and T_a (K) is surface air temperature. The coefficients c_1 and c_2 are obtained by regression from data from all 7 SURFRAD stations [35].

The proposed spectral model is then used to calculate surface DLW for each of the SURFRAD stations. The SURFRAD stations are located at different altitudes, and the effect of altitude differences is modeled by placing their ground surfaces in different layers according to their altitudes, as shown in Fig. 3.14. The model assumes the AFGL midlatitude summer profile, while the ground level relative humidity ranges from 5% to 100% in the increment of 5%, resulting in 20 different water vapor profiles. Thus, at each altitude z, there are 20 data points of water vapor partial pressure P_w and 20 data points of sky emissivity $\varepsilon_{\mathrm{sky}}$. A one-degree spline is used to interpolate the 20 data points, i.e. $\varepsilon_{\mathrm{sky}} = \mathrm{spl}(P_w)$ as shown in Fig. 3.15. At each station, the sky emissivity is calculated for different values of surface water vapor pressure using the spline interpolation. The surface DLW is then calculated from the sky emissivity using Eq. (3.40).

Model results are compared to measurements using three distinct error metrics proposed in section 1.2.4. Table 3.4 presents the MBE, RMSE and rRMSE of the empirical model and the spectral model when compared to measurements for each individual stations. Compared to the empirical model Eq. (3.40), which is regressed using aggregated data from all 7 stations, the proposed spectral model yields lower RMSE (rRMSE) for 6 out of 7 stations, indicating that the spectral model is able to capture the variability between stations. The model rRMSE ranges from 2.08% to 3.08% for all stations. The performance of the model

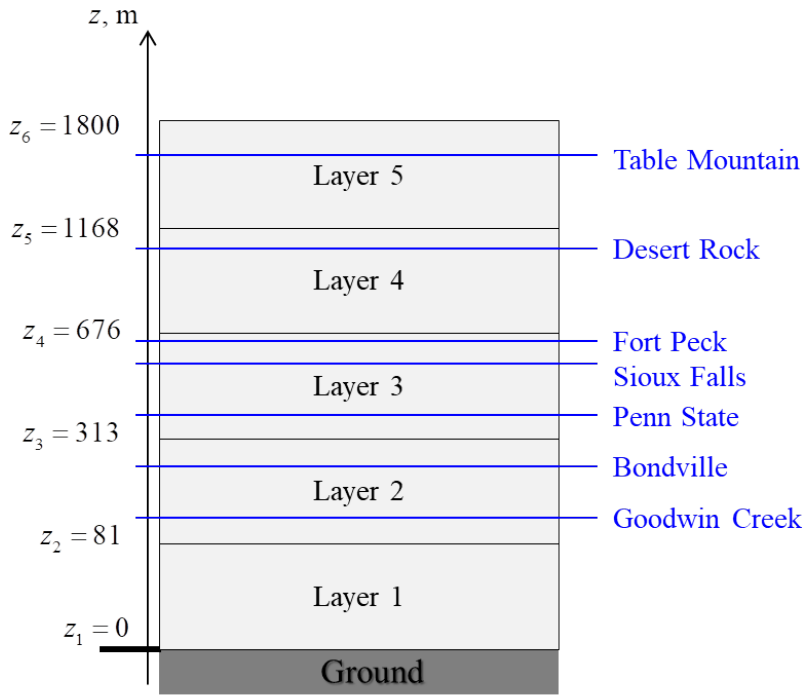

Figure 3.14: Illustration of ground surface locations of the 7 SURFRAD stations used in the model application.

is further illustrated in Fig. 3.15, where biases of the empirical model are more efficiently captured by the spectral model. Note that the proposed model can also be fine-tuned to different pressure-temperature profiles of the atmosphere, but these comparisons show that the model is robust enough to perform well for different microclimates using the standard AFGL midlatitude summer profile.

3.5.5 Comparison with CIRC results for cloudy period

The modeling of clear skies are validated against ICRCCM results as well as SURFRAD measurements, as presented in [60]. In this section, the modeling of cloudy skies are validated against the results from cloudy Case 6 and Case 7 of the Continual Intercomparison of Radiation Codes (CIRC) program [70].

Aerosols, solar longwave radiation and scattering by clouds are not included in the CIRC calculations [71]. The temperature, pressure, gas concentration profiles and cloud properties used in the proposed radiative model are obtained from the input files provided on the CIRC website [70] for validation purposes. The summarized model parameters and results of surface downwelling flux (DLW) for Case 6 and Case 7 are presented in Table 3.5. Scenario 1 recovers the CIRC model parameters except that six out of ten gases are included to be consistent with Ref. [60]. Compared with Scenario 1, Scenario 2 further includes the

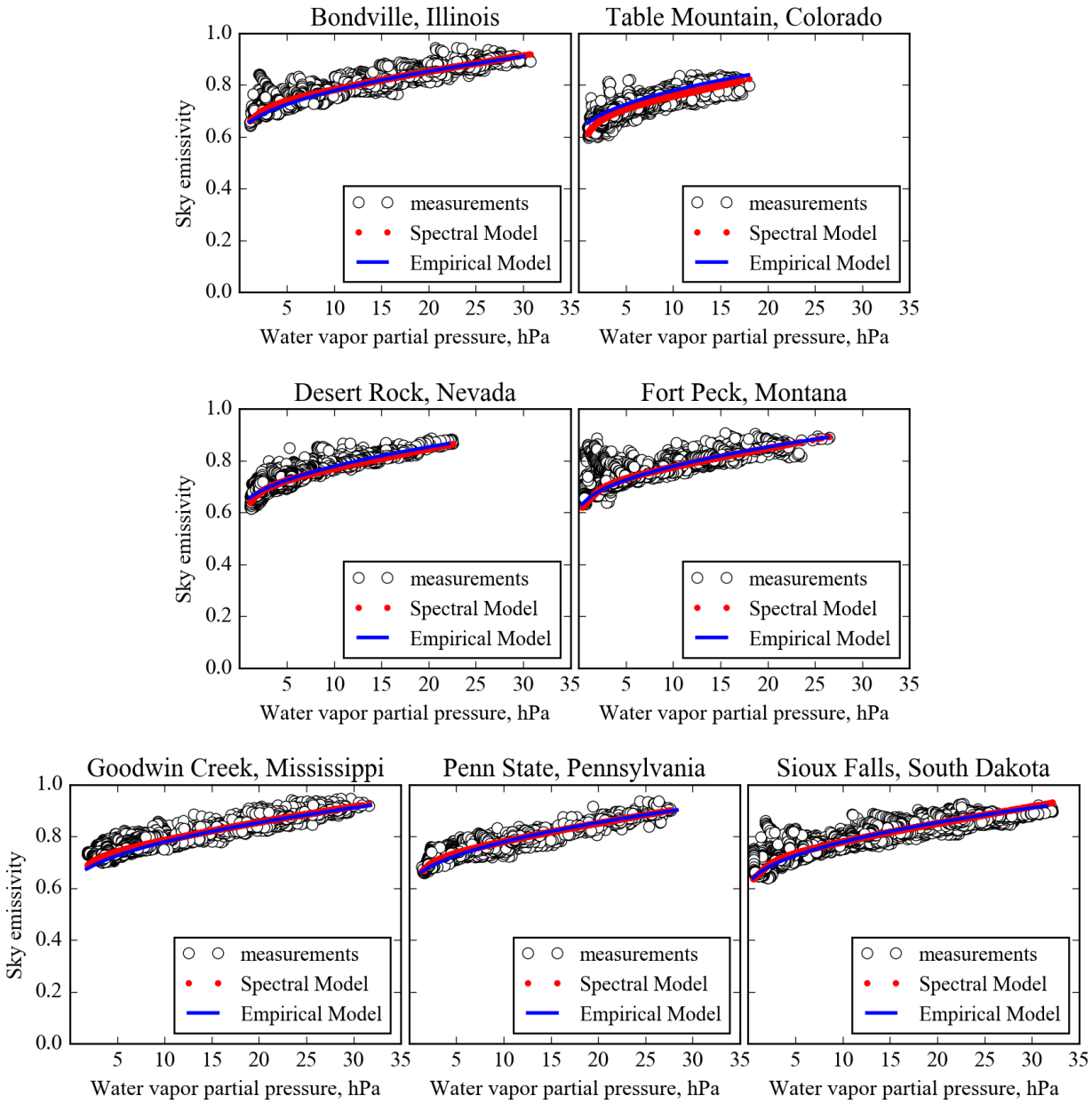

Figure 3.15: Comparison of measured, empirically modeled, and spectrally modeled sky emissivities for the 7 SURFRAD stations.

Table 3.4: Error metrics for empirical and spectral models for estimation of surface DLW during daytime. Bold values indicate best results.

	SURFRAD Stations						
Parameters	Bondville	Table Mountain	Desert Rock	Fort Peck	Goodwin Creek	Penn State	Sioux Falls
Latitude (°)	40.05	40.13	36.62	48.31	34.25	40.72	43.73
Longitude (°)	-88.37	-105.24	-116.02	-105.10	-89.87	-77.93	-96.62
Altitude (m)	213	1689	1007	634	98	376	437
Average T_a (°C)	14.0	14.1	21.9	11.4	18.2	14.6	11.6
25th percentile of T_a (°C)	5.0	7.3	14.6	0.4	11.1	9.4	0.2
75th percentile of T_a (°C)	23.3	21.6	30.1	22.9	26.1	21.1	23.0
Average P_w (hPa)	11.9	7.2	5.1	8.9	14.3	11.1	11.1
25th percentile of P_w (hPa)	5.0	3.4	3.1	4.0	6.4	4.9	4.4
75th percentile of P_w (hPa)	18.0	10.6	5.8	13.7	21.7	16.5	17.0
Empirical MBE (W/m^2)	2.64	-6.82	**3.34**	3.91	4.62	**0.46**	1.30
Empirical RMSE (W/m^2)	7.62	9.70	**6.93**	9.60	8.53	7.34	9.07
Empirical rRMSE (%)	2.47	3.41	**2.18**	3.20	2.54	2.44	2.99
Computed MBE (W/m^2)	**-0.02**	**0.61**	4.52	**3.85**	**1.35**	-1.58	**0.15**
Computed RMSE (W/m^2)	**6.86**	**6.93**	7.65	**9.25**	**6.97**	**6.95**	**8.68**
Computed rRMSE (%)	**2.22**	**2.43**	2.40	**3.08**	**2.08**	**2.31**	**2.86**

scattering by cloud droplets. Scenario 3 adds aerosols where the aerosol profile is adapted from Ref. [60]. Scenario 4 adds the $\sim 13\ \mathrm{W\,m^{-2}}$ extraterrestrial longwave irradiance. Scenario 5 uses the Gamma cloud droplet size distribution presented before, while also keeping the liquid water path (LWP) unchanged. The results of the proposed radiative model are within 3% of the CIRC measurements ($339.0\ \mathrm{W\,m^{-2}}$ and $373.2\ \mathrm{W\,m^{-2}}$ for Case 6 and Case 7, respectively) for all scenarios. Since the measurements have uncertainties of 3% [71], the proposed model produces reliable results that are within the uncertainties of the measurements.

The comparisons of different scenarios are presented in Fig. 3.16 and Fig. 3.17 for Case 6 and Case 7, respectively. The difference between S2 and S1 indicates the contribution of cloud scattering, which reduces the downwelling flux of the cloud layers and the layers below the clouds because part of the longwave radiation is scattered to outer space. The contribution of aerosols is quantified by the difference between S3 and S2, which increases the downwelling flux above the cloud layers while the surface downwelling flux is nearly unchanged. In the cloud layers and the layers below the clouds, the contribution of aerosols is diminished by the presence of clouds. By comparing Figs. 3.17 and 3.16, the aerosol contribution is more distinct when optically thin clouds are present (Case 7). The contribution of longwave irradiance from the Sun increases the downwelling flux above the cloud layers as shown by the difference between

Table 3.5: Comparison of the proposed radiative model with ICRC results as well as different scenarios. Different inputs between scenarios are highlighted in bold fonts.

	CIRC modeled [70]	Scenario 1	Scenario 2	Scenario 3	Scenario 4	Scenario 5
Spectral resolution, cm^{-1}	1	1	1	1	1	1
P, T and gas concentration profiles	CIRC	CIRC	CIRC	CIRC	CIRC	CIRC
Number of modeled gases*	10	**6**	6	6	6	6
$AOD_{497.5}$	0	0	0	**0.10**	0.10	0.10
Longwave from solar irradiance, $W\,m^{-2}$	0	0	0	0	**13.29**	13.29
Effective radius of cloud droplets, μm	CIRC	CIRC	CIRC	CIRC	CIRC	**10.00**
Effective variance of cloud droplet radius	0.014	0.014	0.014	0.014	0.014	**0.100**
Spectral dispersion of cloud droplet radius	0.12	0.12	0.12	0.12	0.12	**0.35**
Liquid water path, $g\,cm^{-2}$	CIRC	CIRC	CIRC	CIRC	CIRC	CIRC
Scattering of LW by clouds and aerosols	none	none	**included**	included	included	included
Case 6						
Number of layers	69	69	69	69	69	69
Ground altitude, m	320	320	320	320	320	320
Cloud thickness, m	1600	1600	1600	1600	1600	1600
$COD_{497.5}$	61.66	61.66	61.66	61.66	61.66	**41.17**
Surface downwelling flux, $W\,m^{-2}$	335.20	334.39	329.47	329.51	329.51	331.60
Relative error to measured 339.0 $W\,m^{-2}$, %	-1.12	-1.36	-2.81	-2.80	-2.80	-2.18
Case 7						
Number of layers	59	59	59	59	59	59
Ground altitude, m	2.4	2.4	2.4	2.4	2.4	2.4
Cloud thickness, m	120	120	120	120	120	120
$COD_{497.5}$	6.96	6.96	6.96	6.96	6.96	**6.11**
Surface downwelling flux , $W\,m^{-2}$	372.60	373.87	370.42	370.50	370.63	370.95
Relative error to measured 373.2 $W\,m^{-2}$, %	-0.16	0.18	-0.74	-0.72	-0.69	-0.60

Notes*: CIRC models 10 atmospheric gases: H_2O, CO_2, O_3, N_2O, CH_4, O_2, CO, CCL4, CFC11 and CFC12. The proposed radiative model in this work includes the first six gases.

S4 and S3. The downwelling flux remains nearly unchanged in or below the cloud layers since the clouds 'shield' the longwave radiation from the layers above, so that layers below the clouds 'see' only the clouds. The difference between S5 and S4 shows the contribution of cloud droplet size distribution. The proposed size distribution has ~ 30% lower COD when compared with the one used in CIRC (see Table 3.5), which increases the downwelling flux in and below the cloud layers. The difference is more distinct for optically thick clouds (Case 6) when comparing Figs. 3.16 and 3.17. The spectral differences between scenarios show up only in the atmospheric windowing bands (400 ~ 650 cm^{-1} and 750 ~ 1400 cm^{-1}). The surface downwelling flux for the five scenarios are presented in Table 3.5, where the differences between scenarios are smaller than 5 $W\,m^{-2}$, indicating that the surface downwelling flux is insensitive to the cloud scattering, aerosols, extraterrestrial longwave radiation and cloud droplet size distributions under cloudy skies.

3.6 Conclusions

The primary goal of this Chapter is to develop an effective *minimal* model that incorporates the main physical mechanisms needed for calculation of the atmospheric downwelling longwave radiation at the ground level for widely different geographical sites. The operative word *effective* here means a complete model that is capable of discerning the effects of the main contributors to DLW while allowing for fast computations that can be performed by mini computers within time frames compatible with both the time scale of variations in the atmosphere, but also with time scales of engineering systems (power plants, etc.). All main features of the model and its implementation are described within the body of this work.

A secondary goal is to examine the effects of water vapor, carbon dioxide and aerosols content on the surface DLW at high spectral resolutions. A spectrally resolved, multi-layer radiative model is developed to calculate surface downwelling longwave (DLW) irradiance (0 ~ 2500 cm^{-1}) under clear-sky (cloud-free) conditions. The wavenumber spectral resolution of the model is 0.01 cm^{-1} and the atmosphere is represented by 18 non-uniform plane-parallel layers with the pressure of each layer determined by a constant σ coordinate system. Standard AFGL profiles for temperature and atmospheric gas concentrations have been adopted with the correction for current surface atmospheric gas concentrations. The model incorporates the most up-to-date (2016) HITRAN molecular spectral data for 7 atmospheric gases: H_2O, CO_2, O_3, CH_4, N_2O, O_2 and N_2. The MT_CKD model is used to calculate water vapor and CO_2 continuum absorption coefficients.

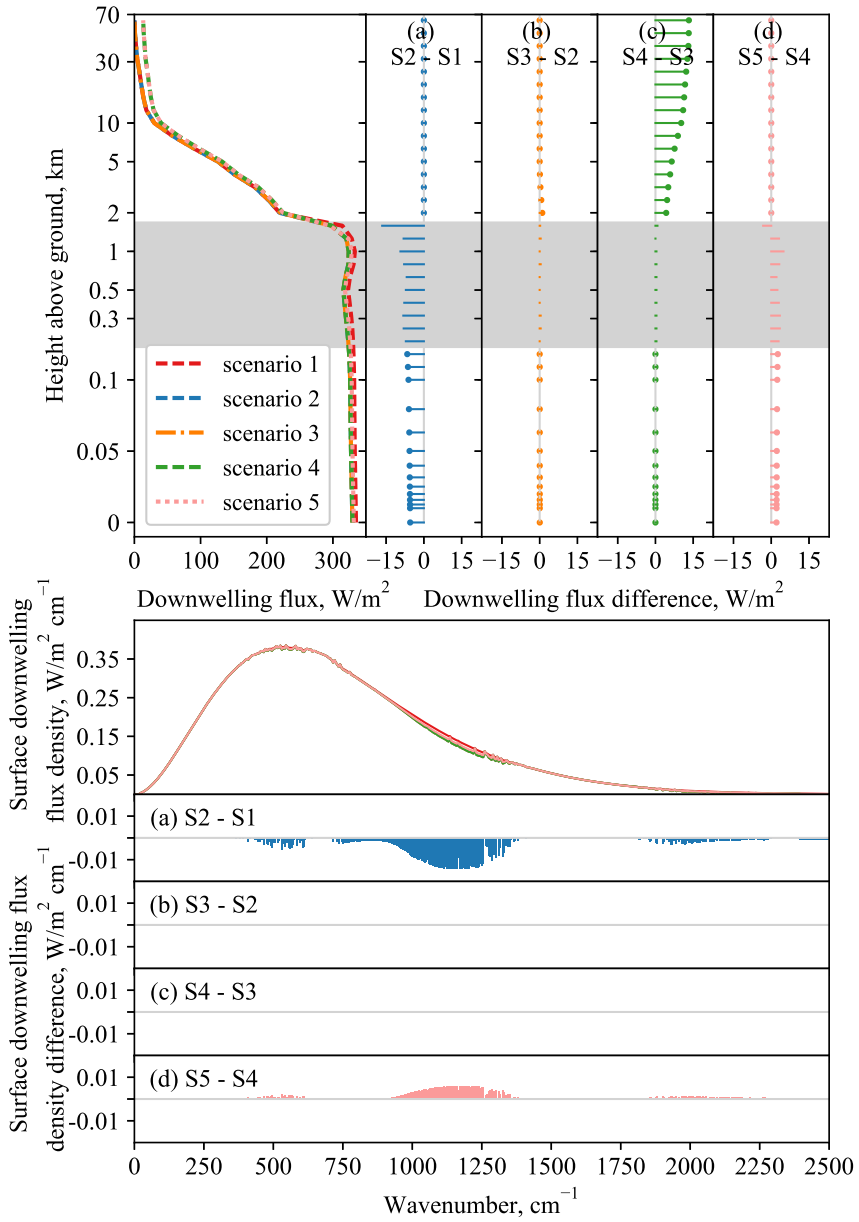

Figure 3.16: Comparison of downwelling flux profiles and surface downwelling flux densities between different scenarios for Case 6. Gray areas indicate cloud layers. Columns (a), (b), (c), (d) show the difference between Scenarios 2 and 1, 3 and 2, 4 and 3, 5 and 4, respectively.

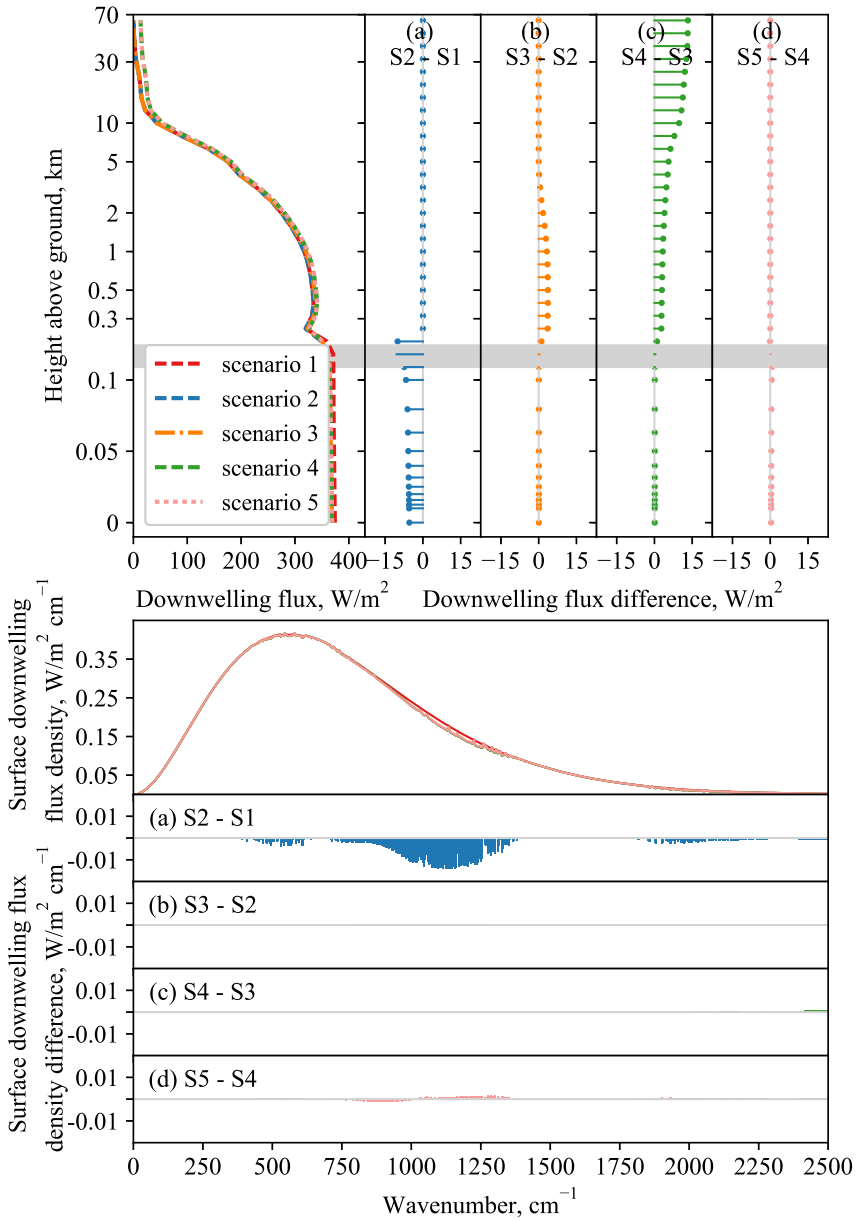

Figure 3.17: The same as Fig.3.16 but for Case 7.

For a scattering atmosphere (with aerosols), the aerosol size distribution is assumed to follow a bimodal distribution. The size and refractive index of aerosols change as they absorb water, therefore the size distribution and refractive index are corrected for different values of local water vapor concentrations (relative humidity values). The absorption coefficients, scattering coefficients and asymmetry factors for aerosols are calculated from the refractive indices for different size distributions by Mie theory. The radiosity and irradiance of each layer are calculated by energy balance equations using transfer factors with the assumption of isotropic aerosol scattering (the δ-M approximation is used to scale anisotropic scattering). The monochromatic downwelling and upwelling fluxes with scattering for each layer are further calculated using a recursive plating algorithm. Broadband fluxes are integrated over the spectrum for both non-scattering and scattering atmospheres.

A model with 18 vertical layers is found to achieve grid independence for DLW. For a non-scattering atmosphere (aerosol free), the calculated surface DLW irradiance agrees within 2.91% with the mean values from InterComparison of Radiation Codes in Climate Models (ICRCCM) program, and the spectral density difference is smaller than 0.035 W cm m^{-2}. For a scattering atmosphere, the modeled DLW irradiance agrees within 3.08% relative error when compared to measured values from 7 climatologically diverse SURFRAD stations. This relative error is smaller than the error from a calibrated empirical model regressed from aggregate data for those same 7 stations, i.e., the proposed model captures the climatological differences between stations. We also note that these deviation values are within the uncertainty range (+/- 5 W m^{-2}) of pyrgeometers ($\sim$ 3% uncertainty).

In summary, the proposed model is capable of capturing climatological and meteorological differences between locations when compared to extensive surface telemetry, which justifies its use for calculating DLW at other locations across the contiguous United States where measurements are not readily available. The proposed model also serves as a powerful and robust tool to study high spectral resolution interactions between atmospheric constituents within the critical longwave region of the electromagnetic spectrum.

3.7 Acknowledgments

Most part of this Chapter, is a combination of three publications: M. Li, Z. Liao, and C. F. M. Coimbra (2018) “Spectral model for clear sky atmospheric longwave radiation” *Journal of Quantitative Spectroscopy*

and Radiative Transfer, 209, 196-211; M. Li, Z. Liao and C. F. M. Coimbra (2018) "An Efficient Spectral Model for Evaluating Spectral and Spatial Distributions of Clear Sky Atmospheric Longwave Radiation," accepted for the *16th International Heat Transfer Conference (IHTC-16)*. The dissertation author is the second author of these manuscripts.

Chapter 4

Anisotropic Corrections for the Downwelling Radiative Heat Transfer Flux from Various Types of Aerosols

4.1 Introduction

The accurate determination of downwelling longwave (DLW) radiation, also referred as sky or atmospheric radiosity, is critically important to many engineering, meteorological and agricultural applications. These applications include the balance of heat and mass fluxes for cooling towers and power plants, the calculation of surface evaporative fluxes from vegetation and outdoor equipment, and many other engineering applications, both in urban and natural settings [72, 73]. Related concepts, such as the 'effective sky temperature' or the 'effective sky emissivity' also provide physical insight on the operation of meteorological and radiometric instruments, as well as on the performance of passive cooling devices [74, 75].

Atmospheric downwelling radiation within the range of 4 - 100 μm can be measured directly by infrared pyrgeometers, which are more expensive and more difficult to calibrate due to ground interference than the pyranometers commonly used for shortwave radiation [72, 76]. Therefore, widespread experimental determination of DLW is often hindered by both capital and maintenance costs associated with infrared telemetry. Also, well-maintained pyrgeometers are only found in a small fraction of existing meteorological

stations, and therefore real-time values of sky radiosity are not available with sufficient spatial resolution to be useful for thermal management of industrial equipment. Remote sensing offers an alternative for indirect calculation of atmospheric radiosity, but again, the relatively low temporal and spatial resolutions currently available are limiting for practical purposes and real-time applications [77].

Theoretical determination of DLW for cloudless (clear) skies is possible by a combination of atmospheric temperature and concentration profiles, high resolution absorption data for the main gas constituents of the atmosphere, and radiative transfer models that incorporate these high spectral resolution data sets into line-by-line calculations [4]. Radiative transfer in diffuse (isotropic) media can be modeled accurately using a two-flux approach to minimize computational resources because the absorption, emission and scattering of longwave radiation by gases in the atmosphere can be closely modeled as diffuse [4]. However, the scattering of longwave radiation by real aerosols can diverge substantially from isotropic behavior.

It is well-known that the Monte Carlo method offers a relatively simple way to model the radiative transfer problem in the atmosphere with high levels of physical realism, including complex effects of anisotropy and polarization. Here we use an anisotropic Mie scattering formulation to model the contributions to DLW caused by aerosols, and compare those solutions to the line-by-line results obtained by the isotropic scattering assumption. This comparison allows us to develop corrective scaling rules for the fluxes that is applicable to different aerosol types and a wider range of aerosol loading values.

When anisotropic effects are taken into account, scaling methods are employed to scale the anisotropic effects into an isotropic scattering formulation [78]. Most of the scaling methods previously proposed are based on the transformation of optical depth and the phase function [79]. The works by Joseph et al. [80] and Potter [81] used $\delta - M$distribution approximations for the forward peaks of the aerosol scattering phase functions. Wiscombe extended the $\delta - M$ distribution approximation to develop what is now called the $\delta - M$ approximation [82]. Lee and Buckius further developed several scaling methods for P1 approximations and two-flux methods [78]. Some of these scaling techniques were compared with exact solutions [78, 83], or with Monte Carlo (MC) simulations [84, 85], and were validated for specific conditions. Lee and Buckius compared the heat flux simulated with $a_1/3$ scaling (derived from P1 scaling) and with 2f-1 scaling with exact solutions to obtain fairly accurate results [78]. Guo and Maruyama [83] conducted similar comparisons between the results simulated from scaling techniques based on $\delta - M$ distribution approximations versus results obtained with anisotropic scattering computations. For more complex anisotropic scattering problems,

integrated P-1 and MC simulations are compared to pure MC simulations, and the former is (not surprisingly) found to be faster but less accurate [84].

Although the studies above have exploited the validity of various scaling techniques, those calculations were conducted for relatively low aerosol loading (e.g. low aerosol concentrations). Moreover, the spectral variability and the sensitivity to asymmetry factors for different aerosol types were not considered in previous studies. The present study employs complete Monte Carlo simulations to analyze the validity of the δ-M approximation for all practical values of aerosol optical depths (AODs). We also propose corrections to the δ-M approximation when large deviations are observed for high AOD values.

4.2 Overview of the Longwave Radiative Model

4.2.1 A Model Atmosphere

The cloud-free atmosphere is modeled by 18 plane-parallel layers as shown in Fig. 4.1. The pressure of each layer is determined by a constant σ coordinate system as proposed in [4, 86]. The AFGL mid-latitude summer profile is used for temperature and pressure profiles as well as for the vertical profiles of seven participating atmospheric gases: water vapor, carbon dioxide, ozone, methane, nitrous oxide, oxygen and nitrogen [87]. The vertical profiles of gases are corrected by their current surface concentrations [4]. The layer averaged temperature and constituent concentrations are averaged using pressure values as the weights [4, 86]. The altitude of layer boundary and average temperature in each layer is shown in Fig. 4.1. The gaseous absorption coefficients are calculated using the most up-to-date HITRAN molecular spectral data for these seven gases [88]. All gases are assumed to be purely absorbing in the longwave spectrum without any scattering effects [89]. The vertical aerosol optical depth profile is adopted from [90] using the Cloud Aerosol LIDAR and Infrared Pathfinder Satellite Observations (CALIPSO) over North America.

4.2.2 The Optical Properties of Aerosols

The absorption, scattering coefficients and asymmetry factor of aerosols are calculated using Mie theory from the size distribution and refractive index of aerosol particles [91], which are dependent on their physical and chemical compositions. Common aerosol components include water-soluble salts, soots, dusts and water droplets. The composition of aerosols varies from region to region with each component

(a)

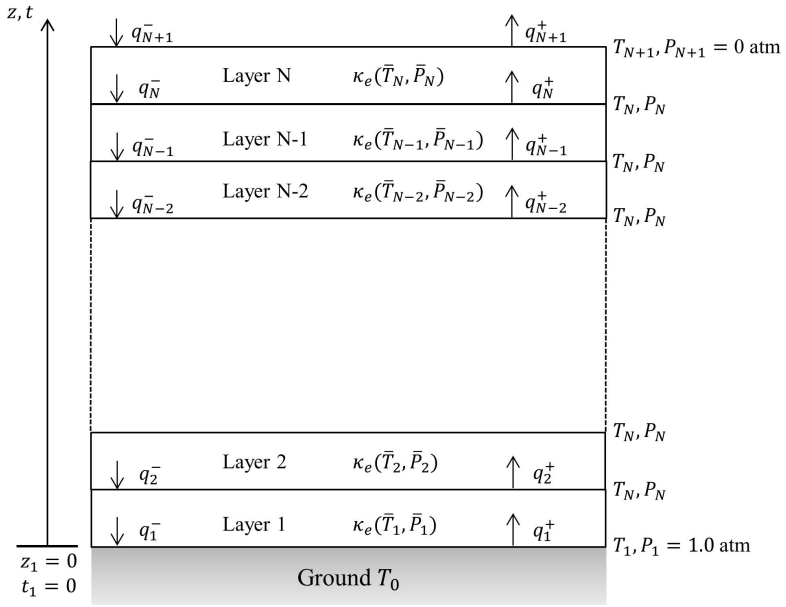

(b)

N	Upper boundary z_N(m)	Average T_N(K)
18	120,000	274.9
17	32,700	230.1
16	23,500	220.1
15	18,500	216.5
14	15,100	217.2
13	12,600	225.6
12	10,500	238.3
11	8,640	249.3
10	7,050	258.8
9	5,700	266.7
8	4,490	273.4
7	3,450	279.2
6	2,550	284.0
5	1,790	287.6
4	1,160	290.1
3	664	292.0
2	300	293.4
1	68	294.0
Ground	0	294.2

Figure 4.1: (a) Schematic representation of the multilayer model of the Earth-atmosphere system with a total of N atmosphere layers. Altitude and optical depth are labeled as z and t, respectively; (b) Altitude of layer boundaries and layer-averaged temperatures.

Table 4.1: The volume fraction (%) of the four basic components for three aerosol types (the numbers inside the brackets are the number fractions (%)).

Aerosol Type	Dust-like (DL)	Water-Soluble (WS)	Oceanic (OC)	Soot (SO)
Maritime		5 (99.96)	95 (0.04)	
Continental	70 (0.02)	29 (93.83)		1 (6.16)
Urban	17 (1.65×10^{-5})	61 (59.25)		22 (40.75)

having typical size distributions and refractive indexes. Finer particles (such as industrial soot) are normally anthropogenic in origin and mostly found in urban areas [92]; marine aerosols are mostly water droplets generated by wave and tide motion; continental aerosols are composed mostly by dust [91]. Four types of aerosols are considered in this work: the internal mixing aerosols from Refs. [4, 6], maritime aerosols, continental aerosols and urban aerosols. The compositions (volume fractions, %) of the latter three aerosol types are presented in Table 4.1 (for dry aerosols). The values inside the brackets are number fractions (%) [91].

In-situ observations have shown that log-normal distribution are appropriate to describe aerosol size distributions [93, 94]. The mixture size distribution is the summation of the distribution functions of each

Table 4.2: Microphysical characteristics of the four basic components in dry conditions [5].

component	Dust-like (DL)	Water-Soluble (WS)	Oceanic (OC)	Soot (SO)
$r_{m,i}$, μm	1.000	0.010	0.600	0.024
σ_i, μm	2.990	2.990	2.510	2.000

Table 4.3: Growth Factors Used to Adjust Particle Size Distributions and Refractive Index [6]

Relative Humidity	30%	40%	50%	60%	70%	80%	90%
Constituent	Growth factor for Relative Humidity						
Dust	1.000	1.000	1.000	1.000	1.000	1.000	1.000
Sulfates	1.140	1.180	1.305	1.350	1.435	1.539	1.746
Sea salt	1.000	1.000	1.573	1.620	1.790	1.965	2.345
Soot	1.000	1.000	1.000	1.016	1.033	1.186	1.407

component. For dry aerosols, the size distribution follows

$$\frac{dn(r)}{dr} = \sum_{i=1}^{I} \frac{N_i}{\sqrt{2\pi} r \ln \sigma_i} \exp\Big[-\frac{1}{2}\Big(\frac{\ln r - \ln r_{m,i}}{\ln \sigma_i} \Big)^2 \Big], \tag{4.1}$$

where $r_{m,i}$ (μm) is the mode radius, σ_i (μm) measures the width of the distribution, and N_i (number/cm^3) is the particle number density of component i. The distribution characteristics of the four basic components are listed in Table 4.2 [5]. Complex refractive indices for the dry components are tabulated in [6].

Ambient relative humidity are found to have an effect on the optical properties of aerosols since the refractive index and size of aerosols are changed if water vapor is being absorbed. To consider the effects of relative humidity, the equivalent complex refractive index for wet aerosols can be estimated using the particle growth factor ϕ_r [95],

$$n = n_0 \phi_r^{-3} + n_w [1 - \phi_r^{-3}] \tag{4.2}$$

$$k = k_0 \phi_r^{-3} + k_w [1 - \phi_r^{-3}] \tag{4.3}$$

where the subscript '0' indicates dry aerosols and the subscript 'w' indicates liquid water. The mode radius for wet aerosols are those for dry aerosols times the growth factor. Growth factors for both refractive indices and radius are listed in Table 4.3. The growth factors for water soluble components and oceanic components in general not available but they can be approximated as sulfates and sea salts respectively in this study [6].

If AOD at 500 nm is specified, with the scale height for the troposphere to be 1575 m [4], the aerosol

extinction coefficient at 500 nm is $\kappa_{e@500\text{nm}} = \text{AOD}/\bar{L}$. Then the particle number density of each component can be inferred from the specified AOD, as described in [4]. Figure 4.2 shows the spectral absorption and scattering coefficients and asymmetry factors for different types of aerosols when AOD is 0.1 and RH is 70%. Marine areosols have the highest asymmetry factor over the entire longwave spectrum, followed by continental aerosols and urban aerosols.

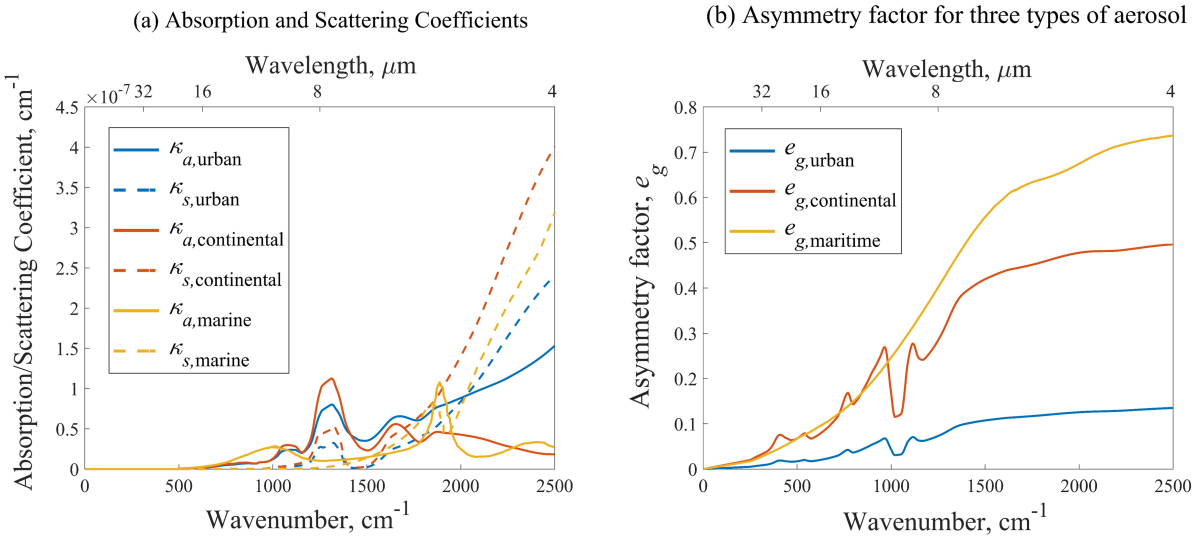

Figure 4.2: Spectral (a) absorption and scattering coefficients and (b) asymmetry factors of urban, continental and marine aerosols when AOD = 0.1 and RH = 70%.

The scattering diagrams presented in Fig. 4.3 illustrate how the incident radiation is scattered for various asymmetry factors. When the asymmetry factor is positive, forward scattering is favored and when the asymmetry factor is negative, backward scattering is more likely to occur.

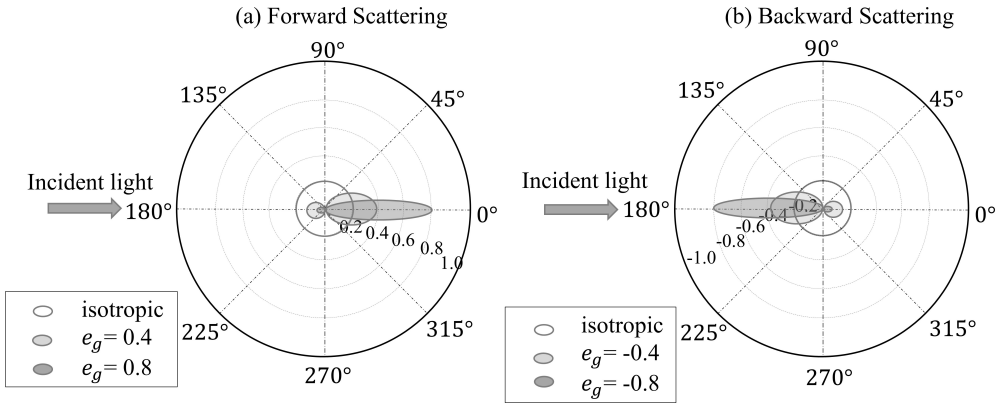

Figure 4.3: Scatter diagram of scattering phase functions for forward and backward scattering with various asymmetry factors.

4.2.3 Input Scaling by δ-M Approximation

One approach to correct the anisotropic scattering effect is to scale the input optical properties to an isotropic scattering medium. Several approximation methods are available. Among them, the δ-M approximation derived by scaling the radiative transfer equation yields the best results when comparing to exact solutions [78]. In this case, the extinction coefficient and single scattering albedo are scaled as,

$$\begin{aligned} \hat{\kappa} &= (1-\tilde{\rho}e_g)\kappa, \\ \hat{\tilde{\rho}} &= \frac{\tilde{\rho}(1-e_g)}{(1-\tilde{\rho}e_g)}, \end{aligned} \tag{4.4}$$

where e_g is the asymmetry factor of the real phase function. After scaling, the phase function is replaced by $P(\cos\Theta) = 1$ and the extinction coefficient and single scattering albedo are replaced by $\hat{\kappa}$ and $\hat{\tilde{\rho}}$, respectively. Following this procedure, anisotropic scattering problems can be approximated and treated as isotropic scattering problems.

Different from scaling the input parameters, another approach is to scale the net result. Scaling rules for this approach will be derived in section 4.4.

4.3 The Monte Carlo Method

Monte Carlo (MC) methods offer statistical means for studying stochastic physical processes (emission, absorption and scattering of bundles of radiant energy or photons) by a large number of simulations. Here the MC algorithm is used to compute the upwelling and downwelling longwave fluxes across each boundary, with longwave radiation emitted both by the ground and the atmosphere.

4.3.1 Photon Emission

Emitting sources in Monte Carlo Radiative Transfer (MCRT) simulation can be divided into two classes: directional point source or diffuse emission, where the latter is the case of longwave emission in the atmosphere [96]. The energy contained in each diffusely emitted photon bundle depends on the total emissive power E_{bs} for a surface or E_{bg} for a gas layer, as well as the number of bundles N [23],

$$E_{bs} = \varepsilon\sigma T_s^4, \tag{4.5}$$

$$E_{bg} = 4\kappa_a \Delta z \int_{\Delta\nu} I_{b\nu}(T_g) d\nu, \tag{4.6}$$

where

$$I_{b\nu}(T_g) = \frac{2hc^2\nu^3}{e^{hc\nu/(k_B T_g)} - 1}, \tag{4.7}$$

represents the wavenumber ν-based Planck distribution, $\sigma = 5.67 \times 10^{-8}$ W m^{-2} K^{-4} is the Stefan-Boltzmann constant; ε is the surface emittance; κ_a (cm^{-1}) is the absorption coefficient of the gas volume; Δz (m) is the thickness of the atmospheric layer; $h = 6.626 \times 10^{-34}$ J s is Planck's constant and $k_B = 1.38 \times 10^{-23}$ J K^{-1} is the Boltzmann constant.

The location of photon emission is randomly sampled across surfaces and volumes. For a photon bundle emitted from a surface, the zenith angle θ (in the range of 0 to $\pi/2$) and the azimuth angle ϕ are sampled as [25]:

$$\theta = \cos^{-1}(\sqrt{\xi_\theta}), \qquad \phi = 2\pi\xi_\phi. \tag{4.8}$$

For a photon bundle emitted from a volume of gas, the range of its zenith angle is extended to $[0, \pi]$,

$$\theta = \cos^{-1}(2\xi_\theta - 1), \qquad \phi = 2\pi\xi_\phi, \tag{4.9}$$

where ξ_ϕ and ξ_θ are random numbers uniformly sampled from 0 to 1.

4.3.2 Collision-Based Monte Carlo Approach

The Monte Carlo simulation procedure for forward collision-based approach is illustrated in Fig. 4.4. An emitted photon bundle is assumed to travel undisturbed until it collides with a molecule or a particle, where it is either absorbed or scattered.

The probability that a photon bundle travels an optical depth τ without collision is:

$$p(\tau)d\tau = e^{-\tau}d\tau. \tag{4.10}$$

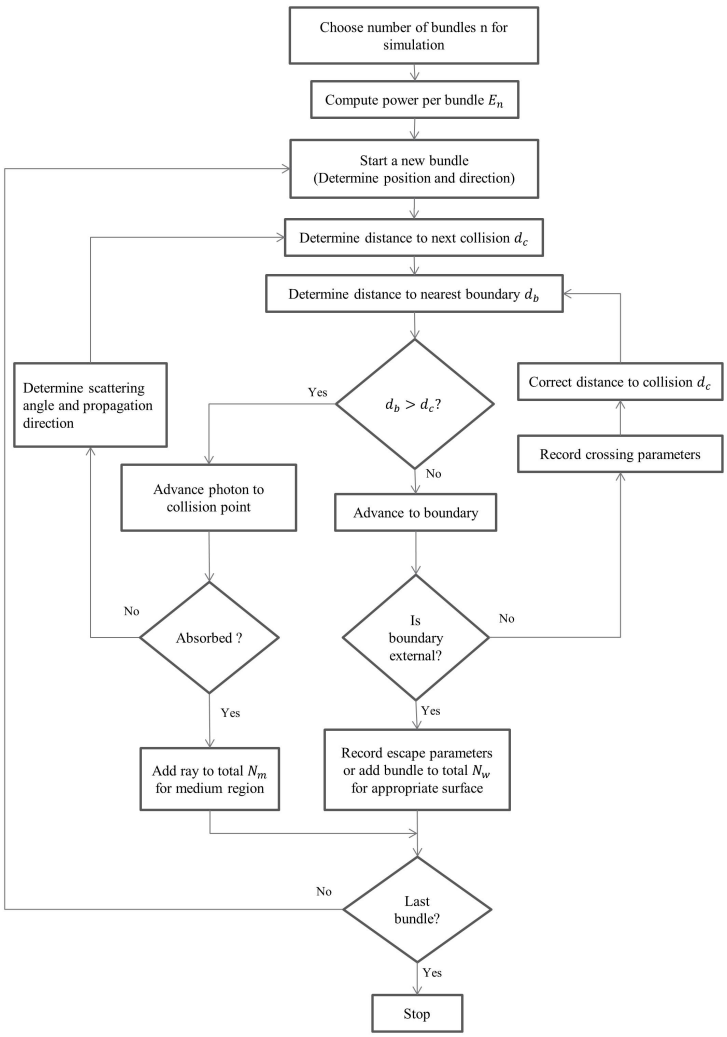

Figure 4.4: Flow chart of Monte Carlo simulation procedure for forward collision-based approach.

Then the traveled optical depth before next collision is sampled as [21, 26]

$$\begin{aligned} \xi_\tau &= \int_0^{\tau_0} e^{-\tau} d\tau = 1 - e^{-\tau_0}, \\ \tau_0 &= -\ln(1-\xi_\tau) = -\ln \xi_\tau. \end{aligned} \tag{4.11}$$

The physical distance traveled between consecutive collisions is then

$$d_c = \frac{\tau_0}{\kappa_\nu} = -\frac{\ln \xi_\tau}{\kappa_e}, \tag{4.12}$$

where ξ_τ is the sampled random number, κ_e (cm^{-1}) is the extinction coefficient of current medium.

After determining d_c, the distance to the nearest boundary d_b (m) along the direction of propagation is calculated. Then d_b and d_c are compared to determine whether the collision occurs in the current layer, or after crossing the boundary. If $d_c < d_b$, the collision occurs in the current layer and the photon may either be absorbed or scattered. The probability of scattering is determined by the single scattering albedo of the medium. If absorbed, the energy of the photon bundle is converted to the thermal field of the media. If scattering occurs, the bundle is traveling in a new direction determined by the scattering angle, which is sampled by inverting the Henyey-Greenstein scattering phase function [97],

$$\begin{aligned} P_{\mathrm{HG}}(\cos\Theta, e_g) &= \frac{1-e_g^2}{2[1+e_g^2-2e_g(\cos\Theta)]^{3/2}}, \\ \cos\Theta &= \frac{1}{2e_g}\left\{1+e_g^2-\left[\frac{1-e_g^2}{1-e_g+2e_g\xi_\Theta}\right]^2\right\}, \\ \Phi &= 2\pi\xi_\Phi. \end{aligned} \tag{4.13}$$

Then, a new scattering direction (r_x', r_y', r_z') is generated according to the incoming ray direction (r_x, r_y, r_z) and the scattering angles [98]

$$\begin{aligned} r_x' &= r_x\cos\Theta - \frac{\sin\Theta}{\sqrt{1-r_z^2}}(r_x r_z\cos\Phi + r_y\sin\Phi), \\ r_y' &= r_y\cos\Theta - \frac{\sin\Theta}{\sqrt{1-r_z^2}}(r_y r_z\cos\Phi - r_x\sin\Phi), \\ r_z' &= r_z\cos\Theta + \sqrt{1-r_z^2}\sin\Theta\cos\Phi. \end{aligned} \tag{4.14}$$

If $d_c > d_b$, the photon is advanced to the boundary and its coordinates are updated accordingly,

$$x' = x + r_x d_b, \qquad y' = y + r_y d_b, \qquad z' = z + r_z d_b. \tag{4.15}$$

If the boundary is an external boundary, the energy contained in this photon bundle is recorded as an outgoing energy flux or energy absorbed by a surface. If the external surface is non-black, the possible reflection should also be considered. If an internal boundary is crossed, energy flux to the next layer is recorded. Moreover, d_c and d_b are also updated according to the optical properties in the new layer. The remaining distance to collision is then

$$d_c' = \frac{\kappa_\nu}{\kappa_\nu'}(d_c - d_b), \tag{4.16}$$

where κ_ν' (cm^{-1}) is the extinction coefficient in the just-entered layer. The updated distance to collision d_c' and distance from the updated position to next boundary d_b' are compared. This process continues until the bundle is absorbed or exits the external boundaries [27].

4.3.3 Computational performance

The Multi-Spectral Energy Bundle (MSB) method is used to reduce the computational cost associated with the line-by-line Monte Carlo simulations [99]. The MSB method treats the energy bundles as multi-spectral rays composed of a set of sub-bundles in order to make the spectral integration more efficient. Unlike the energy emitted by each monochromatic bundle represented by Eqs. (4.5) and (4.6), the averaged energy of a photon bundle is

$$E_{bg} = \int_V \int_{4\pi} \int_0^\infty \kappa_\nu I_{b\nu} d\nu d\Omega dV = 4\pi V \int_0^\infty \kappa_\nu I_{b\nu} d\nu, \tag{4.17}$$

where κ_ν (cm^{-1}) is the spectral absorption coefficient, ν (cm^{-1}) is the wavenumber and $I_{b\nu}$ ($\mathrm{W\,m^{-2}}$) is the blackbody spectral intensity given by the Planck distribution. In the MSB approach, the bundles are composed by a set of sub-bundles, each carrying a certain amount of energy and having a specific wavenumber. The energy of the multi-spectral bundle will be the summation of the energy of its sub-bundles [99]. The longwave spectral range (0 to 2500 cm^{-1}) with a resolution of 0.01 cm^{-1} is uniformly divided into N_b sub-bands with respect to wavenumber, each with a specific Planck-mean absorption, scattering coefficients and single

scattering albedo

$$y_p = \frac{\int_{\Delta\nu} y I_{b\nu}(T) d\nu}{\int_{\Delta\nu} I_{b\nu}(T) d\nu}, \tag{4.18}$$

where y is a general notation representing absorption, scattering coefficients and single scattering albedo and y_p is the Planck-mean value in the sub-bands. The number of sub-bands N_b is found from a grid dependence test where less than 5% change is observed when using 2500 sub-bands or more.

Monte Carlo simulations are based on random sampling procedures so any practical results will have a non-zero variance associate with it. One measure of performance is to compute the variance of multiple runs, which can always be reduced by increasing the number of samples, but at the penalty of increasing computational time. Variance reduction techniques are used to improve performance while significantly reducing the required number of samples [98].

Biasing is a common technique for variance reduction. When source particles are sampled over space, energy, angle or time, some source particles may be more likely to contribute to a particular quantity of interest than others [100]. Traditional source biasing techniques enable the simulation of more source particles with reduced weights from more important regions [101]. In our case, the radiative transfer in some spectral bands (infrared atmospheric windows 800 cm^{-1} to 1200 cm^{-1}, 2000 cm^{-1} to 2300 cm^{-1} and 2400 cm^{-1} to 2500 cm^{-1}) are more sensitive to optical properties of aerosols, so the contribution of anisotropic scattering effect is larger than that in other bands. The technique adopted here starts by choosing the modified (biased) probability distribution for bands in terms of their contribution to DLW radiative flux and anisotropic scattering effect, and then correcting the corresponding weight of each source particle by $w_{\text{biased}} \cdot p(x)_{\text{biased}} = w_{\text{unbiased}} \cdot p(x)_{\text{unbiased}}$, where w represents the weight while $p(x)$ is the probability distribution of the physical process being sampled. The sum of probability $p(x)$ is $\int p(x)_{\text{biased}}\, dx = \int p(x)_{\text{unbiased}}\, dx = 1$. Note that the total weight of source particles is also conserved. In our case, the unbiased value $p(x)$ is constant for all bands with same particle weight while biased probability distribution increases the number of bundle samples in atmospheric windows and decreases the weight of each bundle.

This variance reduction method successfully reduces computation time in the bands that do not contribute significantly to anisotropic scattering effects, and provides substantial improvements to the computational efficiency of the Monte Carlo simulations.

4.4 Net Result Based Scaling Rules

4.4.1 Model Validation

Spectral comparisons of surface DLW flux densities between the Monte Carlo simulation and two-flux modeling results are shown in Fig. 4.5. Model results for verification are compared with the results from the Atmospheric and Environmental Research (AER) report for Case 27 (aerosol-free) in the Intercomparison of Radiation Codes in Climate Model (ICRCCM) program [102]. Despite of fluctuations caused by statistical nature of Monte Carlo method, the overall shape of the Monte Carlo simulation matches well with the modeled profile. The absolute difference is smaller than 0.05 W cm m^{-2} for all wavenumbers.

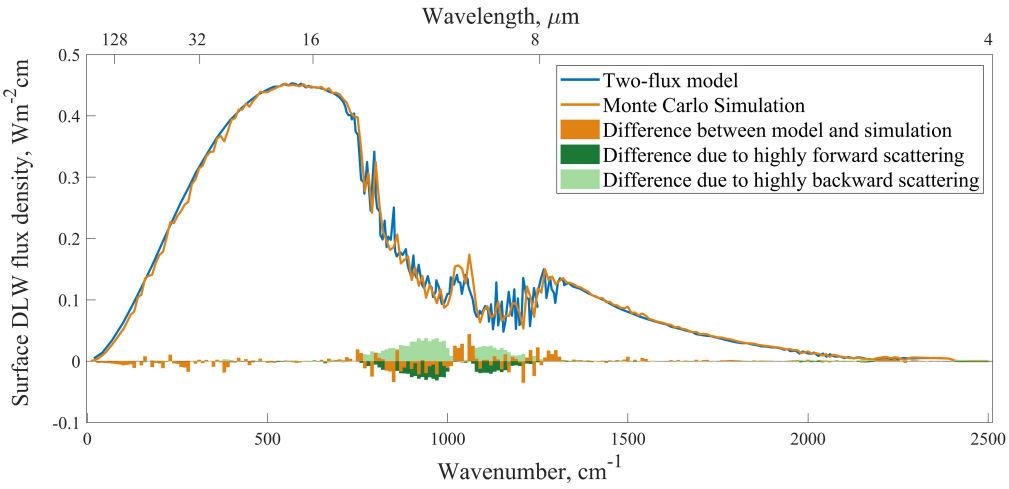

Figure 4.5: Comparison of spectral surface DLW flux densities between Monte Carlo simulation (centrally averaged) and the results obtained from a two-flux model in [4].The differences of flux density due to anisotropic effects are also presented.

4.4.2 The Effect of Anisotropic Scattering

Figure 4.5 also presents the difference of spectral DLW flux density between a highly forward backward scattering atmosphere and an isotropic scattering atmosphere with dark-green bars and light-green bars, respectively. The spectral band between 750 cm^{-1} and 1400 cm^{-1} with high albedo and high Planck's emission are affected the most by the anisotropic scattering. Bands above 2000 cm^{-1} have large albedo but small Planck's emission, therefore their contributions are smaller.

As expected, when backward scattering is dominant ($e_g = -0.9$), the downwelling radiation flux is higher than the flux for isotropic medium, while when forward scattering is dominant ($e_g = 0.9$), the

anisotropic flux is lower. This can be explained by the decrease of temperature and absorption coefficients with respect to altitude. For a backward scattering dominant medium, the DLW that is back-scattered from upwelling radiation emitted from lower layers would exceed the upward longwave radiation that is back-scattered from downwelling radiation emitted from upper layers, resulting an enhancement of downwelling flux. And the DLW is weakened by the forward scattering dominant medium in the similar way. For the considered model atmosphere with prescribed profiles [4], the broadband contribution of DLW from backward scattering is about 0.620 W m^{-2} and broadband forward scattering contribution is about -0.733 W m^{-2}.

4.4.3 The Exponential Relationship between the Correction Factor and the Aerosol Loading Values

The radiative transfer equation (RTE) that describes the photon propagation through the participating atmosphere is [18]:

$$\mu \frac{\partial I(\kappa,\mu)}{\partial \tau} + I(\kappa,\mu) = (1-\tilde{\rho}) I_b(T) + \frac{\tilde{\rho}}{2} \int_{-1}^{1} P(\mu,\mu') I(\kappa,\mu') d\mu', \tag{4.19}$$

where $\mu = \cos\theta$ represents the zenith direction of the radiation ray (azimuthal symmetry is assumed); κ (cm^{-1}) is the extinction coefficient as the sum of of absorption and scattering coefficients; $I(\kappa,\mu)$ and $I_b(T)$ (W m^{-2}) are the radiant intensity in the medium and blackbody radiant intensity, respectively; τ is the optical depth; $\tilde{\rho}$ is the single scattering albedo; T (K) is the temperature of the medium; μ' represents the scattered direction and $P(\mu,\mu')$ is the scattering phase function [78].

By introducing a source function j_ν to represents photon emission and scattering, the radiative transfer Eq. (4.19) can be written in a simplified form

$$\frac{dI_\nu}{ds} = -\kappa_{e,\nu} I_\nu + j_\nu, \tag{4.20}$$

where I_ν (W m^{-2} sr^{-1}) is the spectral intensity, $\kappa_{e,\nu} = \kappa_{a,\nu} + \kappa_{s,\nu}$ (cm^{-1}) is the extinction coefficient, s (m) is the path length.

The anisotropic effect shall be a function of single scattering albedo $\tilde{\rho}$ and asymmetry factor e_g of

aerosols. A normalized optical depth is introduced to quantify $\tilde{\rho}$,

$$\begin{aligned} t^* &= \frac{\kappa_s L}{\kappa_{s0} L}, \\ \tilde{\rho} &= \frac{t^* \kappa_{s0,\mathrm{aer}}}{t^* \kappa_{s0,\mathrm{aer}} + t^* \kappa_{a0,\mathrm{aer}} + \kappa_{a,\mathrm{gas}}}, \end{aligned} \tag{4.21}$$

where L is the thickness of the atmosphere and κ_{s0} is equivalent to AOD equals 0.1 at 500 nm at the surface.

Analogy to Eq. (4.20), the relationship between the anisotropic scattering effect $D(t^*)$ and the normalized optical path t^* for scattering is assumed to satisfy a first order ODE

$$\frac{dD(t^*)}{dt^*} = -\eta D(t^*) + c, \tag{4.22}$$

where $D(t^*) = (q^-_{\mathrm{ani}} - q^-_{\mathrm{iso}})/q^-_{\mathrm{ani}}$ is the anisotropic correction factor that quantifies the anisotropic scattering effect. The solution of the first order ODE is

$$D(t^*) = Ae^{-\eta t^*} + \frac{c}{\eta}, \tag{4.23}$$

With the boundary condition $D(t^* = 0) = 0$, we have $A = -c/\eta$, then,

$$D(t^*) = -\frac{c}{\eta}(e^{-\eta t^*} - 1), \tag{4.24}$$

where coefficients c and η are functions of assymetry factors e_g.

When the concentration of aerosols increases, more radiative cross section overlapping will occurs, then the addition of aerosols would contribute to smaller anisotropic scattering effect, following an exponential behaviour. The exponential behaviour is validated and the values of η and c are evaluated numerically in the following sections.

The anisotropic scattering effect of aerosols increases with increased aerosol concentrations t^*. In some regions of the world, the mean daily values of AOD are often as high as 3.0 (corresponds to $t^* = 30$), while the annual mean over the continent of United States is of the order of 0.1 (corresponds to $t^* = 1$). Table 4.4 shows a few cities and the number of days in 2016 for which t^* exceeded certain values. For these urban areas, there are many days in a year when very high t^* values are recorded. Since evaluation of the anisotropic

scattering effect is especially significant for these conditions, we then ranges t^* from 0 to 30 in the following analysis to cover the possible range of aerosol loadings.

Table 4.4: Number of days in 2016 that t^* exceeded certain values for Beijing (China), Kanpur (India) and Banizoumbou (Niger).

City	$t^* \geq 10$	$t^* \geq 15$	$t^* \geq 20$	$t^* \geq 30$	Number of days in the dataset
Beijing	73	37	18	3	278
Kanpur	81	22	7	1	309
Banizoumbou	68	13	3	2	362

4.4.4 The Scaling Rule for Aerosols with Varying Asymmetry Factors

Figure 4.6 shows the effects of anisotropy $D(t^*, e_g)$ with respect to normalized optical depth t^* and asymmetry factor e_g. The internal mixing aerosol type is used with its spectral asymmetry factor set to vary from -1 to 1. Monte Carlo results obtained from both δ-M scaling and utilization of H-G phase function are presented. The correction factor $D(t^*, e_g)$ increases linearly with increasing asymmetry factor e_g for both backward and forward scattering conditions, as shown in Fig. 4.6 (c). For $t^* < 5$, results from the δ-M approximation and from H-G phase function are identical, indicating that for low aerosol loadings, the δ-M approximation is sufficiently accurate that can be directly used in analytical models such as the two-flux models. For high aerosol loadings, δ-M approximation would underestimate DLW by 0.4% compared to H-G simulations for highly forward scattering cases (corresponds to around 1.2 $\mathrm{W\,m^{-2}}$), then H-G phase function should be used for more precised results. For all cases considered, the anisotropy contributes to less than 2.0% error in surface DLW, as shown in Fig. 4.6 (a) and (b).

Figure 4.6 (d) shows the relationship between $D(t^*, e_g)/e_g$ with respect to t^*, which can be using an exponential function as Eq. (4.24),

$$D(t^*, e_g) = -\frac{e_g A}{\eta}(e^{-\eta t^*} - 1). \tag{4.25}$$

The coefficients A and η are tabulated in Table 4.5 with R^2 values greater than 0.99.

When $t^* > 10$, the correction factor $D(t^*, e_g)/e_g$ becomes notably different for forward and backward scattering cases. Note that the correction factor $D(t^*, e_g)$ is regressed from the Monte Carlo simulations for the model atmosphere considered in this work. If substantially different temperature and constituent profiles are considered (especially aerosol profile), the coefficients for $D(t^*, e_g)$ may differ but the exponential

relationship with respect to t^* and e_g holds, as derived in Section 4.4.3.

Table 4.5: Parameters A, η, and $R^2 2$ in Eq. (4.25) for different asymmetry factor range.

	A	η	R^2
$e_g \geq 0$	0.0179	0.1207	0.9913
$e_g < 0$	0.0169	0.1207	0.9924

4.4.5 The Scaling Rule for Different Types of Aerosols

Figure 4.7 plots $D(t^*)$ with respect to normalized aerosol optical depth t^* for the three aerosol types: Urban, Marine and Continental aerosols, as described in section 4.2.2, when ambient relative humidity is 70%. Monte Carlo simulation results using H-G phase function (star markers and solid lines) and using δ-M approximation (circle markers and dashed lines) are compared. The δ-M approximation deviates from H-G results when $t^* > 5$, overestimates the absolute value of anisotropic effects and its accuracy degrades with increased aerosol concentrations. Since aerosol anisotropic scattering effect is dominant by the aerosol optical properties in the atmospheric window band, continental aerosols with the highest absorption/scattering coefficients have the largest correction factor. Urban aerosols are the least affected by anisotropic scattering because of low values of e_g in the window band. The quantitative relationship between $D(t^*)$ and t^* are using an exponential expression using Eq. (4.24), and the aerosol-type-dependent coefficients c and η are tabulated in Table 4.6. The values of R^2 are greater than 0.99, verifying that $D(t^*)$ is an exponential function of t^* even when the types of aerosols are significantly different.

Table 4.6: Values of coefficients of c and η for different aerosol types. The R^2 for exponential fitting are also listed.

	H-G phase function			δ-M approximation		
	c	η	R^2	c	η	R^2
Urban aerosol	3.8×10^{-4}	0.05241	0.9916	4.7×10^{-4}	0.05811	0.9904
Marine aerosol	7.8×10^{-4}	0.05743	0.9911	8.8×10^{-4}	0.06204	0.9914
Continental aerosol	1.24×10^{-3}	0.06515	0.9978	1.32×10^{-3}	0.06374	0.9972

Since the optical properties of aerosols depend on the ambient relative humidity (refer to section 4.2.2), here the sensitivity analysis of the correction factors to ambient relative humidity is performed. Not only the size distribution and refractive index of aerosols are functions of ambient relative humidity [6], but also the absorption coefficients of atmospheric layers are functions of relative humidity because water vapor

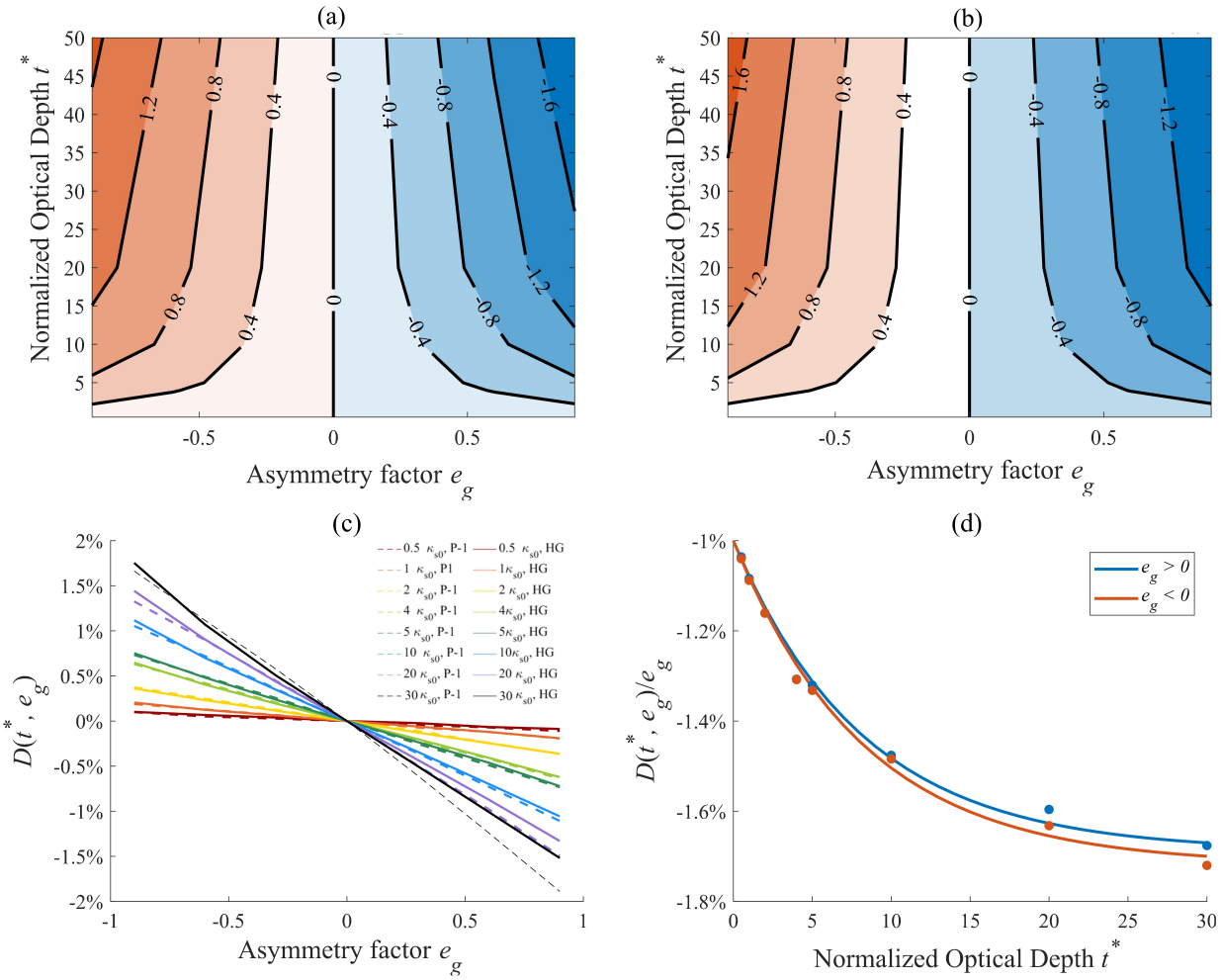

Figure 4.6: Anisotropic correction factor $D(t^*, e_g)$ (%) with respect to normalized aerosol optical depth t^* and asymmetry factor e_g for (a) MC δ-M approximation and (b) MC H-G simulations. (c) Correction factor is a linear function of asymmetry factor. (d) $D(t^*, e_g)/e_g$ is an exponential function of t^* for both forward and backward scattering conditions.

is the main participator.

Figure 4.8 shows the anisotropic correction factor $D(t^*)$ with respect to ambient relative humidity for very high aerosol loadings ($t^* = 30$) under three scenarios. Scenario (a) shows the effects of varying absorption coefficients of the atmospheric layers due to varying water vapor content, assuming that aerosol optical properties are unchanged (optical properties of aerosol at 70% relative humidity is used). The negative correction factors increase with increasing values of relative humidity, because the aerosol forcing is less significant when more water vapor is present. Scenario (b) shows the effects of varying aerosol optical properties due to varying relative humidity, assuming that the absorption coefficients of the atmospheric

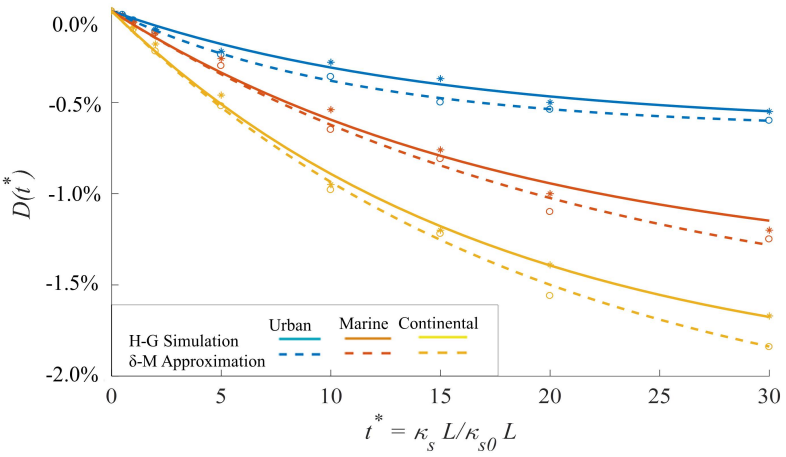

Figure 4.7: Anisotropic correction factor with respected to normalized aerosol optical depth when RH = 70% for three types of aerosols. Symbols represent Monte Carlo simulation results while lines represent exponential fitting functions. Results obtained by using H-G phase functions and using δ-M approximation are plotted for comparison.

layers are unchanged ($\kappa_{a,\text{gas}}$ at 70% relative humidity is used). The negative correction factors decrease with increasing values of relative humidity, because wet aerosols with larger growth factors contribute more to the radiative forcing and have stronger anisotropic effects. Scenario (c) shows the combined effects of scenarios (a) and (b), where the two opposite effects cancel, leaving the correction factor not sensitive to the relative humidity, even for the considered high aerosol loadings ($t^* = 30$).

4.5 Conclusions

A comprehensive Monte Carlo model is used to evaluate quantitatively the accuracy of the isotropic scattering assumption in calculating surface downwelling longwave irradiance (DLW) during clear skies.

The atmosphere is modeled as an 18-layer, plane parallel system with standard temperature and concentration profiles. The absorption, scattering coefficients and asymmetry factors of aerosols are modeled using Mie theory equations, and aerosol scattering is modeled using Henyey-Greenstein phase functions. We use a direct Monte Carlo (MC) method as a baseline anisotropic radiative transfer model that requires no directional assumptions (e.g. diffuse medium and isotropic scattering in two-flux model) to compute accurate values of the downwelling longwave radiation (DLW) for different aerosol concentrations and properties. The present work proposes two scaling rules that correct the surface DLW calculated by assuming isotropic

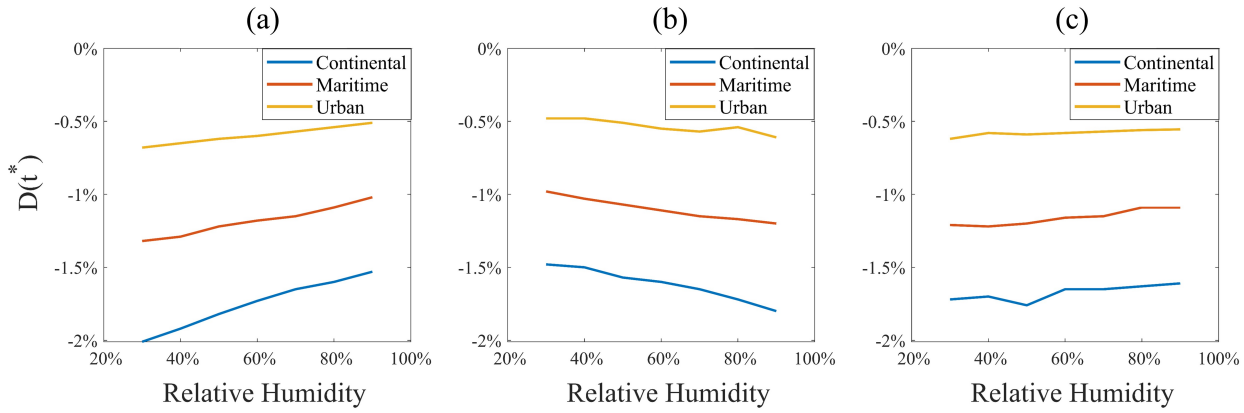

Figure 4.8: Sensitivity of the anisotropic correction factors to ambient relative humidity when $t^* = 30$ under three scenarios: (a) hold AOD constant and change κ_a of atmospheric gases due to changing water vapor content. (b) hold κ_a constant and vary AOD. and (c) the combined effects from (a) and (b).

scattering and diffuse radiative properties.

The first scaling rule is input based, and is used to scale the input optical properties such as extinction coefficient and the single scattering albedo values as done in the widely used δ-M approximation. The second scaling rule is net result based. The net result based method scales the output surface DLW based on the results from detailed MC simulations. Henyey-Greenstein phase functions are used to approximate Mie scattering equations. The latter method and is presumed to be more accurate than the former. The latter net result based approach is also substantially more expensive computationally, and is used here as a benchmark for the validity of the δ-M approximation.

The correction factor $D(t^*) = (q^-_{ani} - q^-_{iso})/q^-_{ani}$ correlates exponentially with the normalized aerosol optical depth t^*, i.e. $D(t^*) = -c/\eta(e^{-\eta t^*} - 1)$. Detailed simulations were performed for both aerosol-type-neutral and aerosol-type-dependent cases. For aerosol-type-neutral cases, D is also a function of asymmetry factor e_g, and the coefficient c is expressed as $c = e_g A$. Regression coefficients A and η are provided for both backward and forward scattering cases. More generally, the anisotropic effect is dependent on aerosol composition. For aerosol-type-dependent cases, the regression coefficients c and η for three types of aerosols (urban, continental and maritime) are also investigated. For all cases under consideration, the correction factor D is an exponential function of t^*, revealing the underlying nature of the anisotropic scattering correction.

The δ-M approximation is found to be accurate when $t^* < 5$ (equivalent to surface AOD < 0.5). For values of t^* of the order of 30 (equivalent to surface AOD equal to 3), the error incurred by the isotropic scattering assumption is of the order of 2.0% ($\approx 5\,\mathrm{W\,m^{-2}}$). The relative offset is highest for continental aerosols and lowest for urban aerosols, but the much higher values of AOD observed in urban areas contribute to a more significant correction in these cases, and may represent a relevant bias in DLW values for cities such as Beijing and Kanpur. The influence of relative humidity on the correction factor is found to be negligible even at very high aerosol loads.

In summary, this work proposes two scaling rules to expedite surface DLW calculations by means of corrections to the isotropic scattering assumptions. Optimal scaling rules for urban, continental and marine aerosols are reported. The input-scaling approach (δ-M approximation) is generally accurate for relatively low aerosol loading values observed in non-urban areas, while the proposed net-result-based scaling is valid for all values of aerosol loading, including high aerosol urban areas, and rural and urban areas affected by large-scale fire pollution.

4.6 Acknowledgement

Chapter 4, in full, is from the publication: Z. Liao, M. Li, and C. F. M. Coimbra (2019) " Anisotropic Corrections for the Downwelling Radiative Heat Transfer Flux from Various Types of Aerosols " *International Journal of Heat and Mass Transfer* , 136, 1006-1016. The dissertation author is the first author of this manuscript.

Chapter 5

Spectral cloud optical property estimation using real-time GOES-R longwave imagery

5.1 Introduction

Despite the rapid growth of solar installation, the variability of solar power hinders its large scale deployment, and serves as a challenge in replacing fossil fuels with solar power. This variability mainly comes from cloud coverage. Long-term average solar power output is well characterized by diurnal and seasonal changes in solar insolation and average cloud cover but the short-term forecast is much more difficult due to the meteorological volatility. Due to the lack of real-time, accurate estimates of cloud optical properties, cloud are typically oversimplified in solar forecasting applications. Therefore, this chapter aims to provide a solution for real-time cloud estimation that can be applied to various locations and requires minimal data dependencies.

A data driven approach for estimating cloud optical properties called Spectral Cloud Optical Property Estimation (SCOPE) method is proposed in this chapter. Remote sensing data are acquired by geostationary satellites GOES-16, which makes high temporal (10-min) and spatial (2 km) resolution estimates available across the entire United States, and this forms the basic data source for SCOPE method. This method integrates the GOES-R satellite imagery with radiative modeling mentioned in previous chapters.

Basically, SCOPE estimates the cloud optically properties by solving the constrained optimization problem involving the outgoing longwave radiation (OLR) at the top of the atmosphere (TOA). By comparing

the measurements of the true OLR and modelled $\widehat{OLR}$, the cloud optical depth (COD) and cloud bottom height (CBH) and cloud layer thickness are evaluated by the optimizing function:

$$\text{minimize} \quad f(OLR, \widehat{OLR}(x)) \tag{5.1}$$

$$\text{subject to} \quad x \in \chi, \tag{5.2}$$

where f is the objective function, and x encodes three variables for cloud optical properties mentioned above.

This chapter will explain the basics of this method in detail and introduce some improvement options including aerosol calibration, multi-layer detection and ice cloud correction.

5.2 Data Acquisition

There are mainly two data sources: remote sensing data from the latest generation of the Geostationary Operational Environmental Satellite (GOES) system: the GOES-R series, and ground telemetry data from SURFRAD stations.

The GOES-R series consists of four identical satellites, each equipped with a suite of nadir-pointing, solar-pointing, and in situ instruments. In the framework of this study, only data from the nadir-pointing Advanced Baseline Imager (ABI) are used. Compared to the imagers on the previous generation of GOES, the ABI provides data at five times the temporal resolution (full disk every 15 min and CONUS every 5 min), four times the spatial resolution (0.5–2.0 km), and three times the spectral resolution (16 spectral bands). Fig. 5.1 shows the calibrated spectral response of each channel.

SCOPE considers the band averaged spectral radiance (mW $m^{-2}sr^{-1}cm$) from the ten longwave channels (7–16), which have a spatial and temporal resolution of 2.0 km and 5-min, respectively. A full year of data (1/1/2018–12/31/2018) was retrieved from publicly available sources and processed to extract the intensity per channel for the pixel in the zenith direction of the target ground sites. Each ABI data file includes three UTC timestamps, corresponding to the start, center, and end of the scan. To maintain compatibility with real-time applications, the end timestamp, rounded up to the next nearest 5-min interval, is used to index the data. The result is one multivariate time-series per target site, consisting of eleven columns: one for the timestamp index and the remaining ten columns for the band averaged intensity measured by the ABI

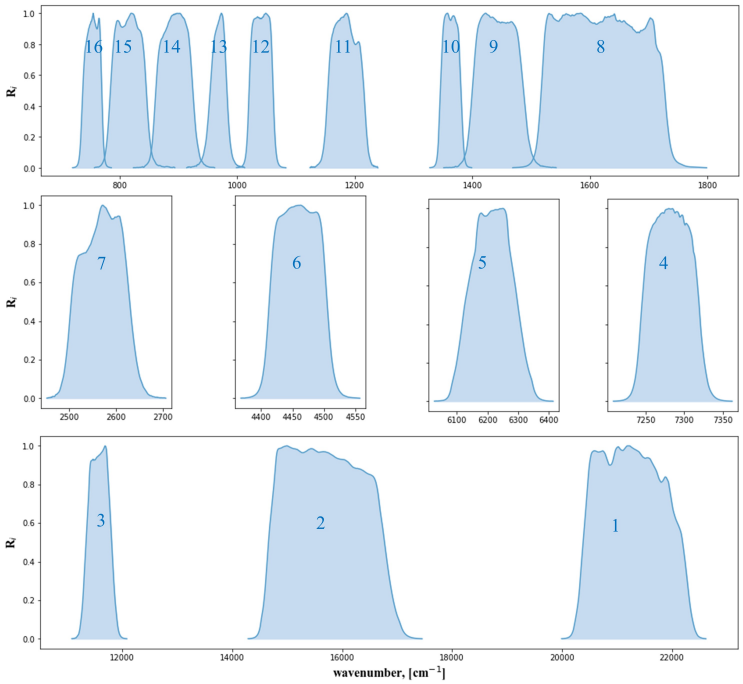

Figure 5.1: The spectral response function (SRF) of each channel [R_i] from calibration data of the GOES-16 ABI. Data are retrieved from http://cimss.ssec.wisc.edu/goes/calibration/.

longwave channels.

Apart from remote sensing data, ground measurements such as air temperature and relative humidity are also required for this method. This work uses the long-term measurements of the surface radiation budget provided by the Surface Radiation Budget Network (SURFRAD) across the United States. There are seven active SURFRAD stations: Bondville, Illinois (BON); Desert Rock, Nevada (DRA); Fort Peck, Montana (FPK); Goodwin Creek, Mississippi (GWN); Pennsylvania State University, Pennsylvania (PSU); Sioux Falls, South Dakota (SXF); and Table Mountain, Boulder, Colorado (TBL). Table 5.1 summarizes the stations, while Fig. 5.2 shows the locations of the stations. Each station provides a range of irradiance and meteorological measurements at a 1-min resolution, along with quality control (QC) flags per variable. For this study, the following ground measurements are used: ambient air temperature [Ta (K)], relative humidity [RH (%)], global horizontal irradiance [GHI (W m^{-2})], direct normal irradiance [DNI (W m^{-2})], and downwelling longwave radiation [DWL (W m^{-2})]. We retrieved a full year of data (1/1/2018–12/31/2018) from each of the seven stations, converted all variables to SI units, and then re-sampled the data to 5-min backward-averaged values to match the GOES-R CONUS scan rate. Note that only ambient air temperature and relative humidity

Table 5.1: Summary of the seven SURFRAD stations: three-letter station code, latitude and longitude. The elevation (β) and azimuth (α) look angles are from the stations to GOES-16 (GOES-East), with $\alpha = 90^o$ and $\alpha = 180^o$ corresponding to due East and South, respectively.

Station	Latitude(^{o})	Longitude(^{o})	$\beta(^o)$	$\alpha(^o)$
BON	40.1	-88.4	41.7	160
DRA	36.6	-116.0	29.9	124.6
GWN	48.3	-105.1	27.5	142.4
FPK	34.3	-89.9	47.2	155.0
PSU	40.7	-77.9	42.8	175.8
SXF	43.7	-96.6	35.2	150.4
TBL	40.1	-105.2	34.3	138.1

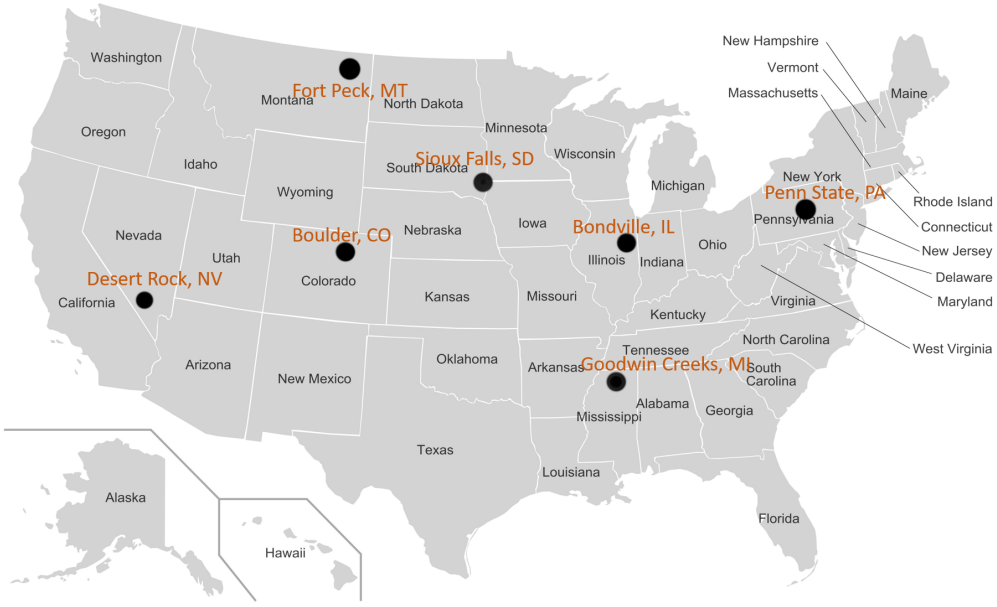

Figure 5.2: The locations of the 7 SURFRAD stations.

are used as inputs to SCOPE, while GHI, DNI, and DLW are used for validation purposes.

5.3 Basics of SCOPE Method

As previously mentioned, SCOPE aims to solve the constrained optimization problem involving the outgoing longwave radiation (OLR) at the top of the atmosphere (TOA). Rather than using broadband OLR, SCOPE considers the upwelling flux from n discrete spectral bands [$F_i^{\uparrow}$(W m^{-2})] because the spectral response of clouds varies throughout the spectrum, providing additional information that can be leveraged to estimate cloud properties:

$$\text{minimize} \quad \sum_{i=1}^{n} f(F_i^{\uparrow}, \hat{F}_i^{\uparrow}(x)) \tag{5.3}$$

$$\text{subject to} \quad x \in \chi, \tag{5.4}$$

where $\hat{F}_i^{\uparrow}(x)$ is the model estimate and x encodes the cloud optical properties.

Although the full spectrum data are covered in the 16 ABI data, our current SCOPE method is designed to only consider the longwave spectrum. Here is the rationale for that:

- unified day and night operation: utilizing longwave data enables a unified approach for estimating cloud properties during both day and night;
- independent of view angles: longwave irradiance in the atmosphere can be approximated to be diffuse, thereby removing irradiance geometric dependencies between the position of the satellite, sun, and ground sensors;
- two-flux approximation: because of the diffuse nature of longwave irradiance, a two-flux radiative model13 can be used to estimate spectral longwave irradiance in the entire atmosphere at a minimal computation cost;
- surfaces approximated as black: unlike shortwaves, most surfaces (e.g., grassland, desert, and ocean) can be approximate as black in the longwave spectrum, thereby ensuring reliable performance of the method across climatically diverse regions and all seasons;
- retrieve cloud temperature: the outgoing longwave irradiance also provides information about cloud top temperature (i.e., cloud altitude), while outgoing shortwave irradiance is independent of cloud temperature

5.3.1 Data Pre-processing

Pre-processing is required for the satellite data. From the band-averaged intensity provided by the GOES-R ABI level 1b Radiance product, the upwelling flux per channel i is computed as:

$$F_i^{\uparrow} = \pi I_{\nu,i} \int R_i(\nu) d\nu, \tag{5.5}$$

where $R_i(\nu)$ is the Spectral Response Function (SRF) for each channel i from the ABI calibrations, as shown in Fig. 5.1.

Since $F_i^{\uparrow}$ varies more than an order of magnitude across the longwave spectral range of 0-3000 cm^{-1}, SCOPE uses normalized $F_i^{\uparrow}$, which is denoted as $[F_i^*(\text{-})]$, to prevent channels with large $F_i^{\uparrow}$ from biasing the estimates of cloud properties.

$$F_i^* = \frac{F_i^{\uparrow}}{E_{b,i}(T)}, \tag{5.6}$$

where $E_{b,i}$(W m^{-2}) is the blackbody emissive power per channel i at temperature T:

$$E_{b,i}(T) = \int_{\nu_i}^{\nu_{i+1}} \frac{2h\nu^3}{c^2} \frac{1}{e^{\frac{h\nu}{k_B T}} - 1} d\nu, \tag{5.7}$$

where ν_i is the lower-bound wavenumber in ith channel, h is the Planck's constant with a value 6.6261×10^{-34} J s; k_B is the Boltzmann constant with a value 1.3806485×10^{-23} J/K; c is the speed of light with a value 299792458 m/s. After this normalization, each channel receives uniform weight in the later optimization process.

5.3.2 Estimation Cloud Optical Properties

Therefore, we select channels 8–10 to estimate zT and then use channels 11 and 13–15 to estimate corresponding s and Dz. Fig. 5.3 outlines the main algorithm of SCOPE method.

5.4 SCOPE 2.0: Further Improvements

5.4.1 Ice Clouds

For basic SCOPE method, only gases, aerosols and water droplets are considered. However, in reality, clouds in high altitudes contains some ice crystals, whose optical properties are different from that of water droplets. Therefore we estimated extinction and absorbing coefficients for different ice clouds according to their altitude. Fu et al. presented an accurate parameterization for the infrared radiative properties of cirrus

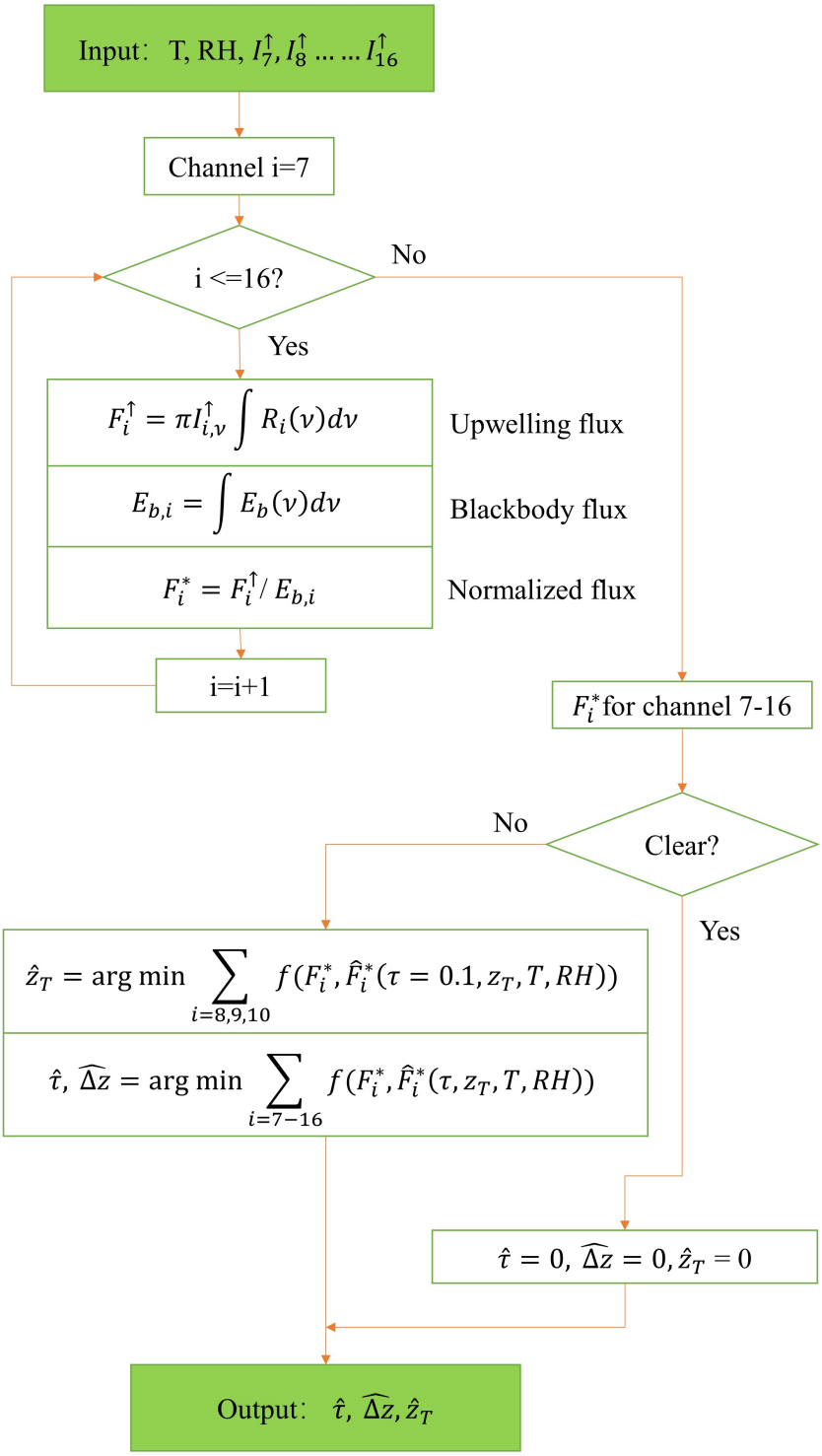

Figure 5.3: SCOPE Algorithm Flowchart

clouds where ice crystals exist[103]. For the single-scattering calculations, a composite scheme is developed for randomly oriented hexagonal ice crystals and is accurate for a wide range of size parameters. The 28 ice crystal size distributions adopted in Fu(1996) are used in the present study, which were based on in situ aircraft observations from both mid-latitude and tropical regions [104]. This is shown in Fig. 5.4. Based on aircraft observations, the width of an ice crystal, D, is related to the length L. The aspect ratio, D/L is estimated as:

$$D/L = \begin{cases} 1.00 & \text{if } 0 < L \leq 30\mu m \\ 0.80 & \text{if } 30 < L \leq 80\mu m \\ 0.50 & \text{if } 80 < L \leq 200\mu m \\ 0.34 & \text{if } 200 < L \leq 500\mu m \\ 0.22 & \text{if } L \geq 500\mu m \end{cases}$$

The ice water content (IWC) and generalized effective size D_e are defined in the forms:

$$IWC = \frac{3(3)^{1/2}}{8}\rho_i \int_{L_{min}}^{L_{max}} DDLn(L)dL \tag{5.8}$$

$$D_e = \frac{\int_{L_{min}}^{L_{max}} DDLn(L)dL}{\int_{L_{min}}^{L_{max}} [DL + \frac{3^{1/2}}{4}D^2]}, \tag{5.9}$$

where $n(L)$ denotes the ice crystal size distribution L_{min} and L_{max} are the minimum and maximum lengths of ice crystals, respectively, and ρ_i is the density of ice. Fu described a detailed method to calculate absorption and extinction coefficients as well as single scattering albedo

The bulk scattering properties of ice clouds are shown to be strongly dependent on the effective particle size at each wavelength. A parameterization of these bulk single-scattering properties is developed based on these results. The single-scattering properties are parameterized as the function of effective particle

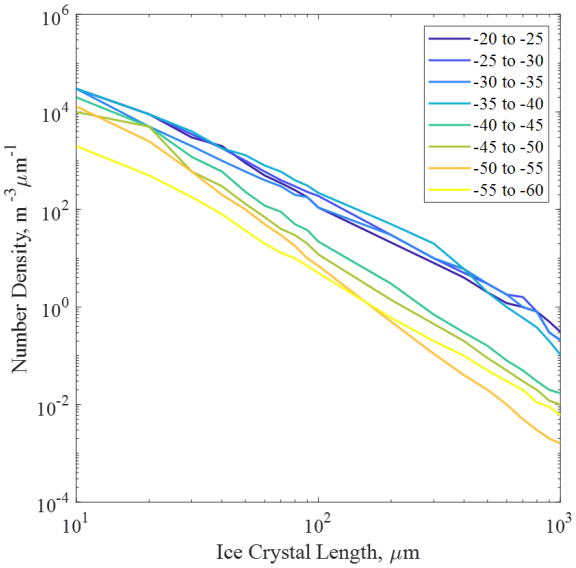

Figure 5.4: Ice crystal size distribution in cirrus clouds based on in situ aircraft observations

size at each wavelength as follows:

$$Q_e = \frac{2 + \eta_1 D_e^{-1}}{1 + \eta_2 D_e^{-1} + \eta_3 D_e^{-2}} \tag{5.10}$$

$$Q_a = \frac{\epsilon_0 + \epsilon_1 D_e^{-1}}{1 + \epsilon_2 D_e^{-1} + \epsilon_3 D_e^{-2}} \tag{5.11}$$

$$e_g = \frac{\zeta_0 + \zeta_1 D_e^{-1}}{1 + \zeta_2 D_e^{-1} + \zeta_3 D_e^{-2}}, \tag{5.12}$$

where η_i, ϵ_i and ζ_i are fitting coefficients that are functions of wavelength which can be found in Table 1. from Yang et al[105]. Q_e and Q_a are extinction and absorption efficiencies respectively and e_g is the asymmetry factor that was mentioned in previous chapter. The extinction and absorption coefficients are calculated from the efficiencies by $\kappa = N(\pi D_e^2/4)Q$ and single scattering albedo $\tilde{\omega}$ is calculated by $\tilde{\omega} = 1 - Q_e/Q_a$.

5.4.2 Multi-layer Detection

The method described previously assumes the presence of single-layer clouds. However, when there presents more than one layer, higher layer clouds would interrupt the retrieval of the information about lower clouds. A lot of research has been done to detect multi-layer clouds, but most of them requires additional instruments or datasets, like A-train sensors [106], millimeter-wave cloud radar (MMCR) combined with a micropulse lidar(MPL) and rotating shadowband spectrometer (RSS) [107]. Since our work aims to use

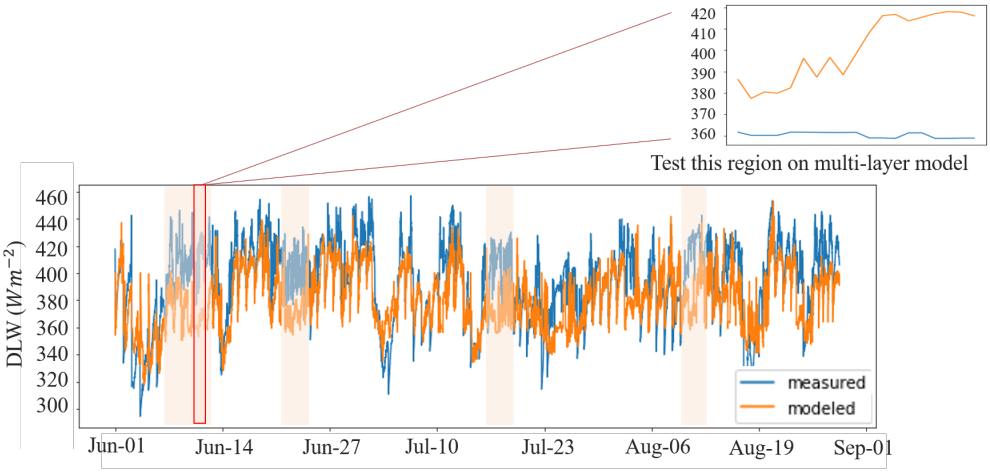

Figure 5.5: Downwelling Longwave Radiation comparison between the measurements and model results. Shaded area indicates the existence of lower cloud bottom height.

minimal input information to estimate cloud properties, attempt to detect multi-layer has been done.

Fig. 5.8 shows the comparison between measured downwelling longwave radiation and the DLW calculated from the estimated cloud properties using the atmospheric model. For the shaded areas, DLW is underestimated by a huge amount, which indicates a much lower cloud bottom height. Therefore, there are three possibilities: z_T is overestimated, cloud thickness is underestimated, or multi-layer cloud exists. In the shaded parts, since the deviation is too large, the last situation is most possible and we tried to add different lower cloud combinations and examine the resultant OLR and DWL.

A sensitivity analysis on COD and on the layer position of the lower cloud is presented in Fig. 5.6 and Fig. 5.7 respectively. Channel 8-10, also known as water vapor channels, are insensitive to COD but varies with cloud height, as these two figures show. Therefore, Channel 8-10 can be used to find the lower cloud position just like normal SCOPE method did. Then the other channels are used to find best COD and cloud layer combinations. DWL as a validation parameter is used afterwards to see whether the new combination gives satisfactory RMSE for DWL.

A flow chart is shown in Fig. 5.8 describing how the Multi-layer cloud detection method works. The threshold value ϵ varies for different locations and could be found statistically. For this work, ϵ of a location for RMSE is set to be one standard deviation higher than the average RMSE for the training set of that location. After this loop, it is possible that the upper bound of lower-layer cloud merges with the lower bound of the upper-layer cloud, which give a big vertically extended cloud layer. This coincides with the

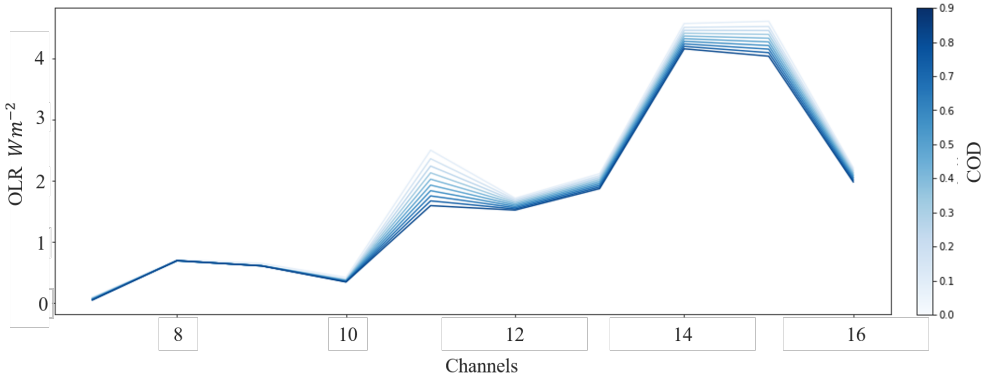

Figure 5.6: Sensitivity Analysis for lower clouds on cloud optical depths.

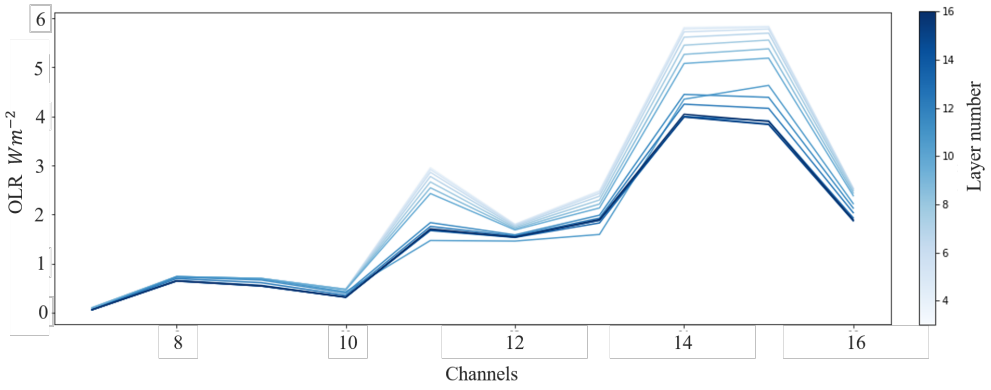

Figure 5.7: Sensitivity Analysis for lower clouds on cloud position.

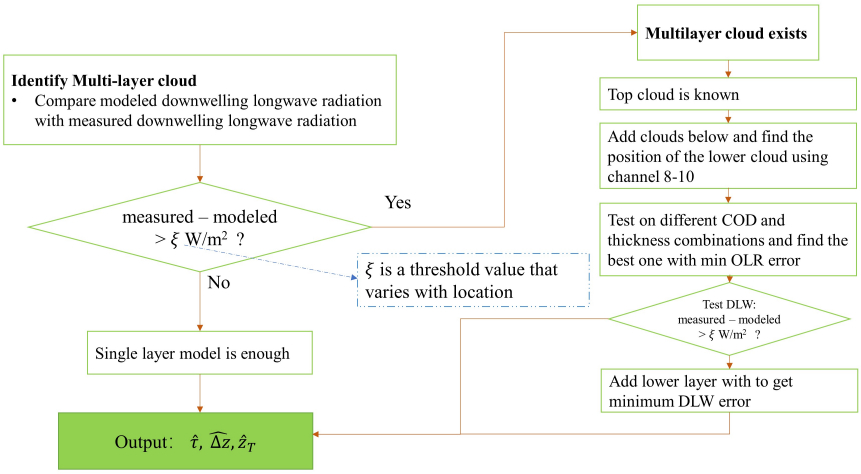

Figure 5.8: SCOPE2.0 that considers multi-layer clouds.

second possibility that is mentioned previously.

5.5 SCOPE Results

The accuracy of the proposed SCOPE method on clear and cloudy periods is evaluated, with different methods we compare the results for three conditions: (1) clear periods, (2) SCOPE 1.0 cloudy periods, (3) cloudy periods. For the daytime periods. Although SCOPE method is capable of estimating clouds in nighttime conditions, for the further purpose of solar radiation modeling and forecasting, only daytime condition is considered in this study.

$\theta_z \leq 85^o$ is used to identify daytime condition. A harder method is used to identify clear-sky condition, based on measured GHI which is described in Inman et al, and separates the data into daytime clear and daytime cloud datasets. [108]. Over one full year(1/1/2018-12/13/2018), about 15% of the daytime data from all seven sites is identified as clear.

Due to the lack of direct accurate measurements of cloud optical properties at 7 sites, the performance of the SCOPE method is evaluated using the following metrics:

- Reproducing $F_i^{\uparrow}$ across the 10 longwave channels and calculating the root-mean-squared error for each of them comparing with the satellite measured *OLR*.

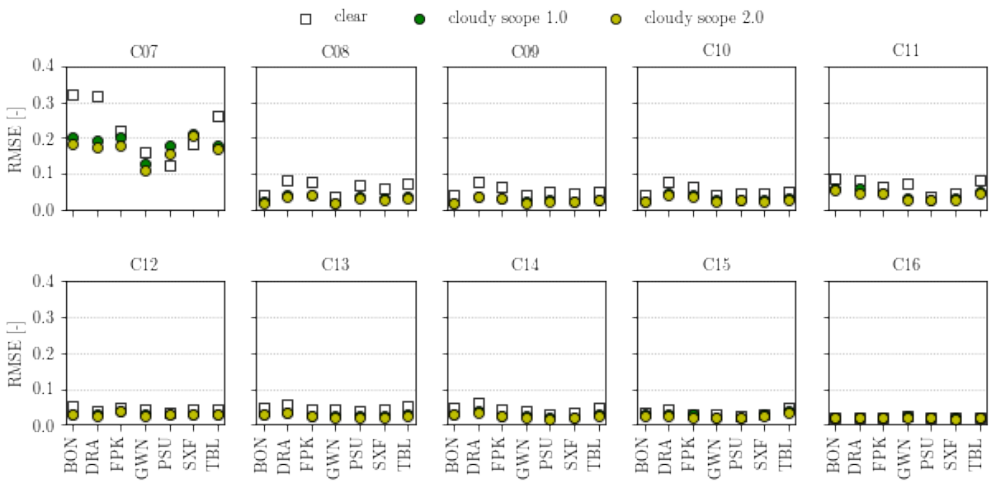

Figure 5.9: The RMSE between the measured and modeled normalized upwelling flux per channel for the ten longwave channels (7–16), seven SURFRAD stations, and 3 evaluated cases: (1) daytime clear-sky, (2) daytime cloudy-sky (SCOPE 1.0), (3) daytime cloudy-sky (SCOPE 2.0).

- Calculating the downwelling longwave radiation with estimated cloud properties using the model and compare it with the measured *DLW*.
- Calculating GHI with estimated cloud properties using Monte Carlo simulation and compare it with the SURFRAD measured GHI.

5.5.1 Root-Mean-Squared Error for *OLR*

First, the accuracy of the method in reproducing $F_i^{\uparrow}$ across the ten longwave channels is evaluated. If the (COD, z_T, Δz) estimates are correct, then the measured and modeled fluxes should match for all ten channels. Fig. 5.9 shows the root mean square error (RMSE) of the normalized value F_i^* for the ten longwave channels for all 7 stations. Overall, the 7 stations show similar levels of RMSE in each channel, with the largest error in Channel 7, which is the shortestwave window and lies at the boundary of the shortwave-longwave ranges and has a known reflected solar component during the day.

For the simplest clear-sky condition, the radiative model is run with COD = 0 and an estimated F_i^* is reproduced. RMSE in clear-sky condition is higher than that in cloudy-sky condition as expected since in cloudy-sky condition, SCOPE method is used to minimize this error. Therefore, other validation methods are necessary.

5.5.2 Downwelling Longwave Radiation

The measured downwelling longwave irradiance at the surface (DWL) is compared with DWL modweled by the radiative model ($\widehat{DWL}$) using the estimated (COD, z_T, Δz). Since the instruments at the SURFRAD sites have a spectral range of $\nu_1 = 200cm^{-1}$ to $\nu_2 = 3333cm^{-1}$, DWL is computed as

$$\widehat{DWL} = \pi \int_{\nu_1}^{\nu_2} \hat{I}_\nu^{\downarrow} d\nu, \tag{5.13}$$

where $\hat{I}_\nu^{\downarrow}$ is the downwelling spectral intensity at the surface ($Wm^{-2}sr^{-1}cm$).

Fig. 5.10 visualizes the DWL RMSE for all the cases. As expected, the root-mean-square error (RMSE) of the cloudy-sky DWL is higher than those of the clear-sky as the cloud optical thickness and physical location (COD, z_T, Δz) are unknown a priori. In addition, the daytime cloudy-sky DWL is under-predicted (MBE¡ 0) for all sites except TBL, indicating that SCOPE either over-estimated z_T or underestimated COD or Δz. DWL RMSE for SCOPE 2.0 is much lower than than that for SCOPE 1.0 since SCOPE 2.0 utilizes DWL as a tuning parameter to find the information for lower clouds. Therefore, to compare the performance of SCOPE 1.0 and 2.0 other validation method should be used.

5.5.3 Monte Carlo validation

Since both SCOPE methods use longwave radiation as inputs, shortwave radiation can be used as validation. Shortwave radiation, also known as solar irradiance is measured as global horizontal irradiance (GHI). Two-flux approximation is not feasible for shortwave bands therefore we have to use Monte Carlo simulation to get the modeled GHI with the estimated cloud properties obtained from SCOPE methods. Fig. 5.11 shows the RMSE between the measured and modeled GHI for seven SURFRAD stations. Lower RMSE obtained from SCOPE 2.0 tests, which means the additional features and considerations help to improve the estimation accuracy of clouds.

5.6 Conclusions

The single-layer and multi-layer SCOPE method for real-time, direct estimation of cloud optical properties from high-resolution longwave remote sensing data is presented. By considering only the longwave

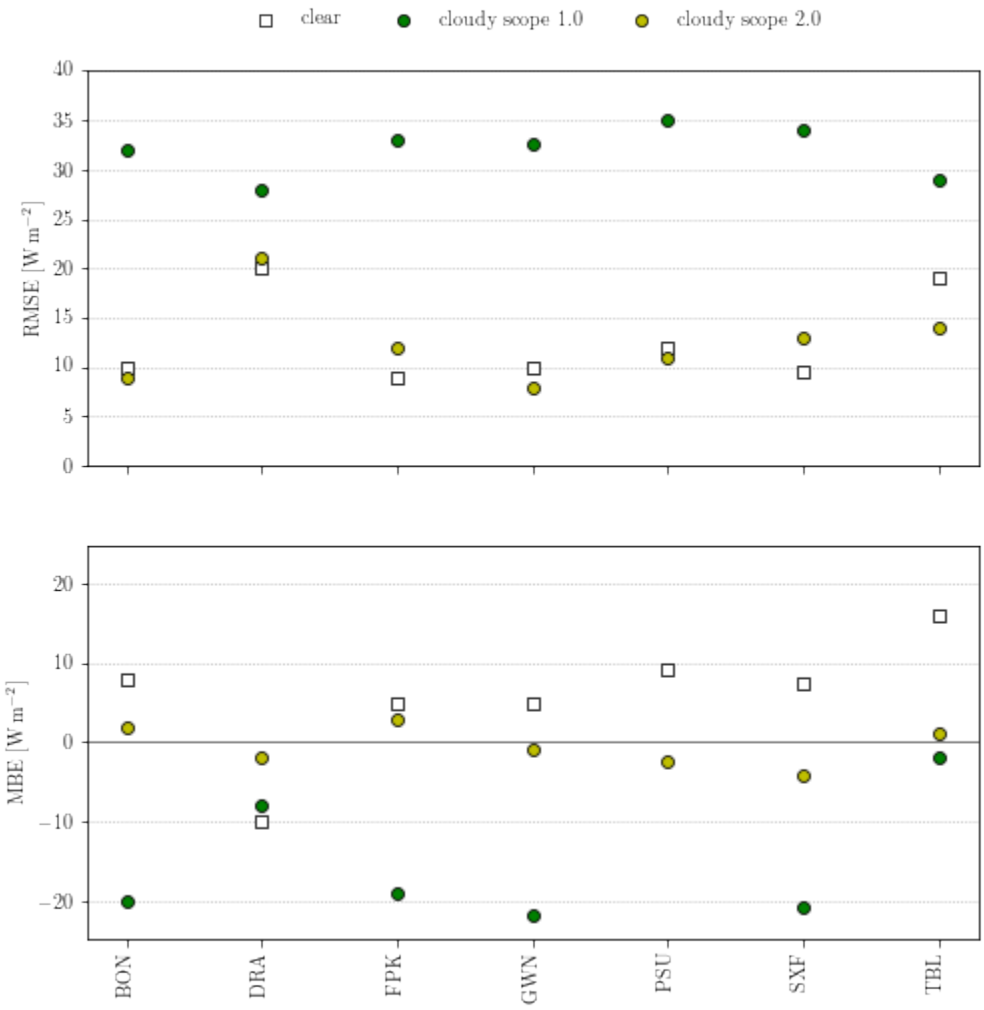

Figure 5.10: The RMSE and MBE between the measured and modeled *DWL* for the seven SURFRAD stations and 3 evaluated cases: (1) daytime clear-sky, (2) daytime cloudy-sky (SCOPE 1.0), (3) daytime cloudy-sky (SCOPE 2.0).

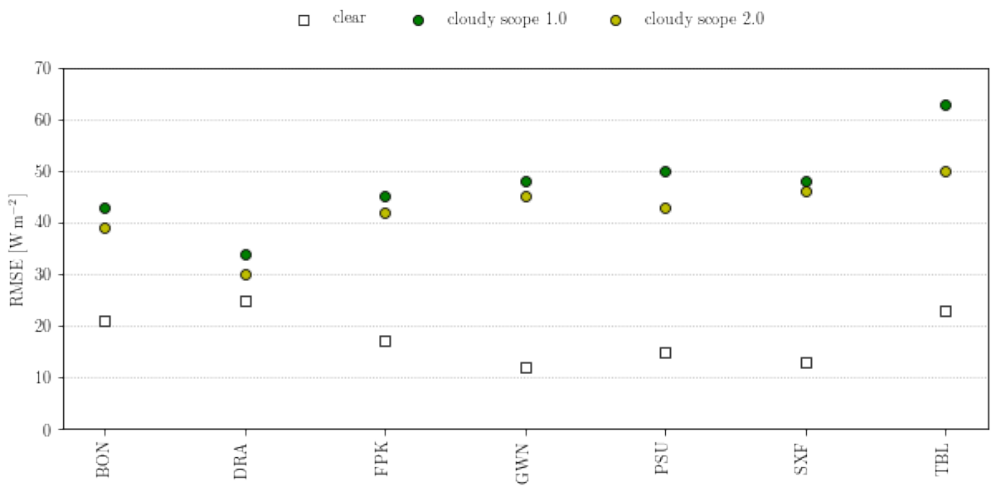

Figure 5.11: The RMSE between the measured and modeled GHI for the seven SURFRAD stations and 3 evaluated cases: (1) daytime clear-sky, (2) daytime cloudy-sky (SCOPE 1.0), (3) daytime cloudy-sky (SCOPE 2.0).

spectrum, the method provides a unified approach to estimating cloud properties during day or night and does not need to consider the view angle of the instruments. For a basic SCOPE method, remote sensing data from GOES-R are used as well as minimal ground measured variables as inputs. A two-stream LBL atmospheric radiative model is used to get the estimated value for upwelling flux for each channel, which is compared with the measured channel-averaged OLR. The optimal cloud height z_T, cloud optical depth COD, and cloud thickness Δz are obtained when the comparison error is minimum. As SCOPE has minimal data dependencies, a linear correction to standard atmospheric profiles (temperature, gas, and aerosol profiles), allows SCOPE to be applied to a wide range of surface conditions and locations. SCOPE 2.0, as a improved version of SCOPE method, considering the situation of high ice clouds and multi-layer clouds, is also presented and compared.

The performance of SCOPE 1.0 and 2.0 is evaluated using a full year of data (1/1/2018 - 12/31/2018) from seven meteorically various locations across the United States for both clear and cloudy cases. For each case, SCOPE estimates cloud optical properties from the upwelling longwave radiative flux at the top of the atmosphere. As a validation, the estimated properties are used to to model the downwelling longwave radiative flux at the surface and compared against ground measurements. In SCOPE 2.0, downwelling longwave radiation is also used to estimate lower cloud information and shortwave radiation modeled from Monte Carlo simulation is compared against the ground measured GHI as a validation. SCOPE 1.0 achieves downwelling longwave RMSE within 20 W m^{-2} for clear conditions and within 40 W m^{-2} for all sky condition (clear +

cloudy). SCOPE 2.0, with the additional DWL inputs, achieves slightly better RMSE (about 2 - 10 W m^{-2}) for shortwave validation. The results indicate that SCOPE is suitable for solar forecasting applications by providing real-time accurate cloud estimates.

5.7 Acknowledgement

This chapter, in full, is from the publication in preparation: Liao, Z., and Coimbra, C. F. M. (2021) "Advanced Multi-layer Spectral cloud optical property estimation using real-time GOES-R imagery". The dissertation author is the first author of this manuscript

Chapter 6

Solar Irradiance Modeling from GOES-R Using the SCOPE Method and CNNs

6.1 Introduction

Due to the rising awareness of climate change and energy crisis, as well as the declining cost of solar panels, the market share of solar photo-voltaic power generation is increasing rapidly in the past decades. In the year of 2019, the power generation from solar PV is estimated to be 22% and with this increase, the solar PV accounts for almost 3% in global electricity generation[7] and this number was only 1.2% in 2016[8].

Despite of the rapid growth of solar PV, its market share is still very low compared to fossil fuels. The major challenge is the variability of solar power, which mainly comes from cloud coverage. This variability has the greatest effect in short-term solar power prediction. In partly-cloudy conditions, the power output from PV panels could drop to near zero in a minute [9]. This highly volatile nature of solar insolation makes it difficult to integrate PV output to electricity grid. A more accurate short-term solar power prediction helps to develop bidding strategies for real-time markets or to determine the need for operating reserves [10].

Although water vapor content and aerosol loadings also affect light absorption, short-term solar power variability mostly comes from clouds, including the optical and physical thickness, cloud bottom height and horizontal distribution[10]. Some of the current solar forecasting methods use either binary (clear or cloudy) or coarse representations of sky conditions[11]. Recent years, many studies make short-term forecasting by correlating total sky imagers to solar power output or GHI. Marquez et al. (2012) derived three sky cover(SC)

indices from the observed cloud cover via total sky imagers. They found the optimal correlation between GHI and SC indices and employed an artificial neural network (ANN) algorithm to improve the forecasting model [12]. Chu et al. (2014) proposed a automatic smart adaptive cloud identification (SACI) system for sky imagery and solar irradiance forecast. Cloud cover classification retrieved by SACI is used as an input for an artificial neural network model that predicts 1-min average global horizontal irradiance (GHI), 5-, 10-, and 15-min ahead of time[13]. Apart from ANN, convolutional neural networks (CNN) are commonly used for the task of image recognition and could be applied for short-term solar forecasting from satellite images or total sky images. For example Y. Sun et al. [10] used CNN to forecast a current PV output from a contemporaneous total-sky image (a "now-casting"). Recently, Ryu et al. [15] made a step forward to use CNN to forecast 5-20 min ahead of global horizontal irradiance using total-sky images and lagged GHI. This model performs root-mean-square error (RMSE) of 49-177 W/m^2, 93-146W/m^2, 71-118W/m^2 in sunny day, partly cloudy day and overcast day, respectively.

The current CNN-related solar forecast models rely heavily on ground instruments. In this paper, satellite data obtained from newest generation of the GOES system are utilized as input to construct a new CNN model which does not rely on ground instruments and can be applied to more places. A method called the Spectral Cloud Optical Property Estimation (SCOPE) developed by Larson et al. [11] was first applied to estimate cloud optical properties directly from high-resolution imagery from GOES-R. The resultant 3D cloud image can be used to predict GHI using CNN. This paper focuses on assessing how satellite data correlate with contemporaneous GHI (a now-cast) and in the future this could be expanded to short-term forecast using image sequences and lagged GHI.

6.2 CNN Model

A convolutional neural network is a class of deep neural network, most commonly applied to analyze image information, either image classification or regression. they are made up of neurons that have learnable weights and biases. Each neuron receives some inputs, performs a dot product and optionally follows it with a non-linearity. A typical CNN architecture consists of an input layer, some hidden layers, which are made of convolutional layers and pooling layers, and fully connected layers. Widely used CNNs, such as AlexNet [109], VGG[110], Inception[111], and ResNet[112] share a basic common framework: the input

image is sequentially passed through several Conv-Pool structure, each of which consists of a set of several convolutional layers and a pooling layer at the end. After the last Conv-Pool structure, the processed input is flattened into a vector and fed into several fully connected layers. The fully connected layers generate a regression result (to predict continuous data) or classification score (to predict discrete or categorical data).

Very little work has examined combining graphical information and neural networks for solar forecasts. In current forecasting models, ANNs are most commonly used. For example, Chu et al. feed the cloudiness calculated from a sky image and lagged output into an ANN model [113] or directly takes the mean and variance of color intensity of cloud images as input [13], which leaves out a wealth of information provided by images, which could potentially be better extracted through CNN. In recent years, some scholars developed CNN models with sky imagers, but no one used satellite images as input. And of course, little work has been done to use satellite derived 3D cloud maps as image inputs for solar modeling and forecasting.

Therefore, this work aims to build up a CNN model using either GOES-R 16-channel ABI data directly or spatial cloud optical properties obtained from SCOPE model as input data is described in Fig. 6.1 and Fig. 6.2. The configuration of the CNN model using 16-channel ABI data and SURFRAD ground measurements (called a "CNN + ABI model") is described in Fig. 6.1. The area of study has 11 by 11 pixels and since there are 16 ABI channels, the input satellite matrix is 11x11x16. Input data first go through three Conv-Pool structures. Each Conv-Pool structure includes one convolutional layer, one batch normalization layer, and one pooling layer in that order. The convolutional layer utilizes a filter size of 3×3, with a step length of one and same-value padding. The activation function used here is Rectified Linear Unit (ReLU) [114]. The first Conv-Pool structure contains 12 filters while the second and third contain 24 and 48 filters respectively. Batch normalization is used after convolution, which makes the model train faster and increases robustness [115]. 2×2 max pooling is used in the pooling layer. Max pooling, which aggregates spatially neighboring features, is considered crucial in obtaining translation-invariant features [116]. The number of filters for each convolutional-pool structure and the number of neurons in the final fully-connected (FC) layer that are mentioned above are determined by tuning the RMSE which would be described in the next section. On the other side, the ground measurements including temperature, relative humidity, zenith angle, and downwelling infrared radiation, are used to build a multi-layer perceptron (MLP) model which also includes 2 fully connected layers set. At last, the combined model produces one output of GHI with linear regression as activation function.

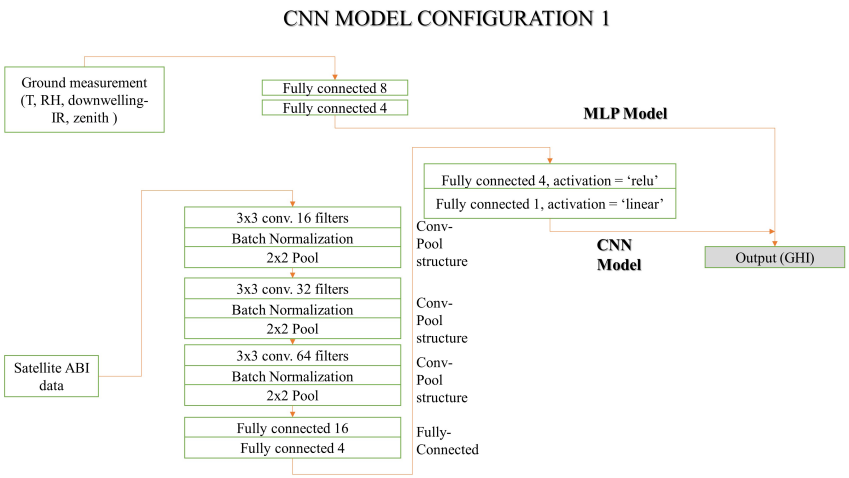

Figure 6.1: Baseline deep CNN network architecture diagram, with input data obtained directly from GOES-R ABI channels facilitated with multi-layer perceptron based on Surfrad ground measurements, went through layers of operation, and forms an output of Global Horizontal Irradiance (GHI) value.

The second model is very similar to the first one and the only difference is the input matrix. This model, we call it "CNN + SCOPE model", first runs the SCOPE model which described above to obtain the cloud optical properties matrix. There are 11x11 pixels and 18 layers so the input matrix is 11x11x18. The illustration is shown in Fig. 6.2.

6.3 Results

6.3.1 Model Tuning

We train the network using the Adam optimizer [117], a stochastic gradient descent optimizer popular in the field of machine learning. The loss function is defined as mean square error of GHI:

$$Loss = \frac{1}{N}\sum_{i=1}^{N}(\widehat{GHI}_i - GHI_i)^2, \tag{6.1}$$

where, N is the number of samples, $\widehat{GHI}_i$ is the modelled output and GHI_i is the measured output for sample i.

Since Adam is a stochastic optimizer, the final resulting model is slightly different for each model training run.To mitigate this variability, all experiments should be repeated for several times. I run 100 times

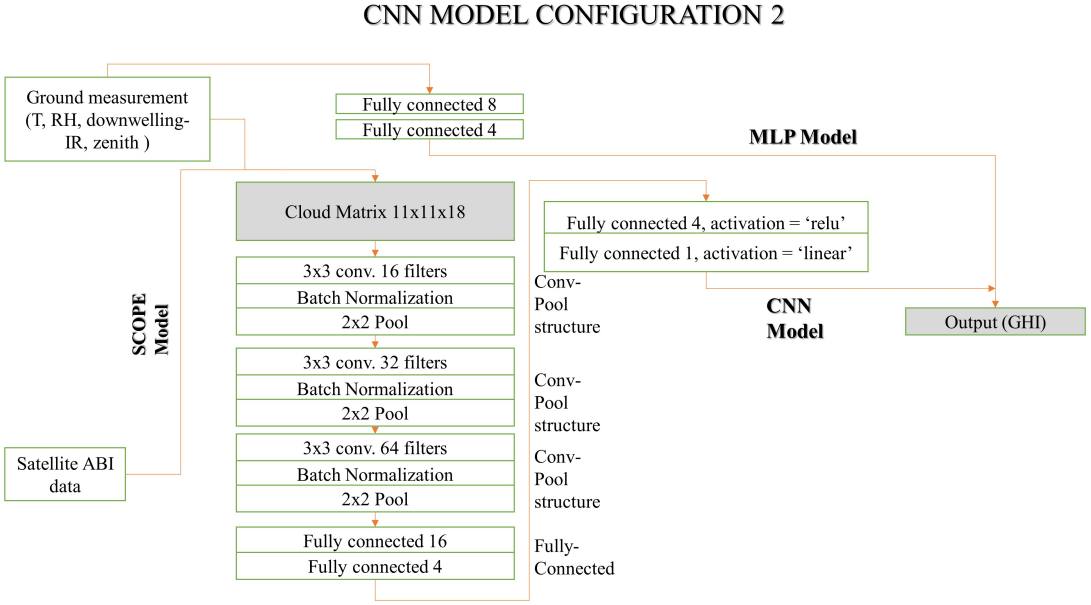

Figure 6.2: Baseline deep CNN network architecture diagram, with input data obtained from SCOPE model which represents 3D cloud optical properties, facilitated with multi-layer perceptron based on Surfrad ground measurements, went through layers of operation, and forms an output of Global Horizontal Irradiance (GHI) value.

to see what epoch number should I choose and report the results in Figure 6.3 (a). Since the loss function for validation data set starts going up after 50 epoch numbers, epoch number of 50 was chosen for all the models.

To test the robustness of our CNN model, We experiment with different architecture choices, including: model width (which is the filter number in the first convolutional layer)and model depth(number of convolutional layers and fully connected layers). They are demonstrated in Figure 6.3 (b) and (c).

Table 6.1 summarizes all the sensitivity runs we have done and the values we choose are in bold font.

Table 6.1: Summary of sensitivity analysis on SCOPE+CNN model, showing the list of value explored for each architecture choice. The values chosen for the model are in bold font

CNN Architecture Choice	Sensitivity Values
Depth (convolutional layers)	[0,1,2,**3**,4,5,6,7,8]
Depth (fully connected layers)	[0, 1, **2**, 3, 4]
Width (number of filters in first convolutional layer)	[1, 2, 3, 4, 6, 8, **12**, 16, 24]

6.3.2 CNN results

The upper figure on Fig. 6.5 shows the overall result by month. From these plots we can find that CNN model with SCOPE estimation is one of the best models that give the lowest rmse and CNN + 16

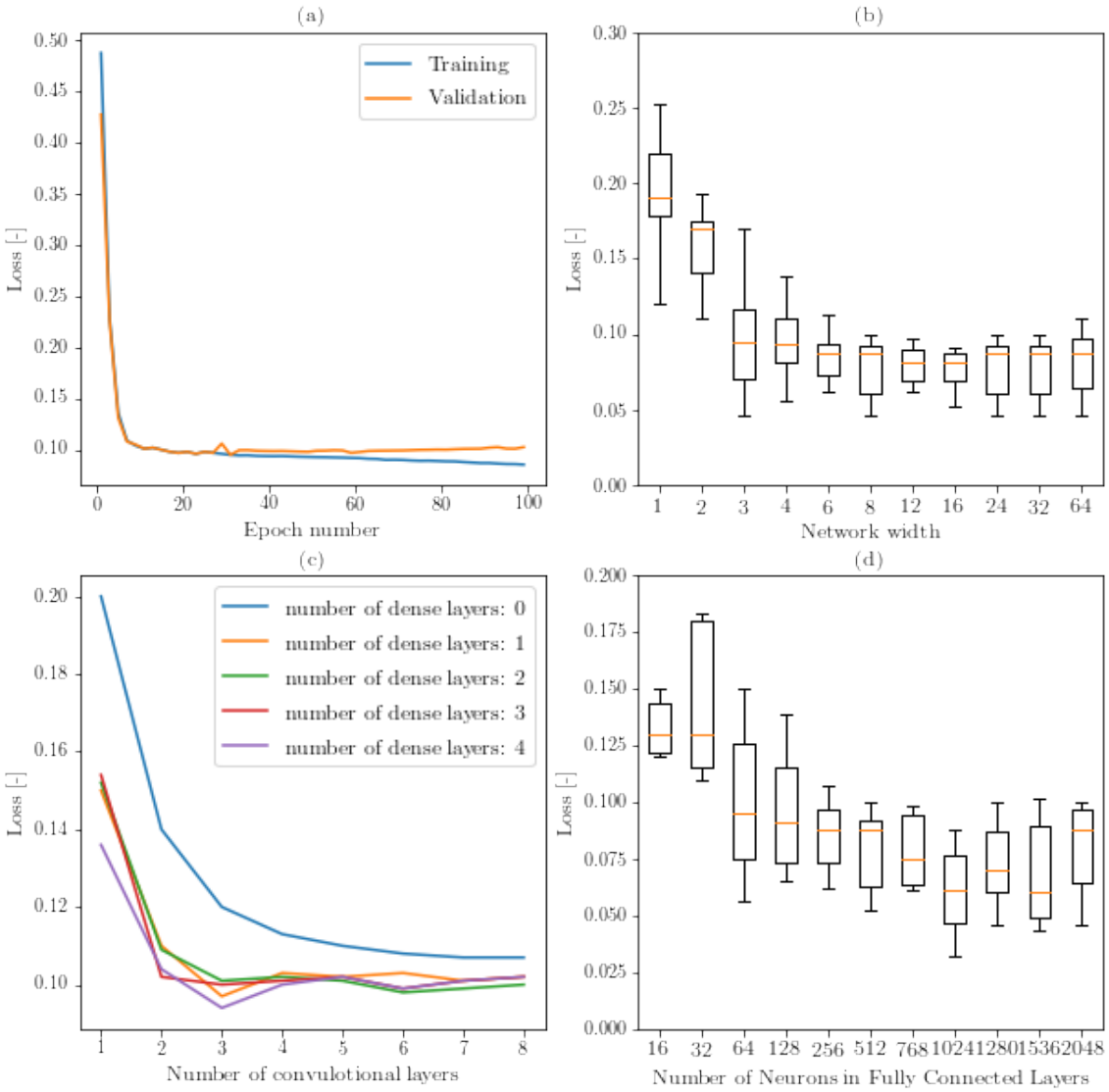

Figure 6.3: Tuning of parameters(epoch number, model width, model depth and number of neurons in FC layer) for CNN models.

ABI channels also give a similar result. But CNN model with only direct longwave channel model is much worse than the other two and close to the reference NSRDB mode. we can also observe a monthly trend for each location. The summer months generally have higher modeling error than the winter months for most locations.

The lower figure on Fig.6.5 shows the overall comparison result by site. From these plots we can most sites have similar results except for Desert Rock, where clear days are more common.

Table 6.2 is the numerical comparison of average RMSE for four models. So here is the average RMSE statistics for each model CNN+SCOPE and CNN+ 16 channels have about 45 W/m^2 error on average, which are much better than the other two.

Table 6.2: Summary of RMSE for all the models in 7 sites.

	BON	DRA	FPK	GWN	PSU	SXF	TBL	Average
NSRDB	59.6	57.4	66.1	60.6	78.4	66.9	79.5	64.8
SCOPE + CNN	42.8	30.5	47.6	50.8	47.6	48.5	62.6	44.7
10 channel + CNN	73.9	44.1	72.1	73.2	76.7	73.5	72.7	68.9
16 channel + CNN	45.0	30.2	48.8	52.3	51.8	49.8	57.6	46.3

6.4 Conclusions and Future Work

This chapter focuses on the modeling of GHI using GOES-R satellite data and ground measurements. Two proposed models, one with and one without SCOPE cloud estimation are compared and they produce average RMSE values 44.7 W/m^2 and 68.9 W/m^2 respectively. Both models perform well and yield errors that are competitive with much more complex models (such as those based on Numerical Weather Prediction). This indicates that convolutional neural networks are suitable for interpreting the information contained in satellite images and relating this information to estimate local ground irradiance. The CNN + SCOPE model yield much improved results than the CNN model that only uses 10 longwave channels. This indicates that the physical features captured by the SCOPE model are not only relevant, but contain information that is able to improve model results for a variety of solar microclimates. The CNN+16 channel model, gives similar results as the CNN+SCOPE model which is also much better than CNN+10 channel model. Therefore, we expect that the shortwave channels also contain much useful information for the modeling of solar radiation. In terms of potential future work, it is appropriate to consider adding additional physical models for the 6

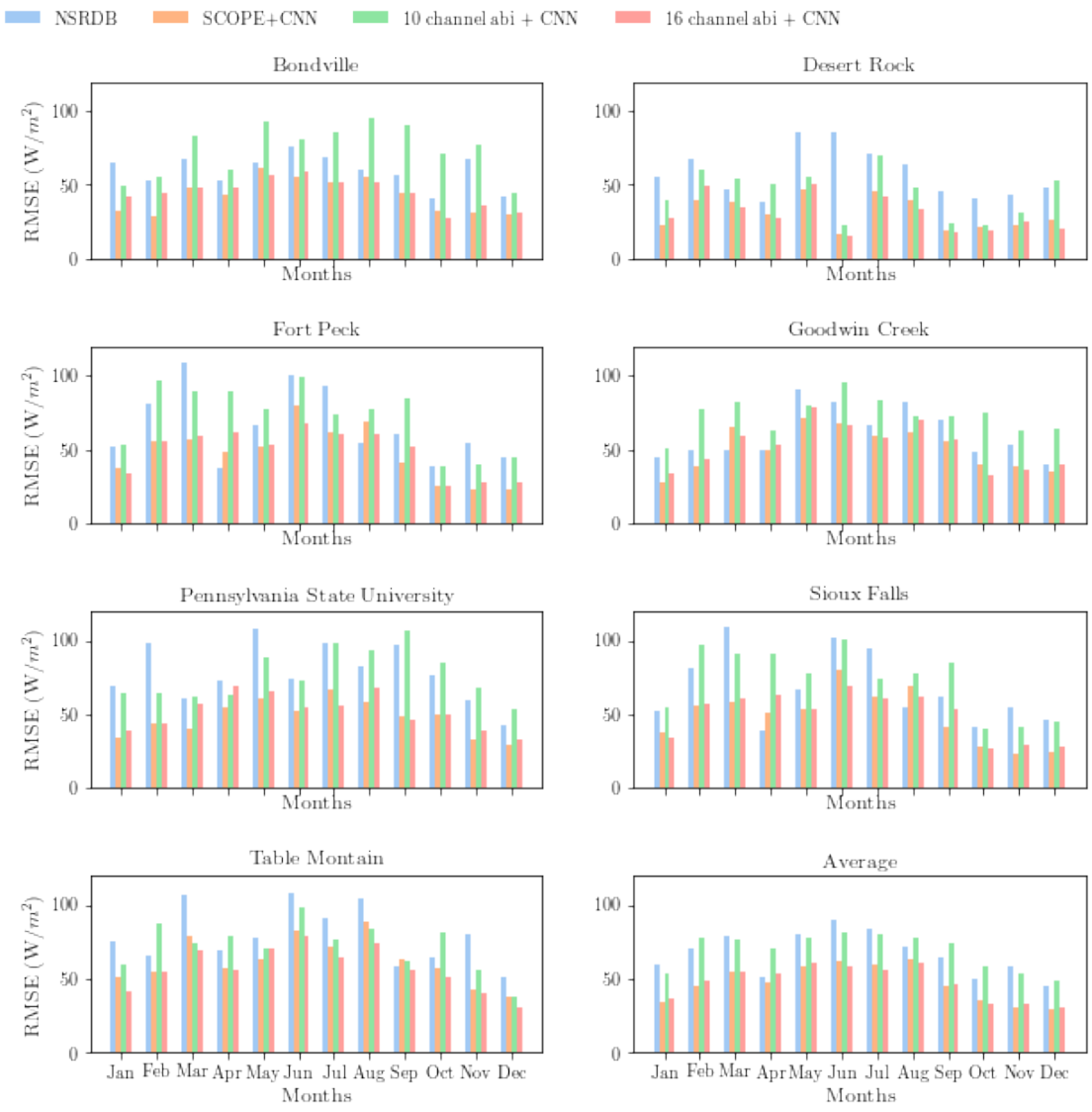

Figure 6.4: Root-mean-square errors for GHI evaluated from different models comparing to the measured GHI. Monthly results for all seven sites are presented.

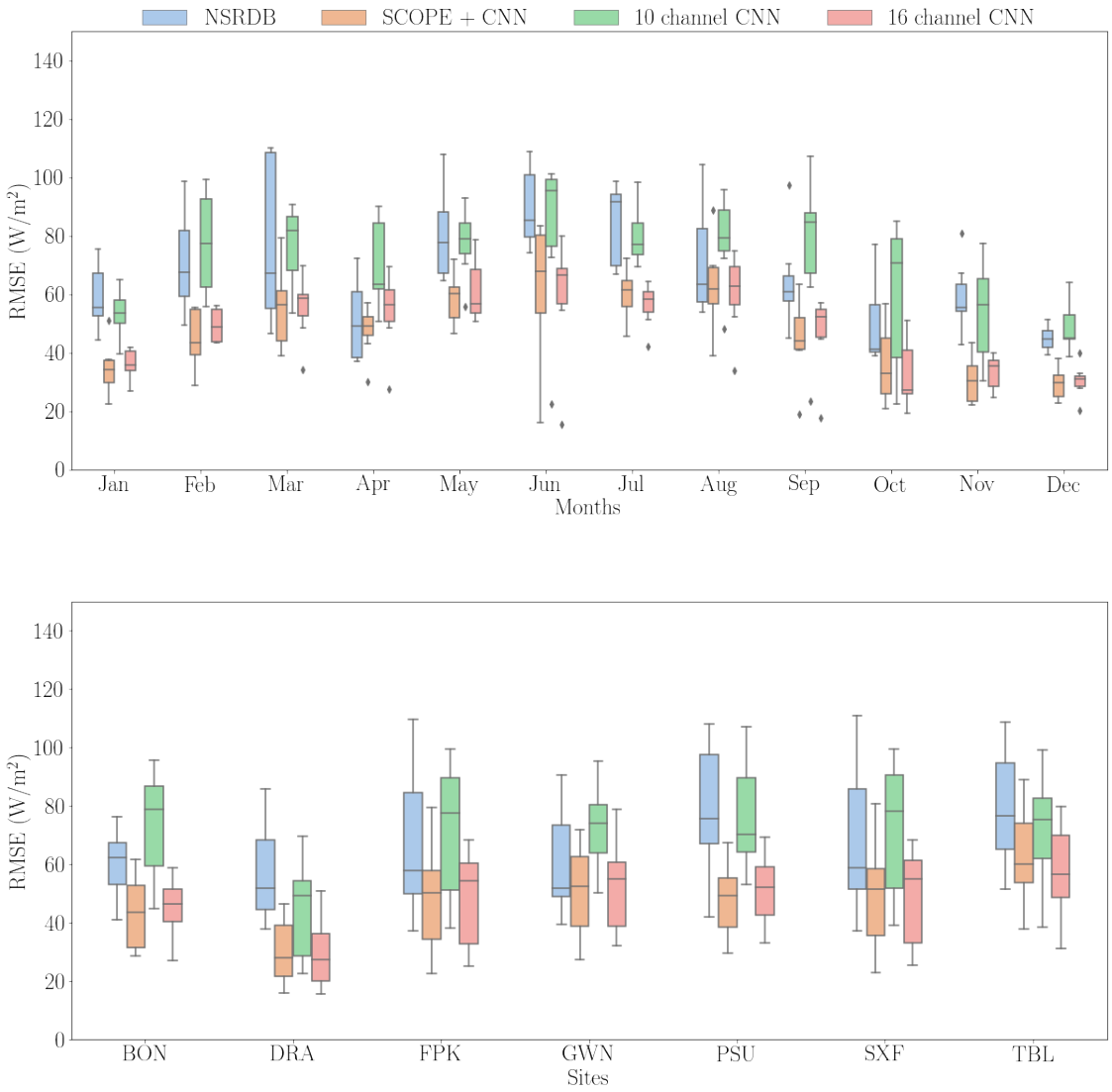

Figure 6.5: The upper figure shows the comparison of site-averaged RMSE values for different models by month; the lower figure shows comparison of month-averaged RMSE values for different models by site.

shortwave channels to the SCOPE+CNN model in order to further increase the modeling accuracy. Those steps are likely to be useful in the development of high-fidelity now-casting and short-term forecasting of ground irradiation.

6.5 Acknowledgement

This chapter, in full is from the publication in preparation: Liao, Z., and Coimbra, C. F. M. (2021) "Solar Irradiance Prediction from GOES-R imagery using SCOPE method and convolutional neural networks". The dissertation author is the first author of this manuscript

Chapter 7

Concluding Remarks

Atmospheric longwave radiation and solar shortwave radiation play a critical role on weather and climate variability, as well as on the heat balance design of solar power plants, of radiant cooling systems, and of the built environment. To quantify the spectral thermal balances of the atmosphere and engineered systems, comprehensive line-by-line radiative models are developed to simulate atmospheric longwave and shortwave radiative transfer in the Earth-atmosphere system.

First, the basics of radiative transfer and a rationale for using Monte Carlo simulations are introduced in the first two chapters. Then, in Chapter 3, an efficient spectrally resolved radiative model is developed to simulate a simplified process of longwave radiation in the atmosphere, under clear and cloudy skies. This model, with 18 vertical layers is found to achieve grid independence for DLW under the selected spectral resolution that is relevant for solar energy applications. For the non-scattering clear atmosphere (aerosol free), the surface DLW agrees within 2.91% with mean values from the InterComparison of Radiation Codes in Climate Models (ICRCCM) program, with spectral deviations below 0.035 $\mathrm{W\,cm\,m^{-2}}$. For a scattering clear atmosphere with typical aerosol loading, the DLW calculated by the spectral model agrees within 3.08% relative error when compared to measured values at seven climatologically diverse SURFRAD stations. This relative error is smaller than the aforementioned calibrated parametric model regressed from data for those same seven stations, and within the uncertainty (+/- 5 $\mathrm{W\,m^{-2}}$) of pyrgeometers commonly used for meteorological and climatological applications.

Therefore, the proposed model is capable of capturing meteorological differences between locations when compared to extensive surface telemetry, which justifies its use for calculating DLW at other locations

across the contiguous United States where measurements are not readily available. The proposed model also serves as a powerful and robust tool to study moderate to high spectral resolution interactions between atmospheric constituents within the critical longwave region of the electromagnetic spectrum.

Some additional corrections are also considered for the proposed model. One is airmass correction that allows for compensation of Earth's curvature effects. A spherical Monte Carlo simulation is used to compared the results against the results based on plane-parallel assumption. Deviations are negligible for zenith angles less than 85 degrees, so for the purpose of solar forecasting applications, the plane-parallel approximation seems more than adequate. A comprehensive Monte Carlo simulation is also used to evaluate quantitatively the accuracy of the isotropic scattering assumption in calculating surface downwelling longwave irradiance (DLW) during clear skies. Two scaling rules that correct the surface DLW calculated by assuming isotropic scattering and diffuse radiative properties.

The first scaling rule is input based, and is used to scale the input optical properties such as extinction coefficient and the single scattering albedo values as done in the widely used δ-M approximation. The second scaling rule is net result based. The net result based method scales the output surface DLW based on the results from detailed MC simulations. Henyey-Greenstein phase functions are used to approximate Mie scattering equations. The latter method and is presumed to be more accurate than the former. The latter net result based approach is also substantially more expensive computationally, and is used here as a benchmark for the validity of the δ-M approximation.

The correction factor $D(t^*) = (q^-_{ani} - q^-_{iso})/q^-_{ani}$ correlates exponentially with the normalized aerosol optical depth t^*, i.e. $D(t^*) = -c/\eta(e^{-\eta t^*} - 1)$. Detailed simulations were performed for both aerosol-type-neutral and aerosol-type-dependent cases. For aerosol-type-neutral cases, D is also a function of asymmetry factor e_g, and the coefficient c is expressed as $c = e_g A$. Regression coefficients A and η are provided for both backward and forward scattering cases. More generally, the anisotropic effect is dependent on aerosol composition. For aerosol-type-dependent cases, the regression coefficients c and η for three types of aerosols (urban, continental and maritime) are also investigated. For all cases under consideration, the correction factor D is an exponential function of t^*, revealing the underlying nature of the anisotropic scattering correction. The δ-M approximation is found to be accurate when $t^* < 5$ (equivalent to surface AOD < 0.5). For values of t^* of the order of 30 (equivalent to surface AOD equal to 3), the error incurred by the isotropic scattering assumption is of the order of 2.0% ($\approx 5\,\mathrm{W\,m^{-2}}$). The relative offset is highest for continental aerosols and

lowest for urban aerosols, but the much higher values of AOD observed in areas influenced by wildfires or urban areas contribute to a more significant correction in these cases, and may represent a relevant bias in DLW values for cities such as Beijing and Kanpur. The influence of relative humidity on the correction factor is found to be negligible even at very high aerosol loads.

The input-scaling approach (δ-M approximation) is generally accurate for relatively low aerosol loading values observed in non-urban areas, while the proposed net-result-based scaling is valid for all values of aerosol loading, including high aerosol urban areas, and rural and urban areas affected by large-scale fire pollution.

Then, with the atmospheric model described above, a Spectral Cloud Optical Property Estimation (SCOPE) method for real-time, direct estimation of cloud optical properties from high-resolution longwave remote sensing data is presented. By considering only the longwave spectrum, the method provides a unified approach to estimating cloud properties during day or night and does not need to consider the view angle of the instruments. For the basic SCOPE method, remote sensing data from GOES-R images are used in parallel with minimal ground measured variables as inputs. A two-stream LBL atmospheric radiative model is used to get the estimated value for upwelling flux for each channel, which is compared with the measured channel-averaged Outgoing Longwave Radiation (OLR). The optimal cloud height z_T, cloud optical depth COD, and cloud thickness Δz are obtained when the comparison error is minimum. As SCOPE has minimal data dependencies, a linear correction to standard atmospheric profiles (temperature, gas, and aerosol profiles), allows SCOPE to be applied to a wide range of surface conditions and locations. SCOPE 2.0, as a improved version of SCOPE method, considering the situation of high ice clouds and multi-layer clouds, is also presented and compared.

The performances of SCOPE 1.0 and 2.0 are evaluated using a full year of data (1/1/2018 - 12/31/2018) for seven meteorologically diverse locations across the United States, covering both clear and cloudy cases. For each case, SCOPE estimates cloud optical properties from the upwelling longwave radiative flux at the top of the atmosphere. As a validation, the estimated properties are used to to model the downwelling longwave radiative flux at the surface and compared against ground measurements. In SCOPE 2.0, downwelling longwave radiation is also used to estimate lower cloud information and shortwave radiation modeled from Monte Carlo simulation is compared against the ground measured GHI as a validation. SCOPE 1.0 achieves downwelling longwave RMSE within 20 W m^{-2} for clear conditions and within 40 W m^{-2} for

all sky condition (clear + cloudy). SCOPE 2.0, with the additional DWL inputs, achieves slightly better RMSE (about 2 - 10 W m^{-2}) for shortwave validation. The results indicate that SCOPE is suitable for solar forecasting applications by providing real-time accurate cloud estimates.

Finally, a convolutional neural network model using ground measurements as well as the 3D cloud map derived from satellite data by SCOPE method as inputs is developed to model solar radiation. Two proposed models, one with and one without SCOPE cloud estimation are compared and give average RMSE values 44.7 W/m^2 and 68.9 W/m^2 respectively. Both models perform well and the errors are within competitive range of standard reference models (the reference NSRDB model has an average RMSE of 64.8 W/m^2). This indicates that convolutional neural networks hold promise for interpreting the information contained in the satellite images and relating it to ground irradiance. The CNN + SCOPE model gives much better results than the CNN model that only uses 10 longwave channels and the reference, which indicates that the physical features captured by the SCOPE model contribute to the improvement of the overall model performance. The CNN+16 channel model, gives similar results as the CNN+SCOPE model, which in turn is also superior to the CNN+10 channel model. Therefore, this study provides strong support for also including information from the shortwave channels in order to further improve solar radiation prediction based on spectral analysis of remote sensing images. In a future work, we will add a model for the 6 shortwave channels to the latest version of the SCOPE+CNN model in order to further increase the accuracy of the overall results, in preparation for the development of a comprehensive intra-day forecasting methodology based on CNN analysis of remote sensing and physical modeling of both shortwave and longwave radiative fluxes.

Bibliography

[1] D. Lubin, S. Satheesh, G. McFarquar, A. J. Heymsfield, Longwave radiative forcing of Indian Ocean tropospheric aerosol, Journal of Geophysical Research: Atmospheres 107 (D19) (2002).

[2] G. M. Hale, M. R. Querry, Optical constants of water in the 200-nm to 200-μm wavelength region, Applied optics 12 (3) (1973) 555–563.

[3] U.S. Department of Energy, ICRCCM infrared (clear-sky) line-by line radiative fluxes (DB-1002), http://cdiac.ornl.gov/ndps/db1002.html (2017).

[4] M. Li, Z. Liao, C. F. M. Coimbra, Spectral model for clear sky atmospheric longwave radiation, Journal of Quantitative Spectroscopy and Radiative Transfer 209 (2018) 196–211.

[5] E. F. Vermote, D. Tanre, J. L. Deuze, M. Herman, J. J. Morcrette, Second simulation of the satellite signal in the solar spectrum, 6S: an overview, IEEE Transactions on Geoscience and Remote Sensing 35 (1997) 675–686.

[6] D. Lubin, S. K. Satheesh, G. McFarquar, A. J. Heymsfield, Longwave radiative forcing of Indian ocean tropospheric aerosol, Journal of Geophysical Research - Atmospheres 107 (D19) (2002) INX2 3–1–INX2 3–13.

[7] H. Bahar, P. Bojek, Solar pv, Tech. rep., International energy agency technical report (2020).

[8] IEA-PVPS, Trends in photovoltaic applications, Tech. rep., International energy agency technical report (2016).

[9] R. Marquez, C. F. Coimbra, Solar Energy, Oxford University Press, Oxford, UK, 2013.

[10] W. Sun, N. G. Loeb, P. Yang, On the retrieval of ice cloud particle shapes from POLDER measurements, Journal of Quantitative Spectroscopy and Radiative Transfer 101 (2006) 435–447.

[11] D. P. Larson, M. Li, C. F. M. Coimbra, SCOPE: Spectral cloud optical property estimation using real-time GOES-R longwave imagery, Journal of Renewable Sustainable Energy 12 (2020) 1811–1818.

[12] R. Marquez, V. Gueorguiev, C. F. M. Coimbra, Forecasting of global horizontal irradiance using sky cover indices, ASME Journal of Solar Energy Engineering 135 (2012) 0110171–0110175.

[13] Y. Chu, L. Nonnenmacher, R. H. Inman, Z. Liao, H. T. C. Pedro, C. F. M. Coimbra, A smart image-based cloud detection system for intra-hour solar irradiance forecasts, Journal of Atmospheric and Oceanic Technology 31 (9) (2014) 1995–2007.

[14] Y. Sun, G. Szucs, A. R. Brandt, Solar pv output prediction from video streams using convolutional neural networks, Energy and Environmental Science 11 (2018) 026501.

[15] A. Ryu, M. Ito, H. Ishii, Y. Hayashi, Preliminary analysis of short-term solar irradiance forecasting by using total-sky imager and convolutional neural network, in: 2019 IEEE PES GTD Grand International Conference and Exposition Asia (GTD Asia), 2019, pp. 627–631. doi:10.1109/GTDAsia.2019.8715984.

[16] A. F. Mills, C. F. M. Coimbra, Basic heat and mass transfer, 3rd Edition, Temporal Publishing, San Diego, CA, 2015.

[17] National Renewable Energy Laboratory, 2000 ASTM standard extraterrestrial spectrum reference E-490-00, https://www.nrel.gov/grid/solar-resource/spectra-astm-e490.html.

[18] S. Chandrasekhar, Radiative Transfer, Oxford University Press, Oxford, UK, 1950.

[19] H. H. Tynes, Monte Carlo solutions of the radiative transfer equation for scattering systems, Ph.D. thesis, Texas A&M University (2001).

[20] B. Mayer, Radiative transfer in the cloudy atmoshphere, European Physics Journal Conferences 1 (2009) 75–99.

[21] J. T. Farmer, Comparison of monte carlo strategies for radiative transfer in participating media, Advances In Heat Transfer 31 (1998) 333–429.

[22] J. R. Howell, The monte carlo method in radiative heat transfer, Journal of Heat Transfer 120 (1998) 547–560.

[23] M. F. Modest, Radiative Heat Transfer, Academic press, 2013.

[24] G. Demirkaya, Monte carlo solution of a radiative heat transfer problem in a 3d rectangular enclosure containing absorbing, emitting, and anisotropically scattering medium, master thesis, The Middle East Technical University (December 2003).

[25] B. A. Whitney, Monte carlo radiative transfer, Fluid Flows to Black Holes: A Tribute to S Chandrasekhar on his Birth Centenary. Edited by Saikia DJ et al. Plubished by World Scientific Publishing Co. Pte. Ltd (2011) 151–176.

[26] E. D. Cashwell, C. J. Everett, A Manual of the Monte Carlo Method for Random Walk Problems, Pergamon press, 1959.

[27] L. L. House, L. W. Avery, The monte carlo technique applied to radiative transfer, Journal of Quantitative Spectroscopy and Radiative Transfer 9 (1969) 1579–1591.

[28] D. G. Collins, W. G. Blattner, M. B. Wells, H. G. Horak, Backward monte carlo calculations of the polarization characteristics of the radiation emerging from spherical-shell atmospheres., Applied Optics 11 (11) (1972) 2684–2696.

[29] C. N. Adams, G. W. Kattawar, Radiative transfer in spherical shell atmospheres - i. rayleigh scattering, ICARUS: International Journal of Solar System Studies 35 (1978) 139–151.

[30] D. V. Walters, R. O. Buckius, Rigorous development for radiation heat transfer in non-homogeneous absorbing, emitting and scattering media, International Journal of Heat and Mass Transfer 35 (12) (1992) 3323–3333.

[31] D. V. Walters, R. O. Buckius, Monte carlo methods for radiative transfer in scattering media, Annual Review of Heat Transfer 5 (1994) 131–176.

[32] K. M. Case, Transfer problems and the reciprocity principle, Review Modern Physics 29 (4) (1957) 651–663.

[33] A. Ambirajan, D. C. Look, A backward monte carlo estimator for the multiple scattering of a narrow light beam, Journal of Quantitative Spectroscopy and Radiative Transfer 56 (3) (1996) 317–336.

[34] M. F. Modest, Backward monte carlo simulations in radiative heat transfer, Journal of Heat Transfer 125 (2003) 57–62.

[35] M. Li, Y. Jiang, C. F. M. Coimbra, On the determination of atmospheric longwave irradiance under all-sky conditions, Solar Energy 144 (2017) 40–48.

[36] W. L. Ridgway, A. Arking, Computation of atmospheric cooling rates by exact and approximate methods, Journal of Geophysical Research: Atmospheres 96 (D5) (1991) 8969–8984.

[37] S. A. Clough, M. W. Shephard, E. J. Mlawer, J. S. Delamere, M. J. Iacono, K. Cady-Pereira, S. Boukabara, P. D. Brown, Atmospheric radiative transfer modeling: a summary of the AER codes, Journal of Quantitative Spectroscopy and Radiative Transfer 91 (2) (2005) 233–244.

[38] S. A. Buehler, P. Eriksson, T. Kuhn, A. Von Engeln, C. Verdes, ARTS- the atmospheric radiative transfer simulator, Journal of Quantitative Spectroscopy and Radiative Transfer 91 (1) (2005) 65–93.

[39] A. Berk, F. Hawes, Validation of MODTRAN® 6 and its line-by-line algorithm, Journal of Quantitative Spectroscopy and Radiative Transfer 203 (2017) 542 – 556.

[40] I. E. Gordon, L. S. Rothman, C. Hill, R. V. Kochanov, Y. Tan, P. F. Bernath, M. Birk, V. Boudon, A. Campargue, K. Chance, B. Drouin, The HITRAN2016 molecular spectroscopic database, Journal of Quantitative Spectroscopy and Radiative Transfer 203 (2017) 3–69.

[41] E. J. Mlawer, V. H. Payne, J.-L. Moncet, J. S. Delamere, M. J. Alvarado, D. C. Tobin, Development and recent evaluation of the MT_CKD model of continuum absorption, Philosophical Transactions of the Royal Society of London A: Mathematical, Physical and Engineering Sciences 370 (2012) 2520–2556.

[42] A. Eddington, On the radiative equilibrium of the stars, Monthly Notices of the Royal Astronomical Society 77 (1916) 16–35.

[43] C. Sagan, J. B. Pollack, Anisotropic nonconservative scattering and the clouds of Venus, Journal of Geophysical Research 72 (2) (1967) 469–477.

[44] M. Q. Brewster, C. L. Tien, Examination of the two-flux model for radiative transfer in particular systems, International Journal of Heat and Mass Transfer 25 (12) (1982) 1905–1907.

[45] O. B. Toon, C. McKay, T. Ackerman, K. Santhanam, Rapid calculation of radiative heating rates and photodissociation rates in inhomogeneous multiple scattering atmospheres, Journal of Geophysical Research: Atmospheres 94 (D13) (1989) 16287–16301.

[46] D. K. Edwards, The plating algorithm for radiation script-F transfer factor, Journal of heat transfer 108 (1) (1986) 237–238.

[47] S. Manabe, F. Möller, On the radiative equilibrium and heat balance of the atmosphere, Monthly Weather Review, 1961.

[48] S. Manabe, R. F. Strickler, Thermal equilibrium of the atmosphere with a convective adjustment, Journal of the Atmospheric Sciences 21 (4) (1964) 361–385.

[49] G. P. Anderson, S. A. Clough, F. X. Kneizys, J. H. Chetwynd, E. P. Shettle, AFGL atmospheric constituent profiles (0.120 km), Tech. rep., DTIC Document (1986).

[50] O. A. Alduchov, R. E. Eskridge, Improved Magnus form approximation of saturation vapor pressure, Journal of Applied Meteorology 35 (4) (1996) 601–609.

[51] Carbon Dioxide Information Analysis Center, Recent greenhouse gas concentrations, http://cdiac.ornl.gov/pns/current-ghg.html (2016).

[52] H. Yu, M. Chin, D. M. Winker, A. H. Omar, Z. Liu, C. Kittaka, T. Diehl, Global view of aerosol vertical distributions from CALIPSO lidar measurements and GOCART simulations: Regional and seasonal variations, Journal of Geophysical Research: Atmospheres 115 (D4) (2010).

[53] G. W. Petty, A first course in atmospheric radiation, Sundog Pubulishing, Madison, WI, United States, 2006.

[54] G. Lesins, P. Chylek, U. Lohmann, A study of internal and external mixing scenarios and its effect on aerosol optical properties and direct radiative forcing, Journal of Geophysical Research: Atmospheres 107 (D10) (2002).

[55] H. Yu, Y. J. Kaufman, M. Chin, G. Feingold, L. Remer, T. Anderson, Y. Balkanski, N. Bellouin, O. Boucher, S. Christopher, P. DeCola, R. Kahn, D. Koch, N. Loeb, M. S. Reddy, M. Schulz, Takemura, M. Zhou, A review of measurement-based assessments of the aerosol direct radiative effect and forcing, Atmospheric Chemistry and Physics 6 (3) (2006) 613–666.

[56] C. F. Bohren, D. R. Huffman, Absorption and scattering of light by small particles, John Wiley & Sons, 2008.

[57] C. Mätzler, MATLAB functions for Mie scattering and absorption, version 2, IAP Research Report 8 (2002) 1–24.

[58] National Oceanic and Atmospheric Administration, SURFRAD Network, http://www.esrl.noaa.gov/gmd/grad/surfrad/ (2015).

[59] J. Zhang, S. A. Christopher, Longwave radiative forcing of Saharan dust aerosols estimated from MODIS, MISR, and CERES observations on terra, Geophysical Research Letters 30 (23) (2003).

[60] M. Li, Z. Liao, C. F. M. Coimbra, Spectral model for clear sky atmospheric longwave radiation, Journal of Quantitative Spectroscopy and Radiative Transfer 209 (2018) 196–211.

[61] J. E. Hansen, L. D. Travis, Light scattering in planetary atmospheres, Space science reviews 16 (4) (1974) 527–610.

[62] N. L. Miles, J. Verlinde, E. E. Clothiaux, Cloud droplet size distributions in low-level stratiform clouds, Journal of the atmospheric sciences 57 (2) (2000) 295–311.

[63] H. Barker, G. Stephens, P. Partain, J. Bergman, B. Bonnel, K. Campana, E. Clothiaux, S. Clough, S. Cusack, J. Delamere, Assessing 1D atmospheric solar radiative transfer models: Interpretation and handling of unresolved clouds, Journal of Climate 16 (16) (2003) 2676–2699.

[64] R. M. Goody, Y. L. Yung, Atmospheric radiation: theoretical basis, 2nd edition (1989).

[65] R. V. Kochanov, I. E. Gordon, L. S. Rothman, P. Wcisło, C. Hill, J. S. Wilzewski, HITRAN application programming interface (HAPI): A comprehensive approach to working with spectroscopic data, Journal of Quantitative Spectroscopy and Radiative Transfer 177 (2016) 15–30.

[66] S. A. Buehler, A. Von Engeln, E. Brocard, V. O. John, T. Kuhn, P. Eriksson, Recent developments in the line-by-line modeling of outgoing longwave radiation, Journal of Quantitative Spectroscopy and Radiative Transfer 98 (3) (2006) 446–457.

[67] D. Edwards'GENLN, A general line-by-line atmospheric transmittance and radiance model. version 3.0 description and users guide,', National Center for Atmospheric Research (1992).

[68] M. Lee, Scaling anisotropic scattering in radiation heat transfer for a planar medium, Urbana 2 (1982) 61801.

[69] R. G. Ellingson, J. Ellis, S. Fels, The intercomparison of radiation codes used in climate models: Longwave results, Journal of Geophysical Research: Atmospheres 96 (D5) (1991) 8929–8953.

[70] National Aeronautics and Space Administration - NASA, CIRC: Continual Intercomparison of Radiation Codes, https://circ.gsfc.nasa.gov/index.html (2015).

[71] L. Oreopoulos, E. Mlawer, J. Delamere, T. Shippert, J. Cole, B. Fomin, M. Iacono, Z. Jin, J. Li, J. Manners, The continual intercomparison of radiation codes: Results from phase i, Journal of Geophysical Research: Atmospheres 117 (D6) (2012).

[72] P. Berdahl, M. Martin, F. Sakkal, Thermal performance of radiative cooling panels, International Journal of Heat and Mass Transfer 26 (1983) 871–880.

[73] A. Yoshida, T. Kunitomo, One-dimensional simulation of the thermal structure of urban atmospheres, International Journal of Heat and Mass Transfer 29 (1986) 1041–1049.

[74] M. Li, Y. Jiang, C. F. M. Coimbra, On the determination of atmospheric longwave irradiance under all-sky conditions, Solar Energy 144 (2017) 40–48.

[75] M. Li, C. F. M. Coimbra, On the effective spectral emissivity of clear skies and the radiative cooling potential of selectively designed materials, International Journal of Heat and Mass Transfer 135 (2019) 1053–1062.

[76] H. Yang, B. Kurtz, D. Nguyen, B. Urquhart, C. Chow, M. Ghonima, J. Kleissl, Solar irradiance forecasting using a ground-based sky imager developed at UC San Diego, Solar Energy 103 (2014) 502–524.

[77] E. Shahraeeni, D. Or, Quantification of subsurface thermal regimes beneath evaporating porous surfaces, International Journal of Heat and Mass Transfer 54 (2011) 4193–4202.

[78] H. Lee, R. O. Buckius, Scaling anisotropic scattering in radiation heat transfer for a planar medium, Journal of Heat Transfer 104 (1982) 68–75.

[79] B. H. J. McKellar, M. A. Box, The scaling group of the radiatve transfer equation, Jounral of the Atmospheric Sciences 38 (26) (1981) 1063–1068.

[80] J. H. Joseph, W. J. Wiscombe, J. A. Weinmann, The delta-Eddington approximation for radiative flux transfer, Journal of Atmospheric Science 33 (1976) 2452–2459.

[81] J. F. Potter, The delta function approximation in radiative transfer theory, Journal of Atmospheric Science 27 (1970) 943–949.

[82] W. J. Wiscombe, The delta-M method: rapid yet accurate radiative flux calculations for strongly asymmetric phase functions, Journal of Atmospheric Science 34 (1977) 1408–1422.

[83] Z. Guo, S. Maruyama, Radiative heat transfer in inhomogeneous, nongray, anisotropically scattering media, International Journal of Heat and Mass Transfer 120 (2000) 2325–2336.

[84] L. A. Dombrovsky, W. Linpinski, A combined p_1 and Monte Carlo model for multidimensional radiative transfer problems in scattering media, Computational Thermal Sciences 2 (26) (2010) 549–560.

[85] J. Heino, S. Arridge, J. Sikora, E. Somersalo, Anisotropic effects in highly scattering media, Physical Review E 68 (2003) 031908.

[86] S. Manabe, R. F. Strickler, Thermal equilibrium of the atmosphere with a convective adjustment, Journal of the Atmospheric Sciences 21 (4) (1964) 361–385.

[87] G. P. Anderson, S. A. Clough, F. X. Kneizys, J. H. Chetwynd, E. P. Shettle, AFGL atmospheric constituent profiles (0 to 120 km), Tech. rep., Air Force Geophysics Laboratory (1986).

[88] I. E. Gordon, L. S. Rothman, C. Hill, R. V. Kochanov, Y. Tan, P. F. Bernath, M. Birk, V. Boudon, A. Campargue, K. Chance, The HITRAN2016 molecular spectrospopic data base, Journal of Quantitative Spectroscopy and Radiative Transfer 203 (2017) 3–69.

[89] M. Cherkaoui, J.-L. Dufresne, R. Fournier, J.-Y. Grandpeix, A. Lahellec, Monte Carlo simulation of radiation in gases with a narrow-band model and a net-exchange formulation, ASME Journal of Heat Transfer (1996) 401–407.

[90] H. Yu, M. Chin, D. M. Winker, A. H. Omar, Z. Liu, C. Kittaka, T. Diehl, Global view of aerosol vertical distributions from CALIPSO lidar measurements and GOCART simulations: Regional and seasonal variations, Journal of Geophysical Research: Atmospheres 115 (D04) (2010).

[91] Q. Xu, H. Wei, R. Rao, H. Hu, Simultaneous determination of aerosol optical thickness and exponent of Junge power law from satellite measurements of two near-infrared bands over the ocean, Optics Express 15 (8) (2007) 5227 – 5236.

[92] C. Pilinis, S. N. Pandis, J. H. Seinfeld, Sensitivity of direct climate forcing by atmospheric aerosols to aerosol size and composition, Journal of Geophysical Research 100 (D9) (1995) 18739–18754.

[93] E. M. Patterson, D. A. Gillette, Commonalities in measured size distributions for aerosol having a soil-derived component, Journal of Geophysical Research 82 (15) (1977) 2074–2082.

[94] Y. J. Kim, H. Sievering, J. F. Boatman, Airborne measurement of atmospheric aerosol particles in the lower troposphere over the central United States, Journal of Geophysical Research 93 (D10) (1988) 12631–12644.

[95] J. Blanchet, R. List, Estimation of optical properties of arctic haze using a numerical model, Atmosphere-Ocean 21 (4) (1983) 444–465.

[96] D. Forgan, An introduction to Monte Carlo radiative transfer, Tech. rep., Institute for Astronomy Royal Observatory Edinburgh (2009).

[97] D. Toublanc, Henyey-Greenstein and Mie phase functions in Monte Carlo radiative transfer computations, Applied Optics 35 (18) (1996) 3270–3274.

[98] O. N. Vassiliev, Monte Carlo Methods for Radiation Transport: Fundamentals and Advanced Topics, Springer, 2017.

[99] A. Maurente, F. H. R. França, A multi-spectral energy bundle method for efficient Monte Carlo radiation heat transfer computations in participating media, International Journal of Heat and Mass Transfer 90 (2015) 351–357.

[100] S. A. Dupree, S. K. Fraley, Monte Carlo Primer: A Practical Approach to Radiation Transport, Kluwer Academic/Plenum Publishers, 2002.

[101] A. Haghighat, Monte Carlo methods for particle transport, Crc Press, 2015.

[102] U.S. Department of Energy, ICRCCM infrared (clear-sky) line-by-line radiative fluxes (DB-1002), http://cdiac.ornl.gov/ndps/db1002.html (2017).

[103] Q. Fu, P. Yang, W. B. Sun, An accurate parameterization of the infrared radiative properties of cirrus clouds for climate models, Journal of Climate 11 (9) (1998) 2223–2237.

[104] Q. Fu, An accurate parameterization of the solar radiative prop-erties of cirrus clouds for climate models, Journal of Climate 9 (1996) 2058–2082.

[105] P. Yang, H. Wei, H.-L. Huang, B. A. Baum, Y. X. Hu, G. W. Kattawar, M. I. Mishchenko, Q. Fu, Scattering and absorption property database for nonspherical ice particles in the near- through far-infrared spectral region, Applied Optics 44 (26) (2005) 5512 – 5523.

[106] J. Joiner, A. P. Vasilkov, P. K. Bhartia, G. Wind2, S. Platnick, W. P. Menzel, Detection of multi-layer and vertically-extended clouds using a-train sensors, Atmospheric Measurement Techniques 3 (2010) 233–247.

[107] S. Li, Q. Min, Diagnosis of multilayer clouds using photon pathlength distributions, Atmospheric Chemistry and Physics 19 (2019) 5111–5126.

[108] R. H. Inman, J. G. Edson, C. F. M. Coimbra, Impact of local turbidity estimation on clear sky models for direct normal irradiance, Solar Energy 117 (2015) 125–138.

[109] A. Krizhevsky, I. Sutskever, G. E. Hinton, Imagenet classification with deep convolutional neural networks, Advances in Neural Information Processing Systems (2012) 1095–1105.

[110] K. Simonyan, A. Zisserman, Very deep convolutional networks for large-scale image recognition, arXiv:1409.1556 (2014).

[111] C. Szegedy, W. Liu, Y. Jia, P. Sermanet, S. Reed, D. Anguelov, D. Erhan, V. Vanhoucke, A. Rabinovich, Going deeper with convolutions, Proceedings of the IEEE conference on computer vision and pattern recognition (2015) 1095–1105.

[112] K. He, X. Zhang, S. Ren, J. Sun, Deep residual learning for image recognition, Proceedings of the IEEE conference on computer vision and pattern recognition (2016) 770–778.

[113] Y. Chu, M. Li, H. T. Pedro, C. F. Coimbra, Real-time prediction intervals for intra-hour dni forecasts, Renewable Energy 83 (2015) 234–244.

[114] V. Nair, G. E. Hinton, Rectified linear units improve restricted boltzmann machines, Proceedings of the 27th international conference on machine learning (ICML-10) (2010) 807–814.

[115] S. Ioffe, C. Szegedy, Batch normalization: Accelerating deep network training by reducing internal covariate shift, International Conference on Machine Learning (2015) 448–456.

[116] F. J. Huang, Y.-L. Boureau, Y. LeCun, Unsupervised learning of invariant feature hierarchies with applications to object recognition, Computer Vision and Pattern Recognition (2007) 1–8.

[117] D. Kingma, J. Ba, Adam: A method for stochastic optimization, arXiv preprint arXiv:1412.6980 (2014).